ENABLING MOBILE NEUTRON DETECTION SYSTEMS WITH CLYC

DISSERTATION

Matthew C. Recker, Maj, USAF

AFIT-ENP-DS-19-S-028

DEPARTMENT OF THE AIR FORCE
AIR UNIVERSITY

AIR FORCE INSTITUTE OF TECHNOLOGY

Wright-Patterson Air Force Base, Ohio

AFIT-ENP-DS-19-S-028

ENABLING MOBILE NEUTRON DETECTION SYSTEMS WITH CLYC

DISSERTATION

Presented to the Faculty

Graduate School of Engineering and Management

Air Force Institute of Technology

Air University

Air Education and Training Command

in Partial Fulfillment of the Requirements for the

Degree of Doctor of Philosophy in Nuclear Engineering

Matthew C. Recker, B.S., M.S.

Maj, USAF

12 September 2019

AFIT-ENP-DS-19-S-028

ENABLING MOBILE NEUTRON DETECTION SYSTEMS WITH CLYC

DISSERTATION

Matthew C. Recker, B.S., M.S.
Maj, USAF

Committee Membership:

John W. McClory
Chairman

Edward J. Cazalas
Member

Maj James E. Bevins, PhD
Member

Benjamin F. Akers
Member

ADEDEJI B. BADIRU, PhD
Dean, Graduate School of Engineering and Management

AFIT-ENP-DS-19-S-028

Abstract

$Cs_2LiYCl_6:Ce^{3+}$ (CLYC) has the desirable property of being sensitive to both gamma rays and neutrons while producing waveforms suitable for pulse shape discrimination (PSD) to determine which radiation was detected. This dissertation examines the behavior of CLYC to support its further development for mobile and portable applications. First, the feasibility of performing PSD with CLYC and an inexpensive data acquisition system was examined. A PSD technique compared a delayed region of the detection waveform to the total waveform to clearly distinguish both events with a figure of merit of 1.42. Next, the performance of a SiPM was compared to a traditional PMT. Analysis showed that using a SiPM degraded the energy resolution by an average of 34.0±0.7% (at 662 keV). Measurements were also taken using a CLYC crystal with two optical windows to determine the direction of a neutron source. Based on a Monte Carlo model that established thermal neutrons have a maximum penetration depth of 1.0-1.5 cm in CLYC, a rotating detector was able to determine the direction of a neutron source with an accuracy of ±10°. An analysis of the ability of clustering algorithms to discriminate between gamma ray and neutron interactions was also performed. A methodology was developed and applied to separate these two interactions and provide the ability to isolate the $^{35}Cl(n,p)^{35}S$ interaction with thermal neutrons, which occurs close to the gamma ray region and is difficult to separate visually. Finally, the effect of temperature on a ^{7}Li (99%) enriched CLYC crystal (important when the $^{35}Cl(n,p)^{35}S$ interaction is more desirable than $^{6}Li(n,t)\alpha$ interaction) was examined. Measurements agreed with previous results from ^{6}Li (95%) enriched CLYC, but also indicated that identifying the cluster corresponding to thermal neutrons interacting with ^{35}Cl was temperature dependent.

This dissertation is dedicated to my family. Thank you for you love, support and understanding throughout this research endeavor!

Acknowledgements

I would like to thank Dr. John McClory for serving as my research advisor and chair of my dissertation committee as well as providing support through valuable insight and guidance. I would like to thank Dr. Edward Cazalas for not only serving on my research committee but also providing many hours of assistance in the lab developing experiments and taking data as well as interpreting results. Finally, I'd like to thank Maj James Bevins and Dr. Benjamin Akers for their insight and guidance as members of my research committee.

Matthew C. Recker

Table of Contents

Page

Abstract iv

Acknowledgements vi

List of Figures x

List of Tables xviii

I. Introduction 1

1.1 Applications of Neutron Detection with CLYC 2
1.2 Research Objectives 5

II. Background 8

2.1 Neutron detectors 8
2.2 CLYC 10
Structure and growth 10
Neutron interactions 10
Lithium 12
Chlorine 15
Cesium 18
Yttrium 19
Scintillation process and mechanisms in CLYC 21
Direct electron-hole capture 22
Trapped hole (V_k) centers 23
Self-trapped excitons 24
Core-to-valence luminescence 25
Quenching in CLYC 25
2.3 Detector system 28
SiPM Arrays 29
2.4 Pulse-shape discrimination 30
Waveform analysis methods 30
Figure of merit 32

III. Pulse shape discrimination with a low-cost digitizer using commercial off-the-shelf components 33

3.1 Abstract 33
3.2 Introduction 34
3.3 Experiment 36
Detector setup 36
Digitizer setup 36

Page

Neutron Measurements . . . 39
3.4 Results . . . 40
Energy spectra . . . 40
Pulse shape discrimination . . . 42
3.5 Conclusion . . . 45

IV. Comparison of SiPM and PMT Performance Using a $Cs_2LiYCl_6:Ce^{3+}$ (CLYC) Scintillator with Two Optical Windows . . . 46

4.1 Abstract . . . 46
4.2 Introduction . . . 47
4.3 Experiment . . . 49
4.4 Results and Discussion . . . 52
Single-sided crystals . . . 52
Double-sided crystal . . . 57
4.5 Conclusion . . . 63

V. Determining Direction of a Neutron Source Using a $Cs_2LiYCl_6:Ce^{3+}$ (CLYC) Scintillator with Two Optical Windows . . . 64

5.1 Introduction . . . 64
5.2 2D Monte Carlo Model . . . 65
5.3 Experiment . . . 67
5.4 Results . . . 68
5.5 Conclusion . . . 73

VI. Comparison of Clustering Algorithms for Analysis of Pulse Shape Data from $Cs_2LiYCl_6:Ce^{3+}$ (CLYC) . . . 75

6.1 Abstract . . . 75
6.2 Introduction . . . 76
6.3 Experiment . . . 77
6.4 Clustering Algorithm Analysis . . . 79
K-Means . . . 79
DBSCAN . . . 79
Gaussian Mixture Model . . . 81
Recommended Cluster Analysis Methodology . . . 82
6.5 Cluster Analysis Applied . . . 83
Expanded Data Set . . . 83
CLYC-7 with a Thermal Neutron Source . . . 87
CLYC-7 with Continuous Energy Neutron Sources . . . 87
6.6 Conclusion . . . 90

Page

VII. Controlling CLYC Crystal Temperature and Analysis of CLYC-7 Performance from -20°C to 40°C 93

7.1 Introduction 93
7.2 Experimental Method 94
7.3 Temperature Controller 94
7.4 Results and Analysis 97
7.5 Conclusion 103

VIII. Conclusion 105

Bibliography 110

List of Figures

Figure		Page
1	Neutron interaction cross sections for ^{6}Li across the full neutron energy range with logarithmically scaled energy (a) to show low energy features and linearly scaled energy (b) to show more detail in the fast (>1 MeV) region.	13
2	Neutron interaction cross sections for ^{7}Li across the full neutron energy range with logarithmically scaled energy (a) to show low energy features and linearly scaled energy (b) to show more detail in the fast (>1 MeV) region.	14
3	Neutron interaction cross sections for ^{35}Cl across the full neutron energy range with logarithmically scaled energy (a) to show low energy features and linearly scaled energy (b) to show more detail in the fast (>1 MeV) region.	16
4	Neutron interaction cross sections for ^{37}Cl across the full neutron energy range with logarithmically scaled energy (a) to show low energy features and linearly scaled energy (b) to show more detail in the fast (>1 MeV) region.	17
5	Neutron interaction cross sections for ^{133}Cs across the full neutron energy range with logarithmically scaled energy (a) to show low energy features and linearly scaled energy (b) to show more detail in the fast (>1 MeV) region.	19
6	Neutron interaction cross sections for ^{89}Y across the full neutron energy range with logarithmically scaled energy (a) to show low energy features and linearly scaled energy (b) to show more detail in the fast (>1 MeV) region.	21

7 The process of creating a V_k center (left panel) or self-trapped exciton (STE) and eventual excitation of the Ce^{3+} ion (right panel). Incident radiation (or secondary charged particles in the case of incident neutrons) promotes an electron from the valence band to the conduction band. Any excess energy is lost as the electron-hole pair relaxes so that the hole is at the top of the valence band and the electron is at the bottom of the conduction band. The hole becomes captured between two Cl^- anions to form a V_k center (Cl_2^- in CLYC) . This defect is able to travel around the lattice until it forms a complex with a Ce^{3+} ion in (a) and captures a free electron in the conduction band and emits a photon as it decays from the excited 5d $\rightarrow$ 4f state. If it captures an electron from the conduction band before it forms a complex with Ce^{3+} it will form an STE, as shown in (b). This neutral defect can also travel around the crystal and eventually cause excitation within a Ce^{3+} ion, leading to luminescence, or it can luminesce on its own. It is possible for this STE luminescence to excite the Ce^{3+} if there is an overlap in energies. Diagrams are based on those by Pieter Dorenbos in his paper on scintillation mechanisms in Ce^{3+} doped halide scintillator. 24

8 Basic CLYC detector setup. Crystal is either placed directly on a SiPM array or a PMT. For the SiPM configuration the SiPM array is attached to an interface board which is connected to a control board that provides power to the components and provides signal output to a DAQ. For the PMT setup, the signal is read directly from the PMT by the DAQ without any shaping or modification. 29

9 Demonstration of pulse-shape discrimination windows using average waveforms for gamma and neutron pulses in CLYC. 31

10 The FemtoDAQ two channel digitizer showing (a) front and (b) back connections and switches. 37

11 Flowchart diagram of Python code written for collecting pulse shape data with FemtoDAQ. 38

Figure Page

12 Flowchart diagram of Python code that controls the FemtoDAQ remotely. The third box indicates the code described in Fig. 11. 39

13 Experimental layout for irradiation from thermal neutrons generated by a PuBe source within a graphite pile. 41

14 Calibrated gamma ray energy spectrum for ^{137}Cs as measured by CLYC using FemtoDAQ (R = 8.7% at 662 keV) and an MCA with GammaVision (R = 8.8% at 662 keV). 41

15 Energy spectra for three sources (^{137}Cs, ^{60}Co and thermal neutrons) as measured by CLYC. Peak at ∼3.1 MeVee is due to thermal neutron interaction ^{6}Li (n,t) ^{4}He (Q-value = 4.78 MeV). 43

16 Individual and averaged waveforms for gamma and neutron events in CLYC. Also shown are the windows for prompt and delayed measurements used to calculate PSD ratios. 43

17 Two dimensional hexbin histogram of PSD ratios plotted against energy measured with a histogram of PSD ratios used to calculate a figure of merit for separating neutron and gamma pulses. 44

18 3D printed crystal housings for (a) coupling standard CLYC crystals to the PMT and (b) coupling the double-sided CLYC crystal to a PMT and SiPM concurrently. The PMT attaches to the top circular portion of the housing for the double-sided crystal (b) and the SiPM is completely contained in the black rectangular portion. The crystal sits slightly above the plastic surface to allow good coupling with the PMT. The SiPM rests on compressible foam which holds the components together, but also provides enough vertical movement to ensure the components are not damaged when the PMT is bolted tightly to the housing. 51

Figure Page

19 Energy spectra for three CLYC crystals exposed to ^{137}Cs, ^{60}Co, and thermal neutrons. Each crystal was used for two measurements, one with a PMT and one with a SiPM. In all cases, the PMT had better resolution than the SiPM, but both photomultipliers were able to fully resolve all peaks. The crystal identified as CS-2 was made using 99% enriched ^{7}Li, the other two were made with 95% enriched ^{6}Li. 53

20 Two-dimensional histograms of PSD ratio and energy with intensity scaled logarithmically for (a) PMT and (b) SiPM measurements with the RMD-2 crystal. PMT shows better resolution, but SiPM is also able to clearly resolve the photopeaks of known gamma ray sources and the strong thermal neutron peak. A small cluster is visible in the PMT plot due to the ^{35}Cl(n,p)^{35}S interaction that is not defined in the SiPM measurement. All known sources are labeled in the plots and the FOM is reported for all interactions with energy greater than 500 keVee. 55

21 Averaged waveforms, normalized to their peak amplitudes, for ^{137}Cs gamma ray interactions (a and c) and thermal neutron interaction with ^{6}Li (b and d) in each crystal measured using the PMT (a and b) and the SiPM (c and d). When measured using the SiPM, the waveforms were longer-lived and the gamma ray events had a secondary peak. The fast component in these waveforms corresponds to photons generated by the CVL process while the secondary peak corresponds to the slower scintillation processes. 58

Figure Page

22 Two-dimensional histograms of PSD ratio and uncalibrated energy with intensity scaled logarithmically for (a) PMT and (b) SiPM measurements with the double-sided CS-1 crystal. The lower bound for FOM calculations (channel 300) was chosen because it was above the threshold for each detector and below the full energy photopeak for ^{137}Cs. Both photomultipliers provide measurements with acceptable FOMs (1.850±0.004 for PMT and 1.601±0.005 for SiPM), but only the PMT is able to resolve the ^{137}Cs full energy peak. ^{60}Co could not be used with ^{137}Cs in this measurement because the decreased resolution meant none of the photopeaks were resolvable in either photomultiplier. All known sources are labeled in the plots. 59

23 Range of waveforms for simultaneous PMT and SiPM measurements of thermal neutron interactions. The dark line indicates the average waveform and the shaded areas indicate the range of possible measurements. Inset (a) shows a pair of individual waveforms when the PMT integral is lowest and SiPM is highest while inset (b) shows the opposite. This variation in energy measured indicates whether the interaction site was closer to the PMT or SiPM. Gamma ray interactions follow the same trend. 61

24 Two-dimensional histograms of PSD ratio and uncalibrated energy with intensity scaled logarithmically for combined data from PMT and SiPM measurements with the double-sided CS-1 crystal. The lower bound for FOM calculations (channel 300) was chosen because it was above the threshold for each detector and below the full energy photopeak for ^{137}Cs. Combining the waveforms also improved the FOM to 2.117±0.003. 62

25 Thermal neutron tracks within CLYC showing the paths taken by thermal neutrons within the crystal. It demonstrates that thermal neutrons are captured very quickly within the material. 67

Figure Page

26 Changes in the neutron peak position as a function of detector rotation. For this measurement, the crystal was moved from a cool environment (∼24°C) to a warmer environment (∼33°C) and not provided time to reach thermal equilibrium. The dotted lines indicate the best linear fit for SiPM 0 ($R^2 = 0.31$) and SiPM 1 ($R^2 = 0.72$). 70

27 Changes in the neutron peak position as a function of detector rotation. For this measurement, the crystal was kept in the warm environment (∼33°C) overnight and received sufficient time to reach thermal equilibrium. The dotted lines indicate the best linear fit for SiPM 0 ($R^2 = 0.86$) and SiPM 1 ($R^2 = 0.92$). 71

28 Top down cross section of the additional shielding added for the final measurement (not to scale). Borated polyethylene and cadmium were added to reduce the number of indirect neutrons scattering into the detector. 72

29 Changes in the neutron peak position as a function of detector rotation. For this measurement, the crystal was again allowed sufficient time to reach thermal equilibrium and additional shielding was introduced so that neutrons could only come from the direction of the source. The dotted lines indicate the best linear fit for SiPM 0 ($R^2 = 0.91$) and SiPM 1 ($R^2 = 0.95$). 72

30 This implementation of the K-Means clustering algorithm is not able to discriminate between neutron and gamma events. 80

31 DBSCAN applied to the data is able to identify three clusters corresponding to gamma events (orange), thermal neutrons interacting with ^{6}Li (green), and thermal neutrons interacting with ^{35}Cl (red). 81

32 Gaussian Mixture algorithm applied to the data set. When 10 or more gaussian components are used, this algorithm returns a density-based clustering assignment and is able to identify the gamma region as well as the region corresponding to thermal neutrons interaction with ^{6}Li (green cluster in neutron region). 82

33 Results of Gaussian Mixture applied to the entire data set. Subplot (a) shows the total response from the scintillator with all full energy gamma peaks identified, as well as the thermal neutron peak corresponding to the ^{6}Li interaction. Subplot (b) shows the same energy range with all of the events tagged as gamma ray interactions removed. On this semilog plot the interactions of thermal neutrons with ^{35}Cl can be seen slightly above the noise at ∼493 keVee. 84

34 Result of DBSCAN algorithm applied to the dataset with gamma interaction events removed. Subplot (a) shows three clusters identified by DBSCAN. The red and blue clusters correspond to thermal neutrons interacting with ^{6}Li and ^{35}Cl, respectively. The green cluster is right on the edge of the gamma region and likely corresponds to gamma ray interactions that were not identified during the Gaussian Mixture analysis. Subplot (b) shows energy histograms of the two neutron clusters (in blue and red) laid over the results of the Gaussian Mixture analysis (in gray) with gamma events removed for comparison. After DBSCAN only the neutron clusters remain and in this histogram the neutron events are clearly identified and noise is greatly reduced. 86

35 Gaussian Mixture and DBSCAN are applied to another data set recorded using a CLYC-7 crystal (grown with 99% enriched ^{7}Li). Due to the lower content of ^{6}Li, the cluster and peak corresponding to thermal neutrons interacting with ^{35}Cl are strengthened while those corresponding to ^{6}Li are diminished. 88

36 Gaussian Mixture and DBSCAN are applied to a data set recorded using a CLYC-7 crystal (grown with 99% enriched ^{7}Li) exposed to a continuous energy neutron source (AmBe). 91

37 Main programming loop of the temperature controller built for this experiment. 96

Figure Page

38 Uncalibrated energy spectra for measurements of a combined gamma ray and neutron environment using a CLYC-7 crystal at temperatures ranging from -20°C to 40°C. The full energy photopeaks and Compton edge are visible at all temperatures. At lower temperatures the full energy photopeak is less resolved, and appears at lower energy channels. 97

39 Uncalibrated energy resolution of the ^{137}Cs photopeak for each temperature examined. Increasing temperature, improved the energy resolution with the best value (8.55±0.09%) obtained at 40°C. 98

40 Averaged gamma ray waveforms normalized to the -20°C waveform. Peak amplitude decreases slightly with increasing temperature, but the integral of each waveform is greatly increased with increasing temperature. 99

41 Averaged neutron waveforms normalized to the 40°C waveform. Peak amplitude and integral of each waveform is increased with increasing temperature. 100

42 CLYC-7 PSD ratio plotted against uncalibrated energy at -20°C. At this temperature the only feature visible is the photopeak due to ^{137}Cs. 101

43 CLYC-7 PSD ratio plotted against uncalibrated energy at 0°C. At this temperature the ^{137}Cs photopeak is the only identifiable feature, but it is more defined than it was in the -20°C measurement. 101

44 CLYC-7 PSD ratio plotted against uncalibrated energy at 20°C. At this temperature, the ^{137}Cs photopeak is more clearly separated from the gamma rays in the Compton continuum and now neutrons from the ^{35}Cl(n,p)^{35}S interaction are visible. 102

45 CLYC-7 PSD ratio plotted against uncalibrated energy at 40°C. At this temperature, the ^{137}Cs photopeak is very clearly defined, as is the cluster corresponding to the ^{35}Cl(n.p)^{35}S interaction. 102

List of Tables

Table		Page
1	Research Objectives	6
2	Identification and physical properties of CLYC crystals	50
3	Comparison of energy resolutions for PMT and SiPM measurements for each Single-Sided CLYC crystal	54
4	Temperature controller components	95

ENABLING MOBILE NEUTRON DETECTION SYSTEMS WITH CLYC

I. Introduction

Historically, the detection of neutrons and the analysis of neutron spectra has been challenging due to their neutral charge and limited interaction with matter. This is the primary reason why the neutron was not observed until 1930 by Bothe and Becker and later identified in 1932 by Chadwick [1]. The neutral charge complicates detection because it does not allow a neutron to directly ionize matter, which is how radiation is normally measured in a detector. Instead, neutrons must either be scattered by a light nucleus that can recoil with sufficient energy to ionize nearby atoms or undergo a nuclear reaction that produces charged particles like alphas, protons, and gamma rays that can then cause ionization [2].

These methods work well for detecting neutrons, but often cannot determine the energy of the neutrons detected. In recoil detectors, the energy information is generally lost because only the first neutron scattering event is measured and the amount of energy transferred to the recoil nucleus ranges from zero up to the maximum possible depending on the angle of incidence (with a head on collision transferring the most energy) [1, 2]. As a result, the detector does not usually measure the full energy of the neutron [2]. Detectors that rely on nuclear reactions to detect neutrons often surround the detector with moderating material to increase the interaction probability for fast neutrons, which also removes information about the energy of the neutron before it is thermalized [2]. Some techniques use a series of moderators of various thicknesses and measure detector responses for each thickness to then unfold a neutrons energy spectrum but this requires multiple measurements and post processing

to characterize a neutron source [3].

In recent years, Cs_2LiYCl_6:Ce (CLYC) has shown promise as a scintillator sensitive to both gamma rays and neutrons through neutron interactions with ^{6}Li and ^{35}Cl. The most important property of these scintillation photons is that the decay time for excitation in the crystal due to neutrons is longer than the decay times for excitation by gamma rays. This means the waveforms generated by the photomultipliers will be shaped differently and pulse-shape discrimination will allow identification of the interaction event that caused the scintillation. The reason why these interactions have different decay times and waveforms is discussed in Sec. 2.2 and the method of discriminating between the two interactions is described in Sec. 2.4.

Possibly the most interesting property of CLYC is the ^{35}Cl (n,p) interaction (see Sec. 2.2). This interaction has been shown to have a linear response to neutrons and may become the basis for generating neutron spectra [4, 5]. It may ultimately be possible to create a neutron detector that is also sensitive to gamma rays and able to measure the neutron energy spectra for sources in real time without the need for post-processing or complicated unfolding methods.

1.1 Applications of Neutron Detection with CLYC

Neutron detectors are important in many industrial applications, but they are especially important for national security and combating the threat of nuclear weapons [6]. Prior to September 11, 2001, military systems were the only delivery threat considered for nuclear weapons. Since then, the threat has expanded to include commercial carriers and civilian transportation systems [7]. The threat is also no longer limited to nuclear warheads, but now includes improvised nuclear devices (IND), smuggling of special nuclear material (SNM), and radiological dispersal devices (RDD) [6, 7, 8]. CLYC might be useful in determining the presence of all these potential

threats.

At present, CLYC can be used to detect and differentiate between both gamma rays and neutrons, so it already has applications in any scenarios requiring only the detection of neutrons without concern for neutron energy information. It can also produce gamma spectra with better energy resolution than NaI(Tl) [9]. With a little design effort, CLYC can be developed into a commercial product that counts neutrons and identifies radioisotopes by their gamma signatures. However, with a bit more development, CLYC could be used for nuclear security applications where the determination of the spectrum of neutrons is important.

For nuclear warheads and INDs, SNM is the most important ingredient and poses one of the largest nuclear proliferation threats. Thus, the ability to detect and identify SNM is probably the most important way to limit smuggling and IND threats. Both weapon-grade plutonium (WGPu) and highly enriched uranium (HEU) emit neutrons, though at significantly different rates: $\sim$60,000 neutrons/s around 1 MeV for 1 kg WGPu and $\sim$3 neutrons/s for 1 kg of HEU [10]. They also both emit significant amounts of gamma rays, though these can be shielded [10]. Detecting WGPu with neutrons is particularly attractive because of the high neutron flux from the plutonium and the low background neutron flux from the environment [6, 7]. The fact that very few commercial neutron sources are transported means that any neutrons detected above the background level would be of concern and require additional screening [6].

HEU poses a bigger threat because the neutron count is so low and the gamma rays can be shielded. However, active interrogation techniques could be used to identify hidden HEU by inducing fission and then detecting both the prompt and delayed neutrons produced [10]. Developing the ability of CLYC to measure the neutron energy spectrum will allow easy identification and separation of the neutron source and the neutrons generated by fission in the HEU.

A CLYC detector that is able to generate accurate neutron energy spectra will also be able to identify neutron shielding. This would be accomplished by placing the neutron source and CLYC detector on opposite sides of the object being interrogated and first detecting whether any neutrons penetrate through the object and second measuring the energy of any that do. These measurements would be used to determine how much thermalization there was due to low Z material which might indicate neutron shielding [10]. This could similarly be done with photons to find high Z material which could be indicative of gamma shielding or SNM [10].

By detecting neutrons and gammas concurrently, a single crystal of CLYC or an array of CLYC crystals could detect a wide range of nuclear and radioactive material threats. The gamma sensitivity and energy resolution would enable radioisotope identification and possibly identify SNM sources without gamma shielding. With active interrogation this sensitivity would allow the same crystal to detect high Z material. The ability to detect and discriminate neutron sources would allow for simple neutron counting, but development of a response function for the ^{35}Cl (n,p) reaction with fast neutrons would quickly identify WGPu by the energy of its emitted neutrons and HEU by the fission neutrons released during active interrogation. Furthermore, the neutron energy information could be used with active interrogation to detect neutron shielding and estimate the amount of shielding present. The fact that gamma rays and neutrons can be measured at the same time and separated easily means that passive and active scanning of a target can be accomplished much faster, with fewer steps, and possibly with fewer detectors.

One important thing to keep in mind is that even though detection systems may fail to prevent an attack, if they are credible, or believed to be so, they can still reduce the overall impact of an attack. This is because an credible detection system would force a belligerent to either use weapons with small amounts of SNM or radioactive

material or detonate a weapon at or outside of the detection area. This pushes the threat further from the most populated areas, and while the impact would be devastating, it would be reduced from the worst-case scenario [10].

Having mobile or portable detection systems would allow this detection area to be even further removed from population centers. With further refinement, a CLYC-based detection system could be designed to perform all of the applications outlined in this section. Taking advantage of new, smaller electronics, much of the data collection and processing can be built into the detector in a single unit with a size that is small enough to carry by hand or transport by unmanned vehicle.

One very real threat to our ability to provide a credible detection system is the ongoing shortage of helium-3, which is necessary for our current radiation portal monitors [11]. It is possible that other detectors like CLYC will be necessary to continue our credible detection system and also improve upon it, especially through the use of mobile detectors on unmanned vehicles.

1.2 Research Objectives

The main objective of this research is to further the development of mobile and portable neutron detection systems utilizing scintillating CLYC crystals. The individual research objectives (highlighted in Table 1) pursue that goal by exploring the feasibility of low-cost data acquisition systems for pulse shape analysis, comparing photon collection equipment (SiPM vs PMT), utilizing a unique CLYC crystal with two optical windows to determine source direction, developing a methodology to use unsupervised machine learning algorithms to analyze measurement data, and studying the effect of temperature on the waveforms within a CLYC crystal using lithium enriched to 99% ^{7}Li (CLYC-7).

Table 1. Research Objectives

Research objectives	Chapter
I. Low-Cost Pulse Shape Analysis	3
II. Comparison of PMT and SiPM Measurements	4
III. Source Direction Information from Double-sided Crystal	5
IV. Cluster Algorithm Analysis	6
V. Temperature Effect on CLYC-7	7

The first two objectives directly support the development of a mobile and/or portable system by analyzing possible methods for decreasing the size, weight, and power requirements of a CLYC-based detection system. The first of these objective is to show that pulse shape analysis using a CLYC scintillator can be done with a small, lightweight, and low power digital data acquisition system using commercial off-the-shelf components. This type of data acquisition system will allow for the creation of a small detector system that does not require external support.

The second objective is to compare measurements made with a SiPM to those made with a traditional PMT. This objective will quantify the difference in performance between the two photomultipliers and indicate whether SiPMs are suitable for use with CLYC. Since SiPMs are significantly smaller and require much lower voltages than PMTs, they can further decrease the size and power requirements of a detection system.

The remaining objectives are not concerned with making CLYC more mobile or portable, but rather explore ways to make such a system more useful. The third objective is to analyze a double-sided CLYC crystal to explore whether source direction information can be determined by comparing measurements taken at either optical window. If successful, this objective will allow a portable CLYC system to indicate the direction of a neutron source instead of just detecting its presence.

The fourth objective is to compare cluster analysis algorithms from open-source

Python libraries to find the best method for identifying and analyzing interactions occurring within the crystal. These clustering algorithms might be simple enough to run on the detection system itself, allowing the system to group data into useful clusters for subsequent user identification.

The final objective is to compare the effect of temperature on a CLYC crystal grown with lithium enriched in ^{7}Li (99%). This objective will indicate the best range of temperatures for operating detectors with CLYC-7. This is important as neutron detectors like CLYC may find use in many environments (from extreme hot and cold temperatures found in space to terrestrial operation in hot deserts or frozen tundra) and whether such operations will require heating or cooling for the detector must be determined.

All of these objectives are accomplished experimentally by studying multiple CLYC crystals in different detector configurations and analyzing the response to various neutron and gamma sources. The second column of Table 1 indicates the corresponding chapter for each research objective. Each of these chapters will have a detailed description of the experimental procedure for the corresponding research objective as well as a short discussion of any previous research and brief explanations of background theory necessary to understand the experiment. Detailed background information for all research objectives can be found in the next chapter (Ch. II).

II. Background

2.1 Neutron detectors

Most current methods of detecting neutrons rely on a nuclear interaction between neutrons and a target nuclei to generate charged particles, such as protons and alphas, or gamma rays that can then be detected using standard radiation detectors. The best interactions will have high cross sections to allow for small detector sizes and a high Q-value which will be transferred to the products and make the task of discriminating between neutron and gamma ray events easier [3].

For the detection of thermal neutrons three main interactions are often employed,

$$n + {}^{10}B \rightarrow \begin{cases} {}^{7}Li + \alpha & (Q = 2.79\,MeV) \\ {}^{7}Li + \alpha & (Q = 2.31\,MeV) \end{cases}, \tag{1}$$

$$n + {}^{6}Li \rightarrow t + \alpha \ (Q = 4.78\,MeV), \tag{2}$$

and

$$n + {}^{3}He \rightarrow t + p \ (Q = 0.76\,MeV). \tag{3}$$

All of these interactions have large cross sections for thermal neutrons: 3840 barns for ^{10}B, 940 barns for ^{6}Li, and 5330 barns for ^{3}He.

Boron is used in BF_3 tubes where boron trifluoride, enriched in ^{10}B, acts as both the conversion medium for slow neutrons and a proportional gas. Ideally, the BF_3 tube detector exposed to thermal neutrons will have two peaks centered at 2.31 MeV and 2.79 MeV corresponding to the two reactions in Eq. 1. However, one of the limitations of BF_3 tubes is the long range for alpha particles in the gas ($\sim$1 cm)

which allows the alphas to interact with the walls and decreases the amplitude of the measured pulse [3].

^{10}B has also been used to line proportional counters and create a conversion layer that interacts with the neutrons before they enter the detector. In this configuration, however, only one of the products will enter the detector. This lower energy for each pulse may make discrimination more difficult. Similarly, boron has been added to scintillators to convert neutrons inside the scintillator to charged particles that can be detected. Unfortunately, this method also has a diminished ability to discriminate neutrons from gammas because gammas can deposit their full energy in the solid scintillator, compared to a small fraction of their energy in BF_3 tubes and because organic scintillators will produce more photons from electrons than charged particles. Thus boron-loaded organic scintillators cannot be used to discriminate neutrons from gammas by pulse amplitude. An alternative is to load boron into a liquid scintillator and use pulse-shape discrimination to identify neutron events from gamma events [3].

^{6}Li is commonly used in scintillators since there are no stable proportional gases that contain lithium. Crystalline lithium iodide doped with europium has a light output of approximately 35% of NaI(Tl) and a scintillation decay time of 0.4 μs. Quenching of the charged particles is low in lithium iodide so that the 4.78 MeV from the thermal neutron interaction with ^{6}Li would have the same light yield as a 4.1 MeV electron. Discrimination of neutrons and gammas is accomplished by comparing pulse-height. Lithium has also been added to liquid scintillators where it can be used with pulse-shape discrimination to identify neutron and gamma events [3].

^{3}He is used as a conversion medium and proportional gas in the same way as BF_3. ^{3}He proportional counters also suffer from wall effect interactions and typical techniques to decrease the energy lost to the walls include increasing the pressure of

the helium and introducing a heavier gas to increase the stopping power and limit the range of charged particles in the detector [3].

Fast neutron spectra can be measured by placing these slow neutron detectors in polyethylene spheres of various diameters known as Bonner spheres. These spheres will moderate the incident neutron energy where the amount of moderation is dependent on the thickness of the sphere. By taking multiple neutron measurements with a variety of sphere thicknesses, a neutron spectrum can be unfolded for the higher energy regimes [3].

2.2 CLYC

Structure and growth

CLYC is a cubic elpasolite crystal ($a = 10.4857\,\text{Å}$) with a density of 3.31 g/cm^3 [12]. Scintillators with a cubic structure are desirable for their light output efficiency, proportionality and scalability [13]. This is because the cubic structure will produce less thermomechanical stress during single-crystal solidification which means there will be less scattering due to grain boundaries and the possibility of producing large size single-crystals [13]. CLYC is also hygroscopic which requires it to be used in a sealed canister or handled in a drybox [12].

CLYC is grown with the vertical Bridgman method using LiCl, CsCl, YCl_3, and $CeCl_3$ as starting materials [12]. These materials are sealed within silica ampoules under vacuum and heated to 1055 K and pulled at a rate of 0.03 mm/min [12]. Final dopant concentration is $\sim$0.5 mol% Ce^{3+} [12].

Neutron interactions

Neutrons incident on a CLYC crystal will be either scattered, absorbed, or pass through the crystal without interacting. All interactions within the crystal will trans-

fer energy but only interactions involving charged particle or photon emission will be detectable through scintillation.

The most likely neutron interaction in almost all cases is neutron scattering. At low energy this might not be true (see Fig. 1) but as the energy of the incident neutron is increased, scattering will tend to dominate. Neutrons can scatter in two ways: elastically and inelastically. Elastic neutron scattering occurs when a neutron hits a nucleus as if both were hard billiard balls. The incident neutron changes direction and is slowed by transferring energy to the target nucleus which conserves momentum by recoiling. These events do not cause significant scintillation events within the crystal. Only lithium is light enough to have a sizable recoil from a neutron scattering, but the maximum energy transferred to a lithium nucleus in a collision is much less than it is with hydrogen where it is possible for a neutron to transfer its entire kinetic energy to the nucleus [2, 1].

Higher energy neutrons ($\sim$1 MeV and higher) can scatter inelastically. In this case, the incident neutron is absorbed by the target nucleus and then another neutron is emitted with lower energy. The energy in this case has been transferred to the target nucleus which is now in an excited state. When this excited nucleus decays back to its ground state, a gamma ray or internal conversion electron will be emitted that can cause scintillation within the crystal.

Radiative capture is also possible. In this case, a neutron is absorbed by the nucleus creating a new isotope of the same element in an excited nuclear state. When the nucleus decays to its ground state a gamma ray is emitted that may cause scintillation within the crystal. If the final isotope is not stable it may lead to additional decay events that release alpha particles, beta particles and/or gamma rays which can all cause scintillation.

Neutrons can also create a variety of heavy charged particles including protons,

deuterons, tritons and alphas. In these interactions, the neutron enters the nucleus and causes the emission of a charged particle [1]. These charged particles are able to create many electron-hole pairs within the crystal which can create strong scintillation events.

The remainder of this section will consider the interaction cross sections for all major constituents of CLYC to describe the most likely interactions in the thermal, epithermal and fast neutron regimes. The neutron interactions with cerium are not considered since it is only in the crystal as a dopant and will have such a low concentration that any contributions to scintillation will be insignificant.

Lithium

There are two stable isotopes of lithium: ^{6}Li (7.59 at.%) and ^{7}Li (92.41 at.%) [14]. The neutron cross sections for various reactions with ^{6}Li are shown in Fig. 1. The most important interaction for ^{6}Li is the (n,t) reaction,

$$n + {}^{6}Li \rightarrow t + \alpha \ (Q = 4.78\,MeV),$$

which has a very high cross section for thermal neutrons and is also the most likely non-scattering interaction for fast neutrons interacting with ^{6}Li. The Q-value for this interaction is 4.78 MeV which is split between the ^{4}He and triton, and any additional kinetic energy from the incident neutron will be added to the total energy shared between the two reaction products. Since these particles are charged, they can create scintillation within the crystal. Other possible interactions include (n,p) which is about an order of magnitude less likely than (n,t) and (n,γ) which has a very low probability in ^{6}Li.

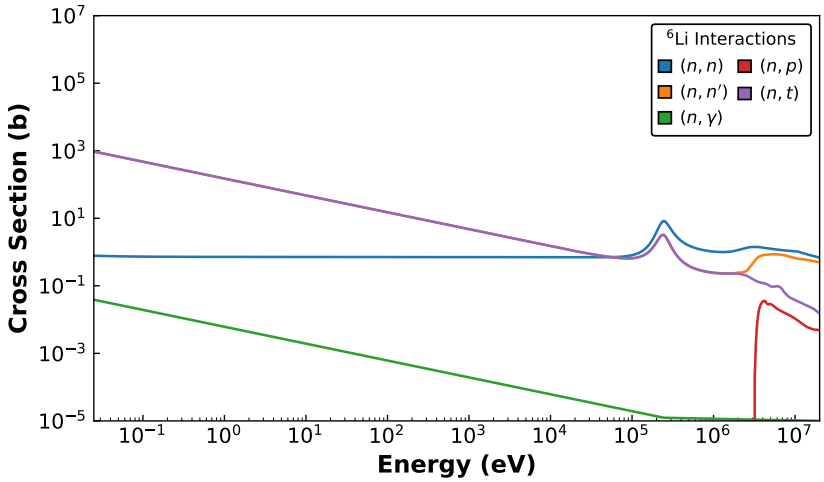

(a)

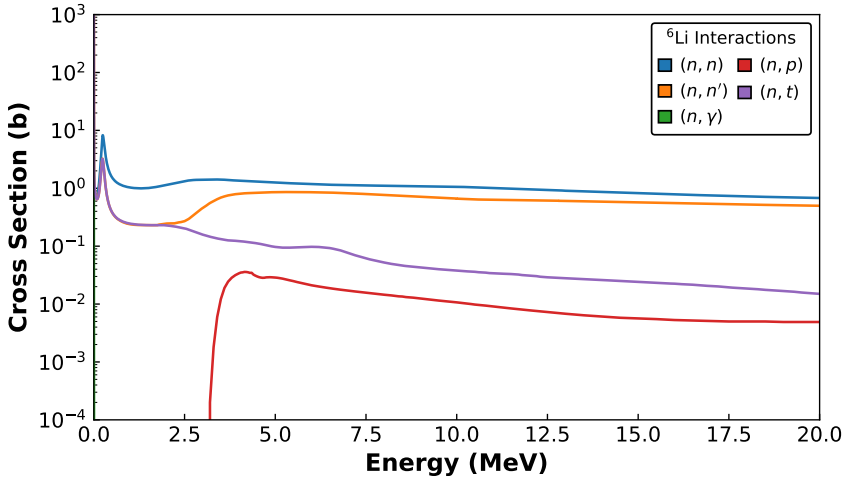

(b)

Figure 1. Neutron interaction cross sections for ^{6}Li across the full neutron energy range with logarithmically scaled energy (a) to show low energy features and linearly scaled energy (b) to show more detail in the fast (>1 MeV) region.

The neutron interactions for ^{7}Li are shown in Fig. 2. There will be some (n,γ) possible with low energy neutrons, but most of the interactions will be due to scattering. Above 10 MeV the (n,d) reaction becomes possible, but it has a very small cross section. Not shown in the plot is the cross section for ^{7}Li (n,nα) which begins

around 3 MeV and reaches its maximum value of 0.3 b at 5 MeV. Often CLYC is grown with lithium enriched in ^{6}Li to increase the opportunity for thermal neutron absorption. However, if fast neutron information is more important, the crystals can be grown using lithium enriched in ^{7}Li to minimize the thermal neutron interaction and focus on the ^{35}Cl (n,p) reaction.

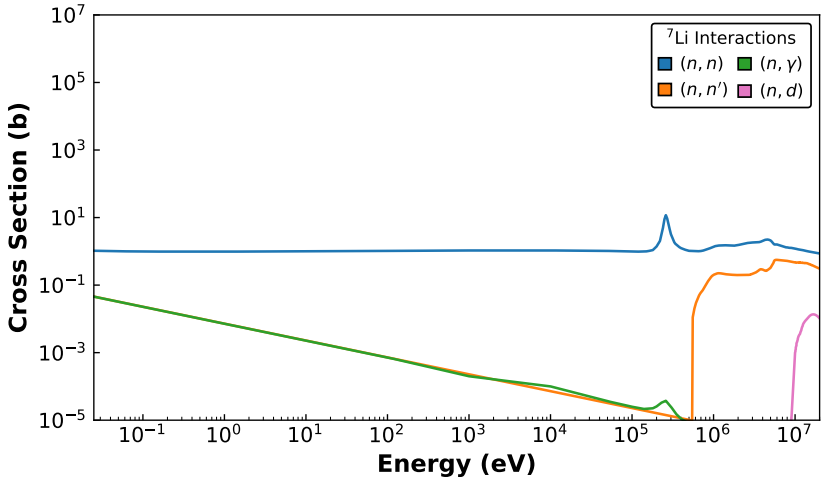

(a)

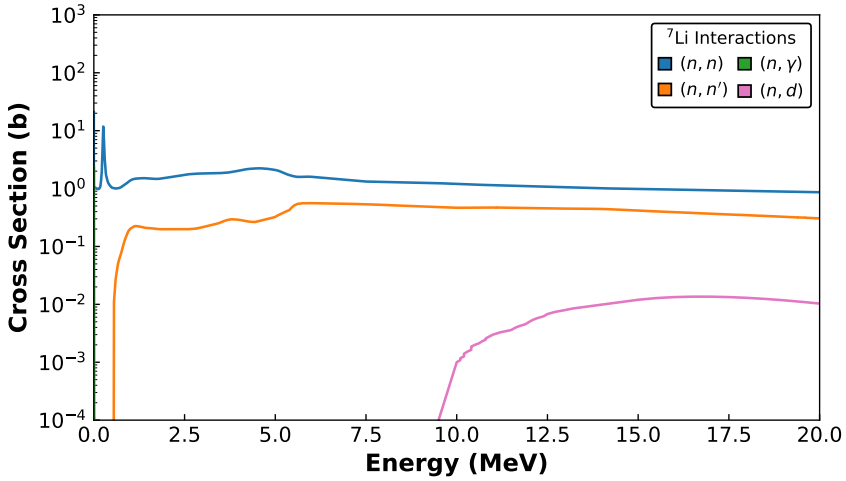

(b)

Figure 2. Neutron interaction cross sections for ^{7}Li across the full neutron energy range with logarithmically scaled energy (a) to show low energy features and linearly scaled energy (b) to show more detail in the fast (>1 MeV) region.

Chlorine

There are two stable isotopes of chlorine: ^{35}Cl (75.76 at.%) and ^{37}Cl (24.24 at.%) [14]. The neutron interaction cross sections for ^{35}Cl are shown in Fig. 3. At low energy (n,γ) is possible, but the most important interaction with ^{35}Cl is the (n,p) reaction,

$$n + {}^{35}Cl \rightarrow {}^{35}S + p \ (Q = 0.616\, MeV),$$

which is possible at all energies and is the most likely non-scattering interaction from 1 MeV until approximately 13 MeV when (n,α) becomes equally likely. Above 15 MeV the (n,p) reaction is again more likely than (n,α). The (n,p) interaction is important because it has been shown to have a linear response to incident neutron energy and may be useful in generating neutron energy spectra [4, 5]. The proton generated through this process will have the energy of the incident neutron plus the Q-value. For example, a 2 MeV neutron would produce a 2.6 MeV proton.

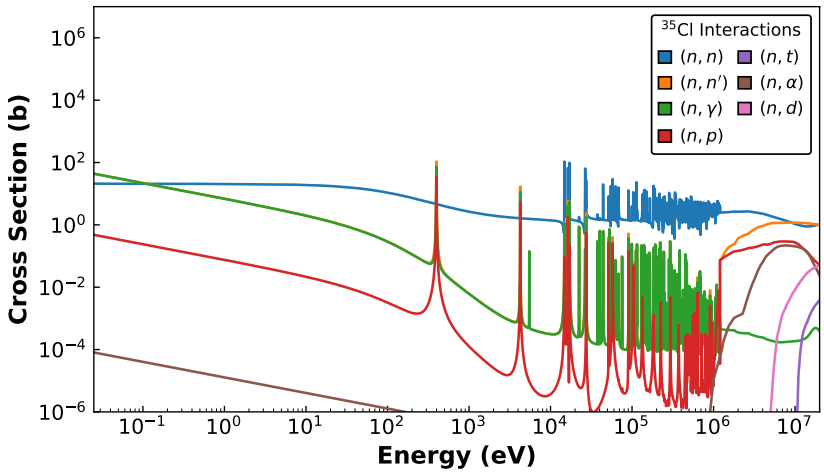

(a)

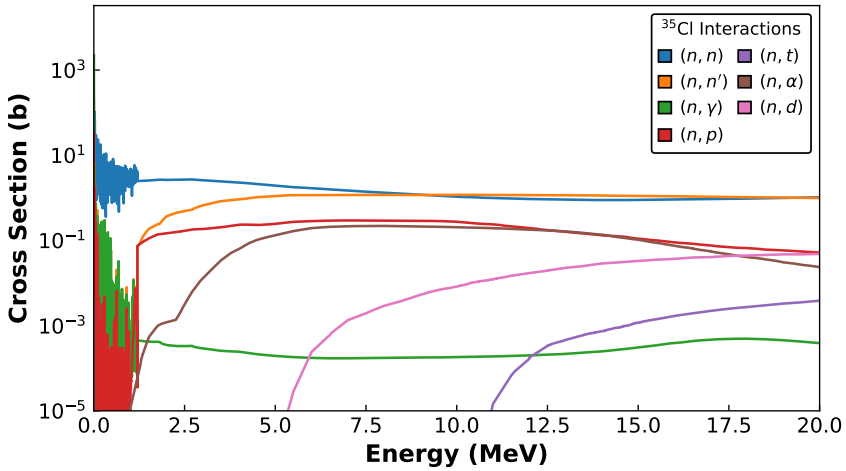

(b)

Figure 3. Neutron interaction cross sections for ^{35}Cl across the full neutron energy range with logarithmically scaled energy (a) to show low energy features and linearly scaled energy (b) to show more detail in the fast (>1 MeV) region.

The neutron interaction cross sections for ^{37}Cl are shown in Fig. 4. The most likely neutron interactions with ^{37}Cl are elastic and inelastic scattering, and while (n,p), (n,α), and (n,d) are possible, they are 10-100 times less likely than scattering. Furthermore, since there are three times more ^{35}Cl nuclei than ^{37}Cl nuclei in natural

chlorine and the ^{35}Cl (n,p) and ^{35}Cl (n, α) cross sections are 10 times larger than any of the non-scattering cross-sections in ^{37}Cl, there will not be a significant contribution to scintillation within the crystal due to ^{37}Cl interactions.

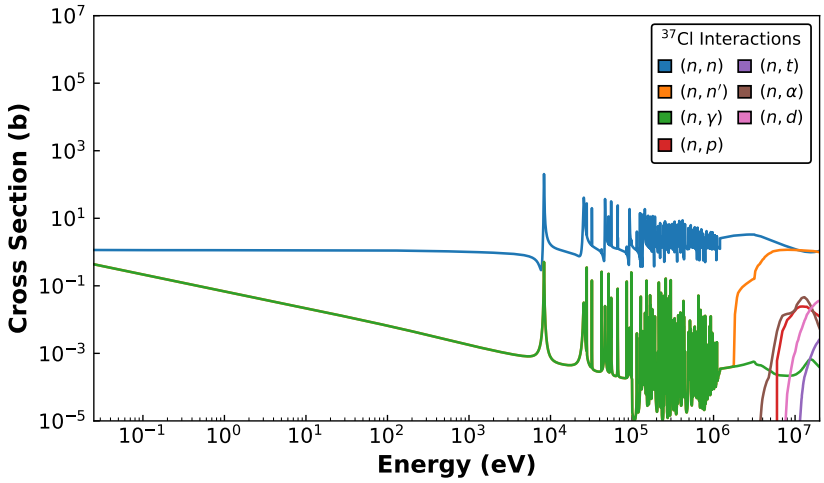

(a)

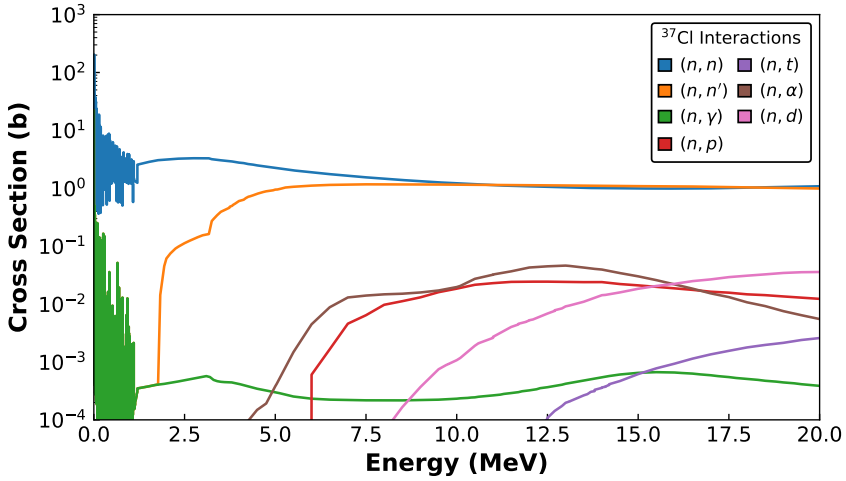

(b)

Figure 4. Neutron interaction cross sections for ^{37}Cl across the full neutron energy range with logarithmically scaled energy (a) to show low energy features and linearly scaled energy (b) to show more detail in the fast (>1 MeV) region.

Cesium

The only stable isotope of cesium is ^{133}Cs and the neutron interaction cross sections are shown in Fig. 5. The only significant interaction is due to neutron capture,

$$n + {}^{133}Cs \rightarrow {}^{134m}Cs + \gamma \ (Q = 6.75\,MeV)$$

or

$$n + {}^{133}Cs \rightarrow {}^{134}Cs + \gamma \ (Q = 6.89\,MeV),$$

at low neutron energies. The metastable state, ^{134m}Cs, decays by internal transition with a half-life of 2.9 hours and produces a 127.5 keV gamma ray [15]. The ground state of ^{134}Cs decays by β^- to ^{134}Ba with a half-life of 2.065 years and produces a variety of gamma rays with the most intense being 604.7 keV (97.62%) and 795.9 keV (85.46%) [15].

At higher energies neutron capture becomes much less likely and even though (n,p) and (n,α) are possible they have very small cross sections and will not be a significant contributor to scintillation.

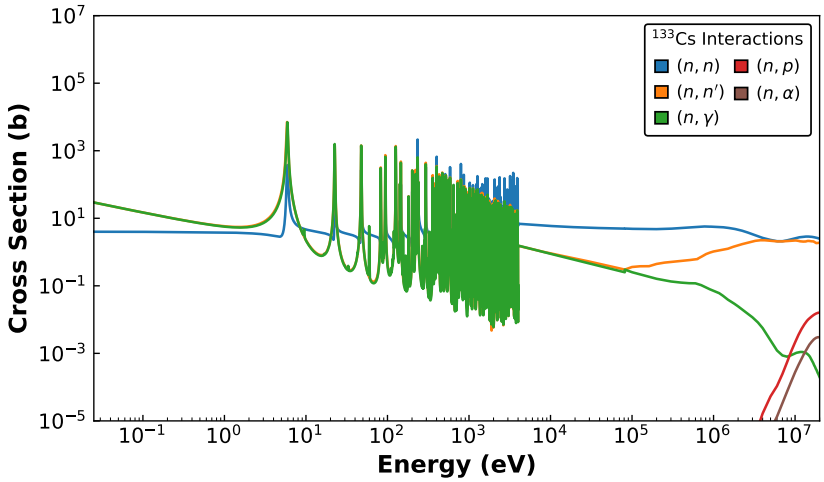

(a)

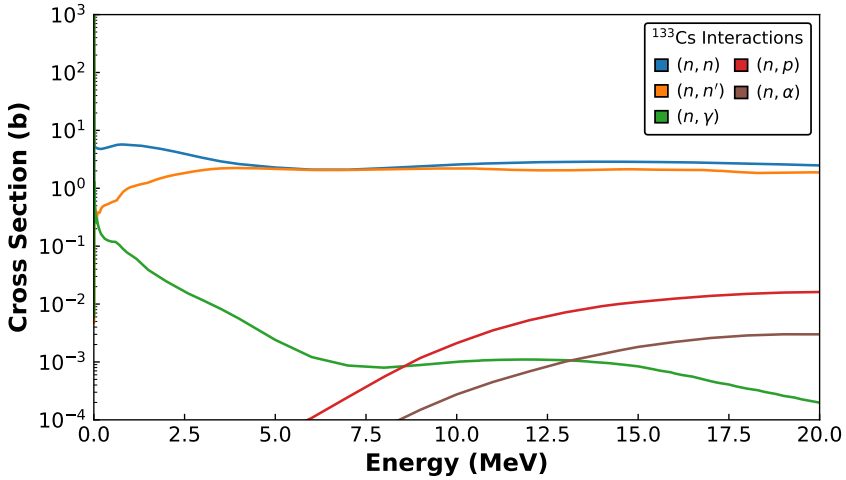

(b)

Figure 5. Neutron interaction cross sections for ^{133}Cs across the full neutron energy range with logarithmically scaled energy (a) to show low energy features and linearly scaled energy (b) to show more detail in the fast (>1 MeV) region.

Yttrium

The only stable isotope of yttrium is ^{89}Y and the neutron interaction cross sections are shown in Fig. 6. The main neutron interaction with ^{89}Y will be through inelastic

or elastic scattering. The most likely non-scattering interaction is neutron capture,

$$n + {}^{89}Y \rightarrow {}^{90m}Y + \gamma \ (Q = 6.75\,MeV)$$

or

$$n + {}^{89}Y \rightarrow {}^{90}Y + \gamma \ (Q = 6.86\,MeV),$$

at low energies, but the capture cross section for thermal neutrons is only ∼1 barn. The metastable state, ^{90m}Y has a half-life of 3.19 hours and can decay by internal transition with a 479.51 keV gamma ray to the first excited state of ^{90}Y, which has a half-life of 250 ps, before decaying again to the ground state producing a 202.53 keV gamma ray [16]. The ground state of ^{90}Y decays by β^- to ^{90}Zr with a half-life of 64 hours and produces a 2.28 MeV gamma ray (99.99%) [16].

The neutron capture cross section decreases rapidly with increased neutron energy. Additional non-scattering interactions are possible at higher energies but will be insignificant due to their low cross sections. Yttrium is not expected to be a significant contributor to scintillation in CLYC.

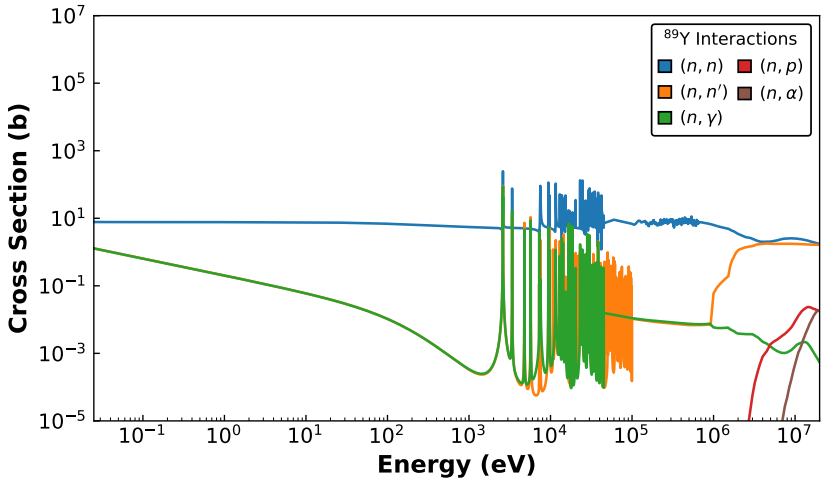

(a)

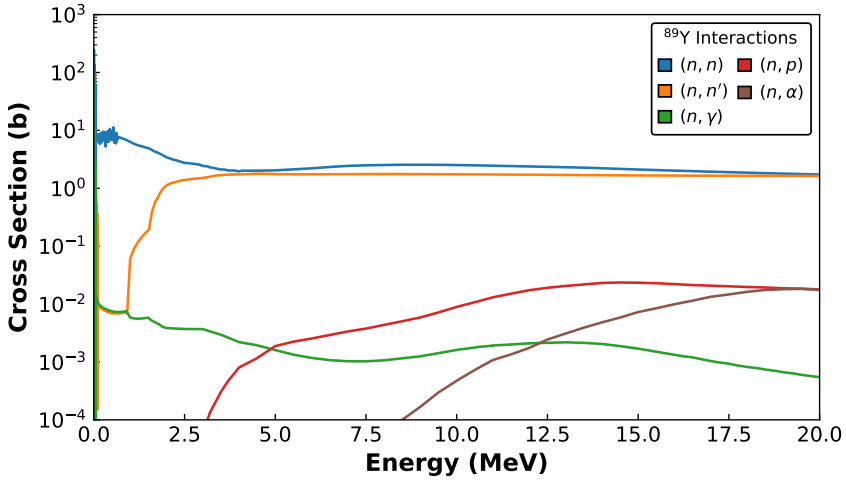

(b)

Figure 6. Neutron interaction cross sections for ^{89}Y across the full neutron energy range with logarithmically scaled energy (a) to show low energy features and linearly scaled energy (b) to show more detail in the fast (>1 MeV) region.

Scintillation process and mechanisms in CLYC

As a scintillator, Ce^{3+}-doped CLYC produces ~20,000 photons per MeV of gamma energy [17, 18] and emits photons in the visible wavelength (250-450 nm) with the

main photon emission at ∼390 nm [12, 17, 19]. Neutrons are not able to directly excite the Ce^{3+} atoms, but rather the charged particles or photons generated by a neutron interaction are responsible for the scintillation. Thermal neutrons, for example, have a high cross section for absorption by ^{6}Li (as seen in Section 2.2) and in the subsequent reaction

$$n + {}^6Li \rightarrow t + \alpha \ ,$$

the triton and alphas share the energy of the reaction ($Q = 4.78\,MeV$) and these charged particles excite atoms within the crystal to create scintillation photons. Since some of the energy is lost to quenching within the crystal the total energy used to create photons is approximately 3.2 MeV [4, 20] which results in approximately 70,000 photons per thermal neutron [17, 18].

In CLYC, the process of scintillation begins with radiation (typically a neutron or gamma ray) interacting with the crystal to form primary electrons [21]. In neutron interactions, charged particles created after the initial interaction generate these primary electrons. The electrons and holes created will relax and thermalize to form electron-hole pairs and one of four mechanisms then transfers energy to the luminescent center (Ce^{3+}) which finally luminesces [21]. These transfer mechanisms include direct electron-hole capture, trapped hole (V_k) centers, self-trapped excitons [21, 22, 23]. Additionally, incident photons may directly excite electrons in the Ce^{3+} ions to create core-to-valence luminescence.

Direct electron-hole capture

Direct electron-hole capture is the mechanism by which prompt luminescence is created when an electron is promoted from the valence band to the conduction band and the free electron and free hole are then promptly (< 1 ns) transferred to a Ce^{3+}

ion [24]. This causes a 4f $\rightarrow$ 5d excitation in Ce^{3+} followed by a 5d $\rightarrow$ 4f emission [19] that produces a broad range of photons from 350 to 450 nm with a peak at $\sim$390 nm [22]. This mechanism produces emission with a fast rise time due to fast ($<$ 1 ns) capture of the electron-hole pairs and a short duration as the excited state of Ce^{3+}has a decay time of 30 ns [19, 21].

Trapped hole (V_k) centers

The process of creating trapped holes is shown in Fig. 7a. If the free electron and free hole are not immediately captured by the Ce^{3+} ions after relaxation, then the hole in the valence band may become trapped and form a complex with two anions sharing the hole known as a V_k center (Cl_2^- in CLYC) [24, 25]. Thermally activated motion allows the V_k center to move around the crystal lattice until it is captured by a Ce^{3+} site where it will form either Ce^{4+} or a Ce^{3+}– V_k associated complex. This new center then captures a free electron which causes an excitation in the Ce^{3+} ion and a 5d $\rightarrow$ 4f transition that emits a photon as in the prompt luminescence process. This is a slower process than direct electron-hole capture because the decay time of the entire process is dependent on the migration speed of the V_k centers within the crystal and transfer speed of electrons to the Ce^{4+} or Ce^{3+}– V_k associated complex in addition to the 5d excited state lifetime of Ce^{3+} [19, 24]. Overall the decay time for this mechanism is between 400 ns [21] and 600 ns [12] resulting in an emission of intermediate duration [19].

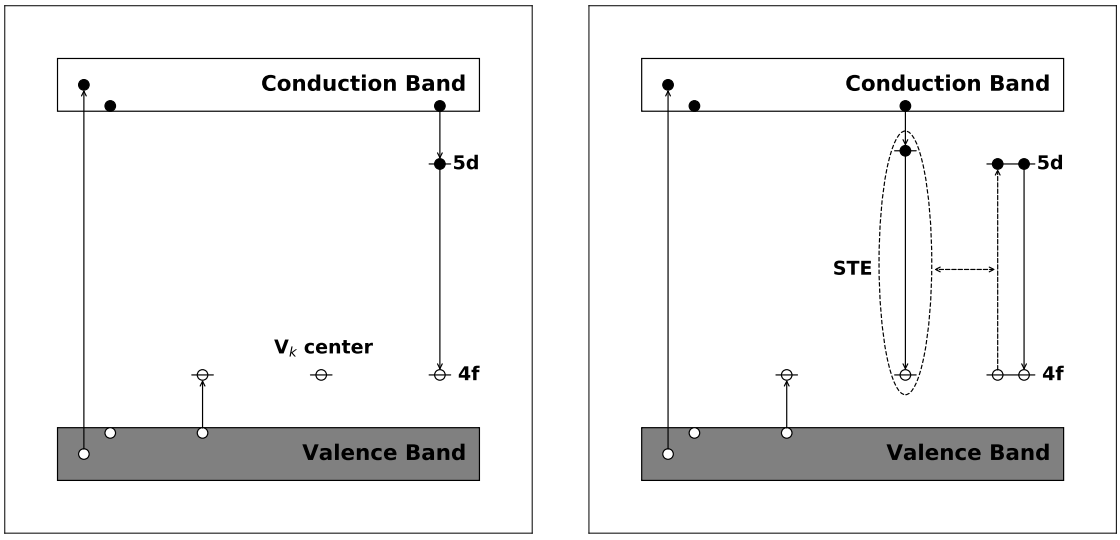

(a) (b)

Figure 7. The process of creating a V_k center (left panel) or self-trapped exciton (STE) and eventual excitation of the Ce^{3+} ion (right panel). Incident radiation (or secondary charged particles in the case of incident neutrons) promotes an electron from the valence band to the conduction band. Any excess energy is lost as the electron-hole pair relaxes so that the hole is at the top of the valence band and the electron is at the bottom of the conduction band. The hole becomes captured between two Cl^- anions to form a V_k center (Cl_2^- in CLYC) . This defect is able to travel around the lattice until it forms a complex with a Ce^{3+} ion in (a) and captures a free electron in the conduction band and emits a photon as it decays from the excited 5d $\rightarrow$ 4f state. If it captures an electron from the conduction band before it forms a complex with Ce^{3+} it will form an STE, as shown in (b). This neutral defect can also travel around the crystal and eventually cause excitation within a Ce^{3+} ion, leading to luminescence, or it can luminesce on its own. It is possible for this STE luminescence to excite the Ce^{3+} if there is an overlap in energies. Diagrams are based on those by Pieter Dorenbos in his paper on scintillation mechanisms in Ce^{3+} doped halide scintillator [24].

Self-trapped excitons

The process of creating self-trapped excitons is shown in Fig. 7b. If the V_k center traps an electron from the conduction band before being captured by a Ce^{3+} ion, it will form a neutral defect known as a self-trapped exciton (STE) that has a higher migration speed than the V_k centers. The STE can move within the lattice and transfer its energy to a Ce^{3+} ion which will then emit photons as before, which is

known as STE diffusion. However, it can also luminesce by itself (STE emission) with a decay time on the order of microseconds. If there is an overlap in STE emission and the energy of the activator ion (Ce^{3+} in CLYC) then radiative energy transfer to the activator is possible [19, 24]. All three routes are possible source of luminescence (STE emission, STE diffusion and STE radiative transfer) and, overall, the STE mechanism has a decay time between 2-6.9 μs and results in an emission of long duration [12, 19, 21, 22].

Core-to-valence luminescence

Core-to-valence luminescence (CVL) occurs when a high-energy photon excites an upper core electron into the conduction band. This transition is short lived as a valence band electron fills the hole and releases a photon [19, 26] with the photons created in CVL ranging from 200-420 nm [21]. CVL is an ultrafast process and the excited state of Ce^{3+} has a decay time of 1-4 ns which results in an emission of very short duration [19, 21, 23].

All of these mechanisms will occur and combine to generate the scintillation photons measured. However, since the CVL process is only possible for high energy photons, it will tend to make the overall intensity of scintillation rise and fall more sharply for gamma ray events than for neutron events and this allows for the possibility of pulse-shape discrimination within CLYC [26].

Quenching in CLYC

Unfortunately, not all of the energy absorbed by the crystal that generates electron-hole pairs will result in scintillation. There are a variety of reasons why this luminescence might be quenched including temperature effects and ionization density.

STE luminescence is one example of temperature dependent quenching. Since

the V_k centers and STEs migrate around the lattice due to thermal activation, it might appear that more thermal energy would increase luminescence as the STEs are more rapidly brought close to the Ce^{3+} ions. The opposite, however, is true because most of the Ce^{3+} luminescence from STE is due to radiative energy transfer from the self-luminescence of the STE, and not STE diffusion [21]. This means the increased thermal energy can excite the bound electron back into the conduction band which reduces this luminescence and even though STE diffusion will now produce relatively more scintillation, it is at the cost of STE luminescence and the overall trend will be less photons per MeV absorbed by the crystal [21, 24]. This is a quenching effect that applies to all interactions and is therefore accounted for through energy calibration of the energy spectra using full energy peaks or other spectral features from known radiation sources.

The major quenching effect to consider in CLYC, however, is due to relative ionization density which means there will be a larger effect for more massive charged particle interactions like alpha particles than for smaller charged particles like protons [5]. This effect is explained using Birks' formula,

$$\frac{dL}{dx} = \frac{S\,\frac{dE}{dx}}{1 + kB\,\frac{dE}{dx}} \ , \tag{4}$$

where $\frac{dL}{dx}$ is the fluorescent energy per unit length, S is the scintillation efficiency, $\frac{dE}{dx}$ is the energy loss per unit length for the charged particle, B is a proportionality constant to determine the density of damaged molecules from the energy lost per unit length ($\frac{dE}{dx}$), and k is the fraction of these damaged molecules that will cause quenching [3].

We can use this formula to consider an electron and an alpha particle. In the case of an electron the value $\frac{dE}{dx}$ is relatively small ($\ll 1$) and the denominator of Eq. 4 reduces to unity which gives us the relationship,

$$\frac{dL}{dx} = S\frac{dE}{dx} \ , \tag{5}$$

which tells us that the fluorescent energy is proportional to the energy lost by the particle and the scintillation efficiency [3]. Furthermore, the light generated per unit of energy loss,

$$\frac{dL}{dE} = S \ , \tag{6}$$

is constant which means each unit of energy lost will create the same intensity of light [3].

With an alpha particle, however, the energy loss per unit length is much larger ($kB\frac{dE}{dx} \gg 1$) due to the increased size and charge on the alpha and Eq. 4 reduces to

$$\frac{dL}{dx} = \frac{S}{kB} \ . \tag{7}$$

This indicates that the light generated per unit length will always be less than the expected output from an electron of the same energy.

As an example, the ^{6}Li (n,t) reaction discussed in Sec. 2.2 has a Q-value of 4.78 MeV and one might expect to measure a scintillation amplitude equivalent to a 4.78 MeV gamma ray. However, when the energy is calibrated to known gamma sources, the peak in the measured energy spectrum attributed to thermal neutrons is $\sim$3.2 MeV because the light generated by the alpha particle is quenched [5]. This is due to the high ionization density created by the alpha particle as it stops quickly within the crystal.

The amount of quenching is typically characterized as a ratio of measured energy to the expected energy, which is called the α/β ratio [3]. For thermal neutrons in CLYC this ratio is approximately 0.67 [4]. One benefit with the ^{35}Cl (n,p) reaction is

that $\frac{dE}{dx}$ is much lower for protons than alpha particles which results in an α/β ratio in the range of 0.84-0.89 [4].

Despite the quenching losses, the ^{6}Li (n,t) reaction is useful for detecting and identifying thermal neutrons because the energy split between the alpha particle (2.05 MeV) and triton (2.73 MeV) is always the same [27]. However, the reaction becomes much more complicated when it occurs with fast neutrons. In this case the energy partition between the alpha particle and triton depends on the angle of emission for each particle [4, 27]. Since alpha particles are more quenched than tritons the fast neutron interaction with ^{6}Li will generate a range of scintillation responses depending on how much of the energy was transferred to the alpha particle [4]. For example, consider a 1 MeV neutron that undergoes an (n,t) reaction with ^{6}Li that creates an alpha particle and triton that share 5.78 MeV. If all of the energy went to the alpha particle and the α/β ratio were 0.67 then a scintillation equivalent to 3.87 MeV would be measured. If, however, all of the energy went to the triton and the quenching α/β ratio were 0.88, then a scintillation equivalent to 5.09 MeV would be measured. The result is that a continuum would be produced in the energy spectrum from 3.87 MeV to 5.08 MeV instead of a strong peak.

2.3 Detector system

In this research, CLYC crystals will form detector systems in two primary configurations using either a PMT or a silicon photomultiplier (SiPM) array. Both of these configurations are shown in Fig. 8. The PMT setup is the simplest and only requires the crystal to be placed on the PMT with some optical grease and an external high voltage power supply to provide -1000 V. The output signal is measured directly from the PMT and is not modified in order to preserve the difference in pulse shapes. To use a SiPM array requires the crystal to sit on the array with optical grease to in-

crease the light transfer. This array is plugged into an interface circuit board which is connected to a control board that provides all connections to power supplies and the data acquisition system. Three voltages are required in this configuration: +5 V and -5 V for the electronic components and up to 30 V for biasing the SiPM. Both detector systems will use a data acquisition system (DAS or DAQ) to measure the output signal and save and/or display results to the user.

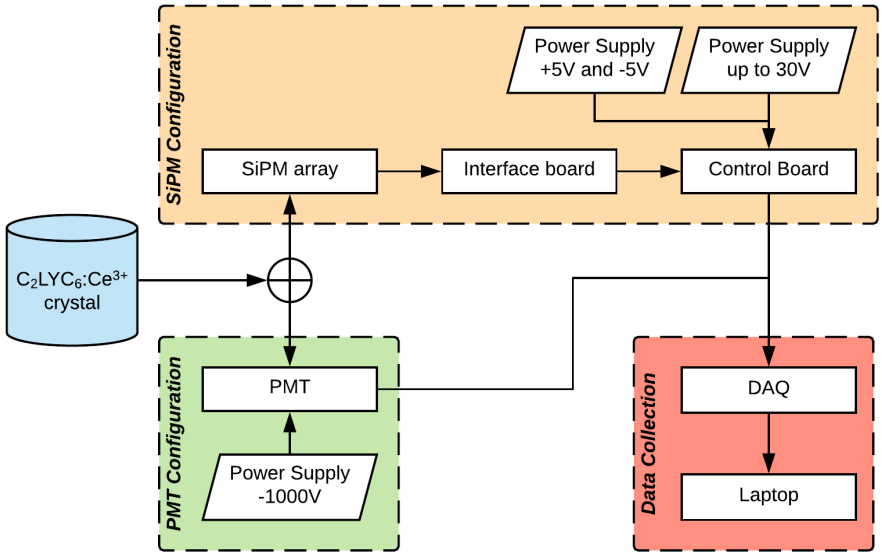

Figure 8. Basic CLYC detector setup. Crystal is either placed directly on a SiPM array or a PMT. For the SiPM configuration the SiPM array is attached to an interface board which is connected to a control board that provides power to the components and provides signal output to a DAQ. For the PMT setup, the signal is read directly from the PMT by the DAQ without any shaping or modification.

SiPM Arrays

A single SiPM is an array of very small avalanche photodiodes (APD) each on the order 10 microns wide. APDs provide an interaction area for incident light to create electron-hole pairs which are then accelerated in opposite directions by a strong electric field. As the electron accelerates it will create more electron-hole pairs, each of which will also be accelerated and an avalanche of electrons is created. If the

voltage is high enough even a single photon interacting in the APD can produce a large output signal and the diode is said to be in "Geiger" mode. In this mode all information is lost about the number of incident photons [3].

The SiPM is designed to overcome this issue by using a large array of tiny APDs so that any individual cell is unlikely to be hit by a photon during a scintillation event. This reduces the chance that any APD will be hit simultaneously by two or more photons and connecting the arrays in parallel will generate an analog signal with an amplitude that is proportional to the number of photons detected [3].

A SiPM array is an array of SiPMs (each referred to as a pixel and consisting of thousands of APDs) usually ranging from 2x2 up to 12x12. These arrays are connected to an interface and control board and in some cases individual pixels can be read, though most often the entire array is read in summation mode so that the array behaves as if it were a large, single SiPM pixel.

2.4 Pulse-shape discrimination

Waveform analysis methods

The goal of waveform analysis is to define a method to determine a value (PSD ratio) for any given waveform that can then be used to determine what interaction generated the waveform. Averaged waveforms for neutron and gamma events in CLYC are shown in Fig. 9. There are several simple methods for calculating a value for PSD ratio based on the prompt, delayed and total pulse components: prompt to total, delayed to total, or prompt to delayed.

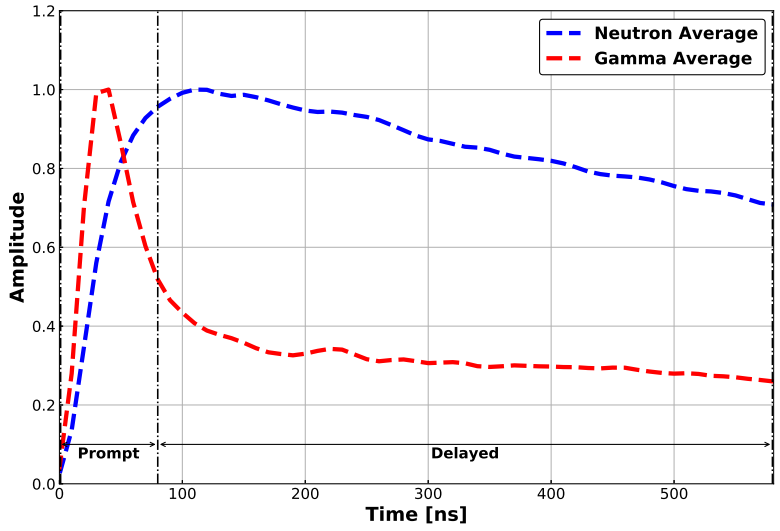

Figure 9. Demonstration of pulse-shape discrimination windows using average waveforms for gamma and neutron pulses in CLYC.

The prompt term refers to the total value of the discrete points in the first portion of the waveform. The delayed term is the summation of all remaining points in the waveform and the total is the two added together. In practice, these windows are defined such that the duration of the prompt and delayed terms are constant and not dependent on the actual peak location of any individual waveform. The prompt region is generally shorter than the delayed region by an order of magnitude and when the pulse is long (as it is with CLYC) the delayed region will not cover the entire tail of the waveform [28, 29, 30]. Most of the difference in pulse shape occurs early within the waveform and measuring too much of the tail slows down data collection.

It is important to know which method is being used to calculate the PSD ratio because the plots generated are very different for each case. In prompt to total calculations the longer lived pulses (typically neutrons) will have a smaller percentage of their total value in the prompt region and will thus tend to have small PSD ratios, while the short pulses will have higher ratios [28]. The reverse is true in delayed to

total calculations. Prompt to delayed calculations typically use windows of similar width. As a result, these calculations will tend to have large PSD ratios for gamma events since the prompt value will be much larger than the delayed value and neutrons will have a PSD ratio close to unity since the prompt and delayed values will be similar [27, 31]. For an example of PSD ratio plots see Fig. 17 in Ch. III or Fig. 20a in Ch. IV.

Figure of merit

The ability to distinguish these pulses can be quantified by calculating a figure of merit (FOM) for separating neutrons and gammas. This is done by taking a histogram of the PSD ratios (for an example see the inset of Fig. 20a) and identifying the peak that corresponds to gammas (the lower PSD ratio) and neutrons (higher PSD ratio). The FOM can be found using,

$$FOM = \frac{\triangle\mu}{\Gamma_g + \Gamma_n}, \tag{8}$$

where $\triangle\mu$ is the difference between the centroids of the gamma and neutron peaks and Γ_g and Γ_n are the FWHM values for the gamma and neutron peaks, respectively [29]. Larger FOM values indicate a better ability to distinguish between neutrons and gammas.

III. Pulse shape discrimination with a low-cost digitizer using commercial off-the-shelf components

The effort to study the feasibility of using a low-cost digital data acquisition system relying on commercial-off-the-shelf components for pulse shape discrimination with CLYC crystals (Research Objective I) was presented at the *Symposium on Radiation Measurements and Applications* in 2018 and generated a manuscript that was submitted to the journal *Nuclear Instrumentation and Methods in Physics Research Section A* on 11 July 2018. Peer review corrections were received on 2 October 2018, and the revised manuscript was accepted for publication on 19 October 2018. This chapter contains the complete manuscript as published with some additional content that was included in the initial submission but removed as requested by the peer reviewers. This content is included because it was not of interest to the journal but is important for the goals and research objectives of this dissertation.

M. C. Recker, the primary author, prepared the manuscript and collaborated with E. J. Cazalas of the University of Utah (formerly of AFIT) on the experimentation and data analysis. J. W. McClory, of AFIT, provided assistance as the author's research advisor and proofread the manuscript.

3.1 Abstract

Pulse shape discrimination of neutrons and gammas is demonstrated using a FemtoDAQ, a low-cost digitizer that uses commercial off-the-shelf components. This digitizer is paired with a CLYC scintillator coupled to a photomultiplier tube to concurrently detect neutrons and gammas. Python code was written to analyze the detector waveforms to determine the energy deposited and distinguish neutron and gamma events within the CLYC crystal. The energy of each waveform is determined by the summation of the discrete amplitudes recorded by the digitizer for each pulse.

This method is compared to a traditional multichannel analyzer operating with commercial software for validation and shown to produce the same energy spectrum. Pulse shape discrimination is accomplished by measuring and summing the amplitudes of the prompt portion of each waveform (first 80 ns) and the delayed portion (following 500 ns) and then calculating a ratio of the delayed region to the total. This technique was able to clearly distinguish thermal neutron events from gamma events with a figure of merit of 1.42.

3.2 Introduction

Recording waveforms generated by photosensors with enough resolution for meaningful analysis can be challenging and costly. Often these pulses are very short, on the order of nano- to microseconds, and require specialized digitizers or oscilliscopes with high sampling rates ($\geq$100 MS/s) to measure and process the data. In the last few years, the release of single-board computers, such as the Raspberry Pi 3 Model B+ (1.4 GHz quad-core, 1GB LPDDR2 SDRAM [32]) and BeagleBone Black (1 GHz CPU, 512MB DDR3 RAM [33]), that provide powerful computing at very low cost ($\sim$\$50) has created an opportunity for data acquisition systems designed from commercial off-the-shelf components that can compete with more expensive instruments [34, 35, 36].

One of these data acquisition systems is the FemtoDAQ, which uses a BeagleBone Black computer and two custom circuitboards to process and digitize data from silicon photomultipliers and photomultiplier tubes (PMTs) with a minimum sampling time of 10 ns and a sampling rate of 100 MS/s [37]. In addition to the low cost, this digitizer uses a Linux operating system and has a Python library.

This paper will demonstrate the ability of the FemtoDAQ to perform pulse shape discrimination (PSD) of gamma and neutron events within the Cs_2LiYCl_6 (CLYC)

scintillator using a PMT. CLYC is a cubic elpasolite crystal grown using the Bridgman method that has garnered substantial interest since it was first created in 1999 [12]. As a scintillator it interacts with gammas (∼20,000 photons per MeV compared to ∼38,000 photons per MeV with NaI(Tl) and ∼3,500 photons per MeV with cerium activated ^{6}Li glass [3]) and neutrons (∼70,000 photons per thermal neutron) to primarily generate photons with peak emission of ∼390 nm and a decay time of approximately 900 ns for the major component [17]. Thermal neutrons will readily interact with ^{6}Li through the (n,t) reaction creating a ^{4}He and triton that deposit 4.78 MeV of energy into the crystal which, after quenching, is measured as 3.2 MeV electron equivalent (MeVee) [20]. Recent studies have demonstrated that CLYC can detect fast neutrons through the ^{35}Cl (n,p) ^{35}S interaction and that this interaction is linearly dependent on the energy of the incident neutron [4, 31, 38].

Pulse-shape discrimination is possible because photons are generated by three different processes with varying decay times and the fastest of these (core-valence luminescence) only occurs due to excitation by gamma rays [20]. Therefore, the excited states generated within the crystal by gamma events will tend to decay faster, producing optical photons more rapidly than neutron events. As a result, gamma waveforms will tend to have a faster rise time and will decay more rapidly than neutron waveforms.

Previous studies have demonstrated PSD with high cost data acquisition equipment [39] and/or computationally expensive wavelet transforms that require processing after collecting the waveforms [40]. Customization with these devices may require programming in older computer languages or using proprietary software, neither of which are as widely supported as Python. The goal of this research is to demonstrate the possibility of fast PSD using small, relatively inexpensive DAQ equipment that can be used to generate energy spectra and distinguish neutron signals from gamma

signals using customizable code for real-time analysis.

3.3 Experiment

Detector setup

A one inch right cylinder of CLYC, grown by Radiation Monitoring Devices [9] and enriched in ^{6}Li, was placed in a 3D printed housing made from polyactide (PLA) and coupled to a 51 mm ETEL 9266KEB PMT with a spectral range of 290-630 nm and peak efficiency at 350 nm. A high voltage power supply provided -1000 V and a FemtoDAQ LV-2 digitizer from SkuTek Instrumentation was connected directly to the PMT output.

For comparison, the detector output was later connected to an Ortec model 113 preamplifier (200 pF), an Ortec model 572 linear amplifier (200x gain, shaping time 2 μs) and an Ortec 926 ADCAM MCB multichannel analyzer (MCA), in line. Gamma spectra in this configuration were recorded using GammaVision version 6.01.

Digitizer setup

A FemtoDAQ LV-2 digitizer (see Fig. 10) was used to capture the waveforms from the CLYC detector. This digitizer has two input channels, a sampling resolution of 10 ns (100 MS/s) and 14-bit analog-to-digital converters (ADCs) [37]. The FemtoDAQ has a small footprint (approximately 90×90 mm^2) and low height (approximately 50 mm) which makes it especially suited for mobile or portable applications.

The front face has two analog inputs with independent three-way switches for selecting impedances of 50 Ω (used in this experiment), 1 kΩ, or 100 kΩ. It can also provide biasing voltages (10-90 V direct current) for two SiPMs, however, when used with a PMT an external voltage source is necessary [37]. The rear face of the FemtoDAQ has the power input and networking connections. The device is powered

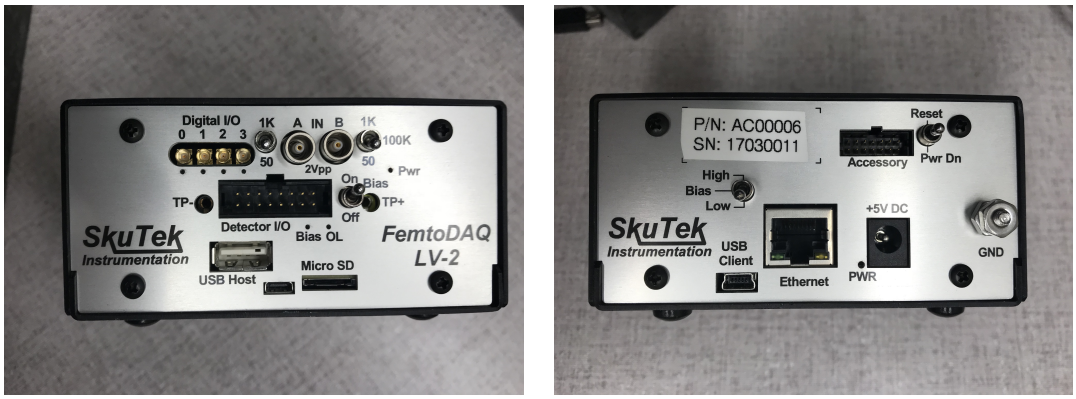

(a) (b)

Figure 10. The FemtoDAQ two channel digitizer showing (a) front and (b) back connections and switches.

with 5 V direct current and communicates through an ethernet cable or networking over USB.

One of the main benefits of using the FemtoDAQ is that all communication is done through secure shell connections to the BeagleBone Black that controls operations within the DAQ. This provides a well known Linux environment and, when combined with the provided libraries, allows the user to develop and write custom data collection software using Python. Coding in a language such as Python is desirable because of its low cost of entry (open source and free), high versatility for many different specialized tasks, operating system independence and extensive codebase that can be used to quickly find examples for most applications.

A custom Python program was written to run on the FemtoDAQ to record the data required for pulse shape analysis. A flowchart for this program is shown in Fig. 11. After initializing the digitizer (ADC) the code requests a waveform and waits until the trigger conditions are met (specifically a minimum voltage). Once triggered, the first 3.5 μs of the waveform are returned by the digitizer as a series of amplitude values (10 ns resolution) resulting in 350 data points.

The energy deposited in the crystal is determined by summing the discrete am-

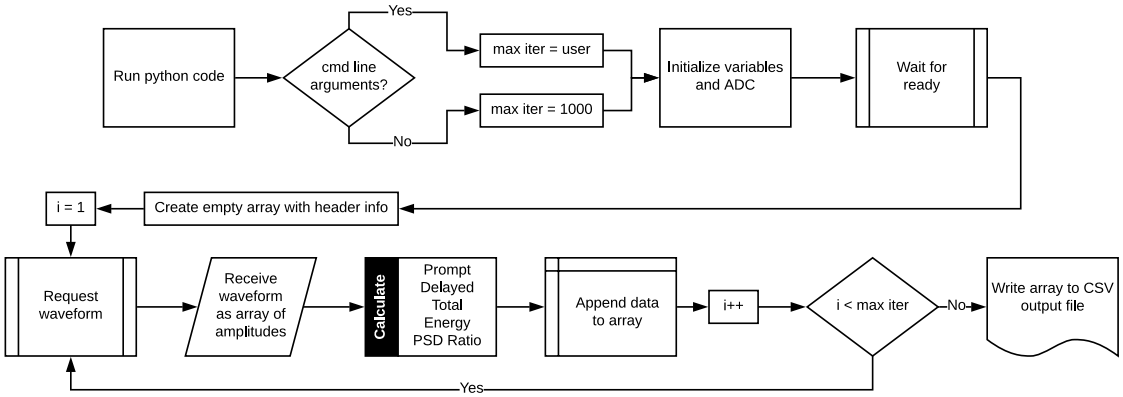

Figure 11. Flowchart diagram of Python code written for collecting pulse shape data with FemtoDAQ.

plitude values over the entire recorded pulse. This energy value is converted to a channel assignment by multiplying it by one less than the number of channels desired (typically 4096) and dividing by some maximum value for the integral.

The PSD ratio is determined by comparing the integral of a prompt portion of the pulse (defined as the first 80 ns and denoted as *prompt* in Eq. 9) and a delayed portion (defined as the next 500 ns and denoted as *delayed* in Eq. 9) using

$$PSD\,ratio = \frac{delayed}{prompt + delayed}. \tag{9}$$

The duration of each pulse region was selected by reviewing previous publications and making small variations on the regions to determine optimum timing to maximize pulse shape discrimination [19, 31, 41].

The prompt integral, delayed integral, PSD ratio, average amplitude of entire pulses, and energy channel assignment are added to an array and the next waveform is requested. Pulses with negative tails that yield a negative energy or PSD ratio are discarded ($\sim$0.3-1.7% of all waveforms). A counter keeps track of the total number of waveforms analyzed (including those that were discarded) and stops requesting waveforms after a predetermined value. Once the waveform request loop is terminated

a function is called to write the array of waveforms to a file on the local FemtoDAQ system.

A second Python code was written that connects to the FemtoDAQ using secure shell protocols and initiates the data collection code. A flowchart for this code is shown in Fig. 12. When the data file is written this code pulls the data file from the FemtoDAQ and displays the data to the user. This code can be setup to repeatedly call the data collection code and provide updated plots with each data file generated adding to the previous data set. 10,000 waveforms per cycle are collected which results in the plots being updated every 40-60 seconds.

Neutron Measurements

To measure neutrons, the detector was placed inside a bismuth (∼10% tin) box approximately 1/2 inch thick to provide gamma shielding. This box was then exposed to a PuBe source within a graphite pile ($48\times48\times72$ in^3) to produce predominantly thermal neutrons (refer to Fig. 13 for the layout of the experiment). Gamma sources (^{137}Cs and ^{60}Co) were positioned within the box with the detector to provide peaks for energy calibration and a known gamma signal to demonstrate the ability to separate gammas and neutrons using the PSD ratio for each waveform. The gamma sources were placed close enough to provide identifiable peaks in the energy spectrum but far enough to not overwhelm the neutron signals. Since the ^{137}Cs source was more active

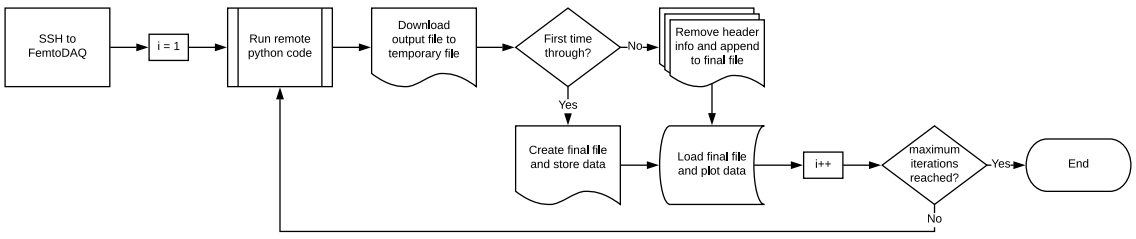

Figure 12. Flowchart diagram of Python code that controls the FemtoDAQ remotely. The third box indicates the code described in Fig. 11.

it was placed further away.

3.4 Results

Energy spectra

The CLYC detector was exposed to two gamma sources (^{137}Cs and ^{60}Co) to verify the energy values measured using the method described above. For each source, 250,000 waveforms were collected by the FemtoDAQ. To demonstrate the accuracy of this method, the ^{137}Cs source was also measured using a traditional MCA and GammaVision software. The resulting energy spectra for ^{137}Cs measured by both systems is shown in Fig. 14. The energy spectra were both normalized to the amplitudes of their full energy peak, all other features (Compton edge and backscatter peak) lined up indicating a close agreement between the two methods of measuring gamma energy (pulse-integral in the case of the FemtoDAQ and pulse-height in the case of the MCA). Several sources have claimed energy resolution as low as 4% for CLYC at 662 keV [20, 42, 43], but the energy resolution of this detector system was only 8.7% at 662 keV when measured with the FemtoDAQ. Since the energy spectra measured with the MCA had the same energy resolution (8.8% at 662 keV) the degradation cannot be attributed to the FemtoDAQ and is likely due to visible defects within the crystal. Measurements of the ^{60}Co source had energy resolutions of 8.4% and 7.0% at 1173 keV and 1332 keV, respectively.

The major difference between the two methods is measured count rate. The FemtoDAQ setup determined the energy of the pulse by integrating the entire recorded portion of the pulse which is relatively slow (< 200 cps) but important for determining the energy deposited for interactions with more than one pulse-shape. The MCA and GammaVision setup only has to determine the height of the pulse and assumes there is one pulse shape which results in a much faster count rate ($\sim$800 cps). If gamma

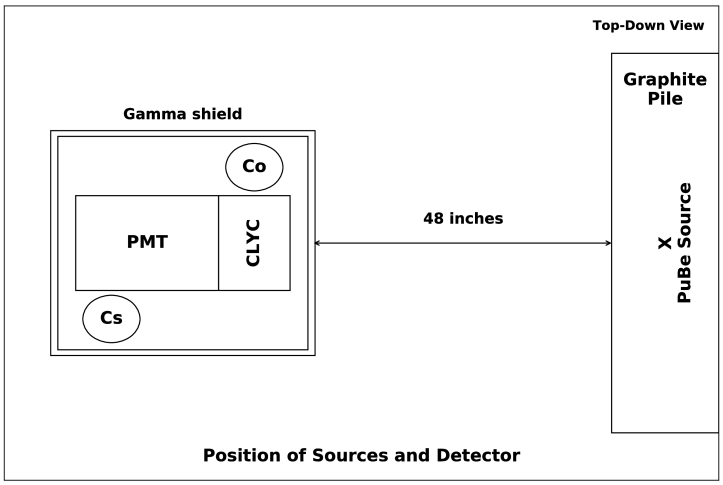

Figure 13. Experimental layout for irradiation from thermal neutrons generated by a PuBe source within a graphite pile.

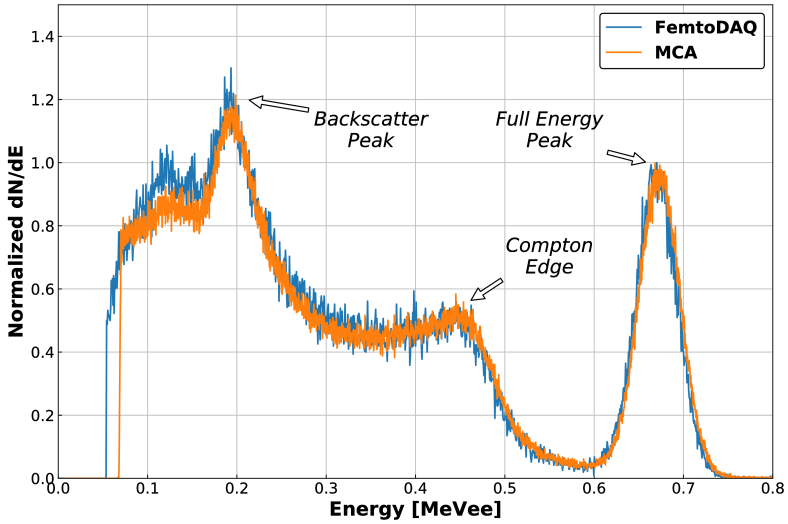

Figure 14. Calibrated gamma ray energy spectrum for ^{137}Cs as measured by CLYC using FemtoDAQ (R = 8.7% at 662 keV) and an MCA with GammaVision (R = 8.8% at 662 keV).

spectra were the only interest, FemtoDAQ has built in functionality to generate faster energy histograms which is not explored here.

The resultant energy spectrum measured during neutron irradiation is plotted in Fig. 15 and shows a strong peak at 3.1 MeVee (R = 4.3% at 3.1 MeVee) that is due to thermal neutrons interacting with ^{6}Li to create a ^{4}He and a triton. The q-value of this interaction is 4.78 MeV, which is shared between both resultant particles. Some quenching occurs within the detector such that the average energy measured for each thermal interaction is 3.1 MeVee. Due to the small size of the crystal the 1.1 and 1.3 MeV gamma peaks from ^{60}Co are diminished and the 4.4 MeV gamma ray from decay of excited ^{12}C nuclei following neutron production in the PuBe source is not detected at all.

Pulse shape discrimination

Two individual, normalized waveforms are shown for neutron and gamma events in Fig. 16 along with averaged waveforms for each type of event. As expected, the gamma waveforms decay much more rapidly than the neutron waveforms and this provides the basis for PSD. The windows for prompt and delayed measurements are also indicated to show how these regions are measured to determine PSD ratio.

Since the decay time of the excited states created by neutron interactions are longer lived than for gammas in CLYC, the PSD ratio is different and is used to verify that the peak at 3.1 MeVee is in fact due to thermal neutrons. By plotting the PSD ratio of each pulse against its energy measurement a two-dimensional histogram is produced that shows clearly differentiated gamma and neutron pulses (see Fig. 17). From this plot it is clear that the peak at 3.1 MeVee does not correspond to gamma ray interactions, but rather to thermal neutron interactions.

The ability to distinguish these pulses can be quantified by calculating a figure

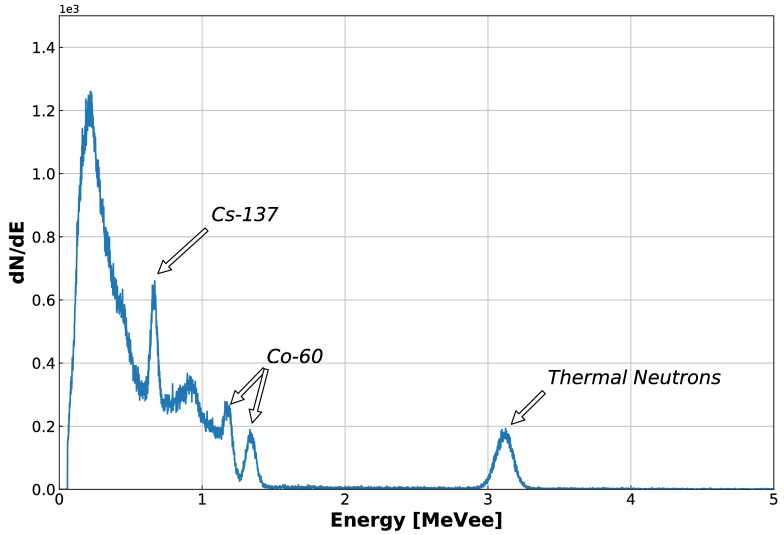

Figure 15. Energy spectra for three sources (^{137}Cs, ^{60}Co and thermal neutrons) as measured by CLYC. Peak at ∼3.1 MeVee is due to thermal neutron interaction ^{6}Li (n,t) ^{4}He (Q-value = 4.78 MeV).

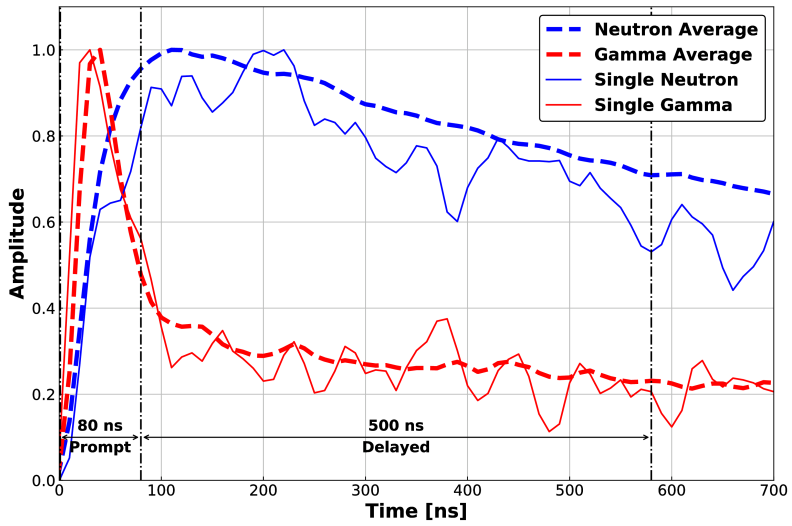

Figure 16. Individual and averaged waveforms for gamma and neutron events in CLYC. Also shown are the windows for prompt and delayed measurements used to calculate PSD ratios.

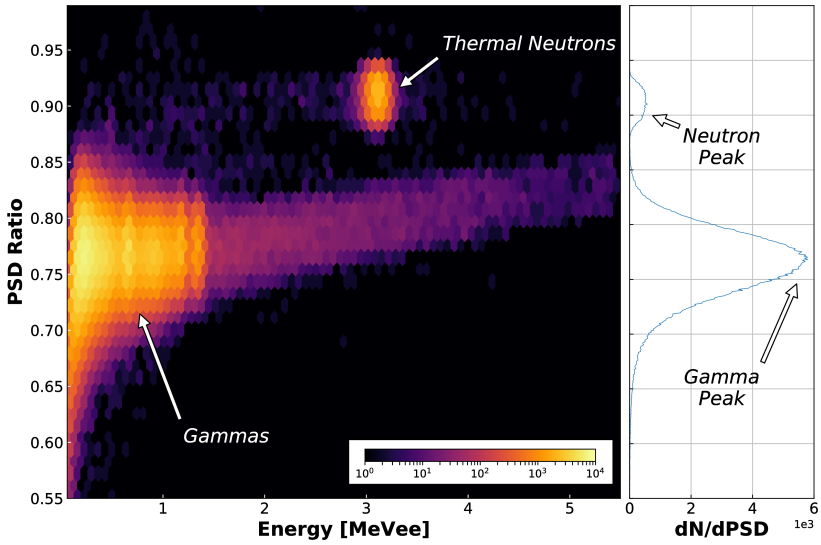

Figure 17. Two dimensional hexbin histogram of PSD ratios plotted against energy measured with a histogram of PSD ratios used to calculate a figure of merit for separating neutron and gamma pulses.

of merit (FOM) for separating neutron and gamma pulses. This is done by taking a histogram of the PSD ratios and identifying the peaks that corresponds to gammas (lower PSD ratios) and neutrons (higher PSD ratios). This histogram is shown in Fig. 17 and the FOM is calculated by,

$$FOM = \frac{\triangle\mu}{\Gamma_g + \Gamma_n}, \tag{10}$$

where $\triangle\mu$ is the difference between the centroids of the gamma and neutron peaks and Γ_g and Γ_n are the FWHM values for the gamma and neutron peaks, respectively [29]. In this way the FOM was found to be 1.42, though other research has indicated a FOM for CLYC could be as high as 4.83 when considering only the events within the energy range of the thermal neutron region (∼2.9-3.3 MeVee) [31]. There were not enough high energy gamma events in this analysis to calculate a FOM for this energy range but a previous study showed room temperature measurement to result

in a FOM of approximately 2.5 when the full energy range is considered [19].

3.5 Conclusion

Pulse-shape discrimination can be accomplished using CLYC and a low-cost digitizer, such as the FemtoDAQ, since the waveforms are 900 ns long on average. The longer pulse duration allows the 10 ns sampling rate of the FemtoDAQ to accurately digitize the differing shapes of the waveforms and calculate the PSD ratios. Additionally, the ability to write code in Python is a powerful tool allowing customized data collection and onboard analysis.

The comparison of gamma spectra measured using the FemtoDAQ to determine energy by integration of the waveforms to those spectra generated with an MCA and commercial software like GammaVision validates the method. It does highlight the decreased speed (75% slower for FemtoDAQ compared to an MCA) for energy collection, but this method also allows PSD ratios to be calculated and displayed in real-time.

The FemtoDAQ could be well suited to mobile radiation detection systems in either unmanned ground or aerial vehicles, or hand-held portable systems because of its small size and weight; both of which could be reduced by removing the metal box and using only the internal components. Furthermore, when used with a SiPM, instead of a PMT, the FemtoDAQ requires only 5 V direct current to digitize and process waveforms while also providing enough biasing voltage that an external power supply is not necessary for photomultiplication.

Future work will try to improve the FOM by examining different durations for prompt and delayed windows as well as exploring different techniques for assigning PSD ratios. Additionally, the FemtoDAQ will be used with a SiPM array to explore portable and mobile detector options.

IV. Comparison of SiPM and PMT Performance Using a $Cs_2LiYCl_6:Ce^{3+}$ (CLYC) Scintillator with Two Optical Windows

This study comparing CLYC-based detector measurements made using a SiPM to those made using a PMT (Research Objective II) was presented at the international *Nuclear Science Symposium* (NSS) in Sydney, Australia in November 2018 and generated a manuscript that was submitted to the *IEEE Transactions on Nuclear Science* on 7 January 2019. Comments from reviewers were received on 4 March 2019 and a revised manuscript was submitted on 1 April 2019. Two minor corrections were requested on 13 May 2019 and a revision was submitted on the same day. This chapter contains the complete, revised manuscript as submitted to the journal.

M. C. Recker, the primary author, prepared the manuscript and collaborated with E. J. Cazalas of the University of Utah (formerly of AFIT) on the experimentation and data analysis. J. W. McClory and J. E. Bevins, of AFIT, provided assistance as the author's research advisor and research committee member, respectively, and proofread the manuscript.

4.1 Abstract

Measurements of thermal neutrons and gamma rays using multiple CLYC crystals with a PMT and SiPM are compared. The first set of measurements used three single-sided crystals (two made from 95% enriched ^{6}Li and one made with 99% enriched ^{7}Li) mated with a PMT and SiPM to compare energy resolutions and figures-of-merit (FOM) for pulse-shape discrimination of gamma rays and neutrons. All crystals and photomultipliers were able to resolve full-energy photopeaks for ^{137}Cs and ^{60}Co and distinguish gamma ray interactions from neutron interactions (FOM > 1 in all cases) while operating in a thermal neutron environment. Measurements made with the

PMT had better energy resolution and switching to a SiPM degraded the energy resolution by an average of 34.0±0.7% (at 662 keV). The second set of measurements used a CLYC crystal with two optical windows to enable simultaneous measurements with a PMT and SiPM. Once again, both photomultipliers were able to distinguish gamma rays from neutrons, and the PMT had the best energy resolution. However, in this case the SiPM was not able to resolve the ^{137}Cs full energy photopeak and neither photomultiplier could resolve any photopeaks if ^{60}Co was used simultaneously. The degradation in energy resolution was due to the relative splitting of scintillation light intensity between each photomultiplier depending on the position of the interaction site within the crystal. Each pair of waveforms recorded from the PMT and SiPM, corresponding to a single interaction within the double-sided crystal, were combined to improve the energy resolution at 662 keV from 15.9±0.9% to 12.7±0.3% and the FOM from 1.850±0.004 to 2.117±0.003 when compared to the data from just the PMT.

4.2 Introduction

The inorganic scintillator $Cs_2LiYCL_6:Ce^{3+}$ (CLYC) is of interest due to its ability to detect gamma rays, thermal neutrons, and fast neutrons at the same time [12, 20]. CLYC has a cubic elpasolite structure with a density of 3.31 g/cm^3 [12] and a peak-emission wavelength of ∼373 nm [17, 18], which pairs well with many commercially available photomultiplier tubes (PMT) and silicon photomultipliers (SiPM). Scintillation is due to excitation of the Ce^{3+} centers and can be caused by prompt luminescence, trapped hole migration, self-trapped excitons and core-valence luminescence (CVL) [21, 22, 24]. Of these, CVL has the shortest decay time (1-4 ns) and is only possible with gamma rays [19, 23]. This ultrafast scintillation component allows pulse-shape analysis to discriminate between signals generated by gamma rays

and neutrons.

CLYC has been shown to work well with PMTs recording gamma ray energy spectra with energy resolutions as low as 4% (at 662 keV) for bare crystals and 5.0-6.0% for fully encapsulated crystals [9, 20] with figures of merit (FOM) for pulse-shape discrimination ranging from 1.8 at high temperature to 4.2 at low temperature [19, 44]. Unfortunately, PMTs have several disadvantages for use in mobile or portable systems including their relatively large size and high voltage requirement.

SiPMs, on the other hand, have sensitivity to similar wavelength ranges, a much smaller footprint, and require less biasing voltage (typically around 30-40 V), which makes them an obvious alternative to PMTs in smaller, more portable detector systems. However, studies exploring SiPM use with CLYC have been inconclusive. One study in 2012 showed a low FOM of 0.64 using a SiPM [30] and another study in 2013 was able to discriminate between neutrons and gamma rays using a SiPM but was unable to resolve the 662 keV photo-peak for a ^{137}Cs source [20]. Conversely, a study in 2015 using three different SiPMs coupled directly to the crystal as part of the encapsulation package reported gamma ray energy resolutions of 6.2%, 6.6% and 8.9% at 662 keV and FOMs always greater than 1 ranging up to $\sim$3.5 at low temperature (-20$^{\text{o}}$C) [29]. Another study in 2016 showed an energy resolution of 7.8% at 662 keV using a SiPM array at room temperature that degraded rapidly at higher and lower temperatures and a FOM that ranged from 1.2 at high temperatures to 3.0 at low temperatures with a value of 1.9 at room temperature [28].

While both of the recent studies showed SiPMs were able to resolve 662 keV photopeaks from ^{137}Cs and discriminate interactions of neutrons from gamma rays, neither of them made a direct comparison to PMTs [28, 29]. The goal of this research is to make that direct comparison and determine how the resolution changes when moving from a detector system that relies on a PMT for photomultiplication

to one that relies on a SiPM. This study uses multiple crystals of CLYC, including a unique fabrication that has two optical windows allowing for the attachment of both a PMT and a SiPM which permits direct comparison of the waveforms recorded from each photomultiplier for any individual scintillation event. The goal is to improve the comparison of PMT and SiPM response by ensuring data recorded from each photomultiplier correspond to the same interactions.

In this paper, we begin by describing the experiment, including the crystals and detector systems used for this research. We then analyze the data from the single-sided CLYC crystals to determine how the resolution varies when changing from a system that uses a PMT for photomultiplication to one that uses a SiPM. Next, we analyze data from our double-sided crystal and find that the waveforms provide information about the location of scintillation interactions within the crystal. Finally, we identify some topics we plan to explore more fully in future research.

4.3 Experiment

Three crystals were used for independent measurements with a SiPM and PMT. Two of these crystals, produced by Radiation Monitoring Devices (RMD), were 95% enriched in ^{6}Li. The remaining crystal, produced by CapeSym, was enriched in ^{7}Li. To better compare the performance of SiPMs to PMTs with CLYC, a custom crystal enriched in ^{6}Li (95%) was produced by CapeSym with two optical windows to allow concurrent measurement with a SiPM and a PMT. All of the crystals were approximately 1 inch right circular cylinders. Table 2 contains crystal identification information.

A 51 mm ETEL 9266KEB PMT was biased at -1000 V and the output signal was read directly from the PMT base without any pulse-shaping using a V1720 CAEN 12 bit digitizer reading at 250 MS/s. The SiPM was an 8×8 array of SensL 3 mm

Table 2. Identification and physical properties of CLYC crystals

Crystal ID	Li Enrichment	Crystal Grower
CS-1†	95% ^{6}Li	CapeSym
CS-2	99% ^{7}Li	CapeSym
RMD-1	95% ^{6}Li	Radiation Monitoring Devices
RMD-2	95% ^{6}Li	Radiation Monitoring Devices

†Double-sided crystal

× 3 mm ArrayJ sensors (spaced 0.2 mm apart) biased with 31.5 V and connected to a base and interface board created by AiT Instruments that has an output channel which sums all of the array signals together. This sum channel was read directly by the same CAEN digitizer.

Housings were made from polyactide (PLA) using a 3D printer to hold the crystals in place once coupled to the photomultipliers using optical grease. The housing for the standard crystals with one optical window (Fig. 18a) are cylinders of plastic that have a 1 inch diameter cavity to hold the crystal securely connected to the PMT with screws. The housing for the double-sided crystal (Fig. 18b) makes a similar connection to the PMT, but also has rectangular box that contains the SiPM. The SiPM rests on compressible foam that ensures the SiPM is pressed firmly against the crystal. This housing is also used to take measurements with the single-sided crystal with the SiPM by removing the PMT and sealing the open PMT attachment point.

The detectors were placed inside a bismuth box with 1/2 inch thick walls to reduce the number of background gamma rays interacting with the crystals. Known gamma ray sources (^{137}Cs and ^{60}Co) were placed inside the box, approximately five inches from the detector, to provide three known photo-peaks for energy calibration and energy resolution measurements. A predominantly thermal source of neutrons ($\sim 10^3 \mathrm{n/cm^2 s}$) was generated by a PuBe source within a graphite pile at the Air Force Institute of Technology. These measurements were taken at an ambient temperature

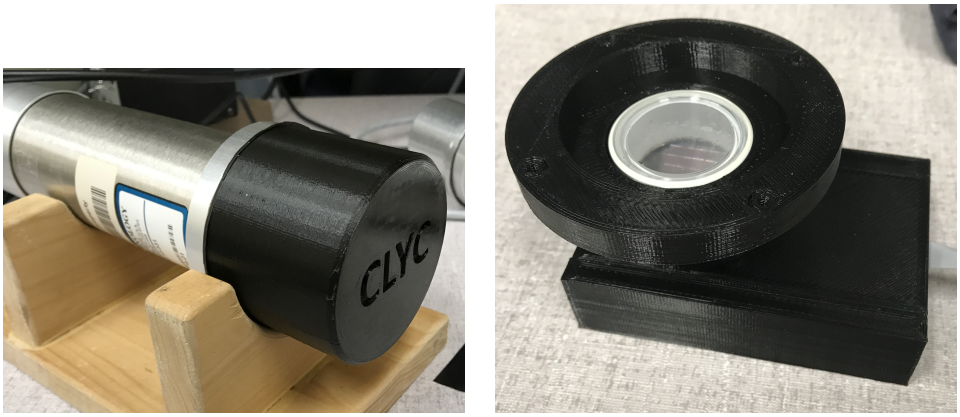

(a) (b)

Figure 18. 3D printed crystal housings for (a) coupling standard CLYC crystals to the PMT and (b) coupling the double-sided CLYC crystal to a PMT and SiPM concurrently. The PMT attaches to the top circular portion of the housing for the double-sided crystal (b) and the SiPM is completely contained in the black rectangular portion. The crystal sits slightly above the plastic surface to allow good coupling with the PMT. The SiPM rests on compressible foam which holds the components together, but also provides enough vertical movement to ensure the components are not damaged when the PMT is bolted tightly to the housing.

of $\sim 30^{\text{o}}$C.

The total energy deposited by each interaction was determined by integrating the first 6.2 μs of each waveform. Pulse-shape discrimination (PSD) was accomplished after all of the waveforms were captured by considering a prompt region (the first 80 ns of the waveform) and a delayed region (500 ns immediately following the prompt region), which was found to provide the best FOM in previous experiments using the same PMT [31, 45]. A PSD ratio was determined using

$$PSD\,ratio = \frac{D}{P + D}, \tag{11}$$

where P is the integral of the waveform in the prompt region and D is the integral in the delayed region. A histogram of the PSD ratios was used to determine the figure

of merit (FOM) for the separation of gamma rays and neutrons using

$$FOM = \frac{\triangle\mu}{\Gamma_g + \Gamma_n}, \tag{12}$$

where $\triangle\mu$ is the difference between the centroids of the gamma ray and neutron peaks and Γ_g and Γ_n are the FWHM values for the gamma ray and neutron peaks, respectively [29].

4.4 Results and Discussion

Single-sided crystals

Energy spectra for each crystal recorded using both the PMT and SiPM are shown in Fig. 19. In all cases, the measurements made with the PMT had the best resolution, but the measurements with the SiPM were able to adequately resolve all of the photopeaks. The low energy regions differ because the SiPM threshold was set at a higher level, relative to peak waveform amplitude. This was done to reduce noise since the SiPM waveforms had a much smaller amplitude than the PMT waveforms.

The FOM for each crystal and energy resolution for each photopeak are listed in Table 3. Also listed are the ratios of PMT resolution to SiPM resolution as an indication of how the resolution will change when moving from a PMT-based measurement to a SiPM-based measurement. The ratios appear to vary by energy with the change in resolution being more significant for low energy photopeaks. The 1172 keV photopeak has the widest range of ratios (0.74 to 0.89), due to the low number of counts and difficulty determining the precise low-energy limit of the photopeak. All measurements of the energy resolution for the 662 keV photopeak are worse than the previously referenced 4% value. This is likely due to encapsulation of the crystal and defects within the crystal, especially for RMD-1 which has a large, visible defect

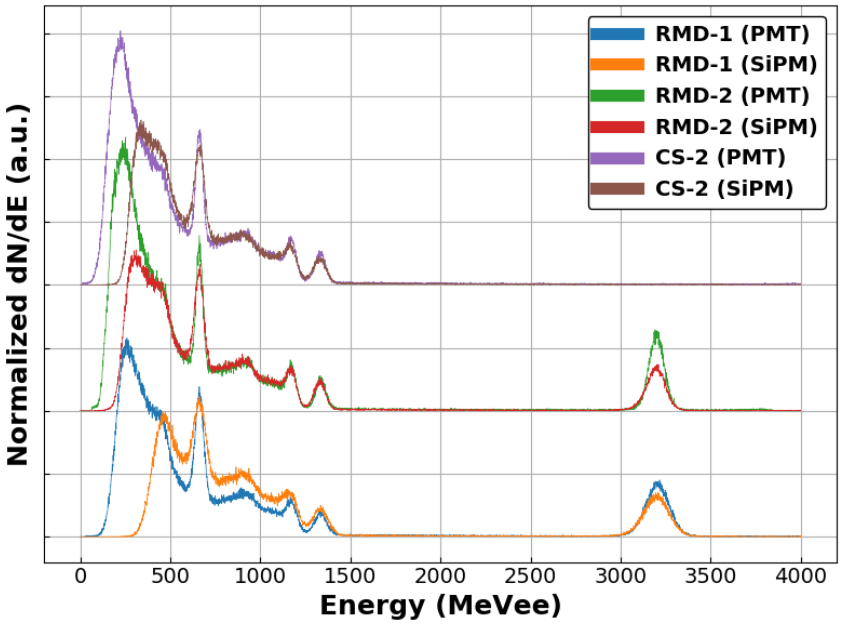

Figure 19. Energy spectra for three CLYC crystals exposed to ^{137}Cs, ^{60}Co, and thermal neutrons. Each crystal was used for two measurements, one with a PMT and one with a SiPM. In all cases, the PMT had better resolution than the SiPM, but both photomultipliers were able to fully resolve all peaks. The crystal identified as CS-2 was made using 99% enriched ^{7}Li, the other two were made with 95% enriched ^{6}Li.

near the optical window.

From these measurements one would always expect the energy resolution to degrade when changing from a PMT to a SiPM. The energy resolution was degraded by 34.0±0.7% at 662 keV; 27±7% at 1172 keV; and 13±1% at 1332 keV. There was also a variation in energy resolution between each of the crystals for each photomultiplier type, on average there was a 17±3% degradation in resolution when compared to the resolution of the RMD-2 crystal. However, in all cases the energy resolution was always best when the spectrum was recorded with a PMT.

Two dimensional histograms of PSD ratio and energy (see Fig. 20) show clear separation of gamma rays and neutrons in all crystals paired with either PMT or SiPM. In the plot of data collected using the RMD-2 crystal mated with a PMT (Fig. 20a) all of the gamma ray sources are identifiable and clearly separated from

Table 3. Comparison of energy resolutions for PMT and SiPM measurements for each Single-Sided CLYC crystal

Crystal	PM	FOM[a,b]	Res. @ 662 keV[b]	Ratio[c]	Res. @ 1172 keV[b]	Ratio[c]	Res. @ 1332 keV[b]	Ratio[c]
RMD-1	PMT	2.352±0.003	8.3±0.1%	0.75±0.02	5.6±0.3%	0.74±0.07	5.4±0.2%	0.88±0.04
	SiPM	2.466±0.005	11.2±0.3%		7.6±0.6%		6.2±0.2%	
RMD-2	PMT	2.490±0.004	6.5±0.1%	0.75±0.02	4.7±0.2%	0.89±0.05	4.7±0.1%	0.90±0.03
	SiPM	2.289±0.005	8.6±0.2%		5.3±0.2%		5.3±0.1%	
CS-2	PMT	–	6.9±0.1%	0.74±0.02	4.7±0.2%	0.76±0.05	5.0±0.1%	0.87±0.03
	SiPM	–	9.3±0.2%		6.3±0.3%		5.8±0.2%	

[a]FOM calculated for all interactions with energy greater than 500 keVee
[b]Reported uncertainty comes from Gaussian fits and represents the 95% confidence interval
[c]Reported uncertainty comes from standard error

the thermal neutrons interacting with ^{6}Li based on the data point clusters in the 2D histogram. A small cluster is just discernible at ˜0.49 MeVee that is due to thermal neutrons in a ^{35}Cl(n,p)^{35}S interaction within the crystal. The energy of this cluster is lower than the Q-value for this interaction (615 keV), but previous studies have shown a quenching factor for the ^{35}Cl(n,p)^{35}S interaction in the range of 0.85-0.90 [4, 46].

The plot of data collected using the RMD-2 crystal mated with a SiPM (Fig. 20b) also shows clear separation between the thermal neutrons interacting with ^{6}Li and the known gamma ray sources, all of which are easily identifiable in this view. However, there does not appear to be a clearly defined cluster corresponding to thermal neutrons interacting with ^{35}Cl as there was with the PMT measurement. The FOMs shown in Table 3 and in Figs. 20a and 20b were calculated using all interactions with energy greater than 500 keVee. The FOM is decreased when using the SiPM in the case of RMD-2, down to 2.289±0.005 from 2.490±0.004 when measured with the PMT. However, this is not always the case. With RMD-1 the separation was actually improved from 2.352±0.003 with the PMT to 2.466±0.005 with the SiPM. All combinations of CLYC crystal and PMT or SiPM resulted in FOMs above one, indicating adequate ability to distinguish between the gamma ray and neutron events.

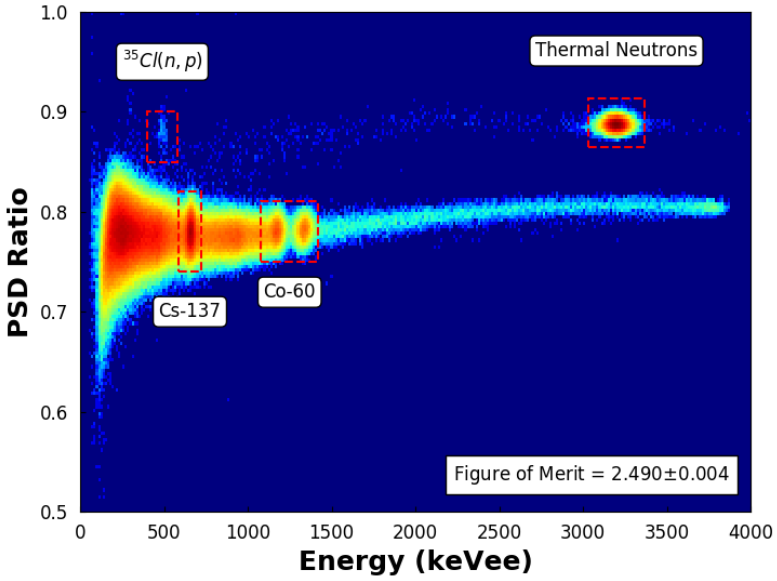

(a)

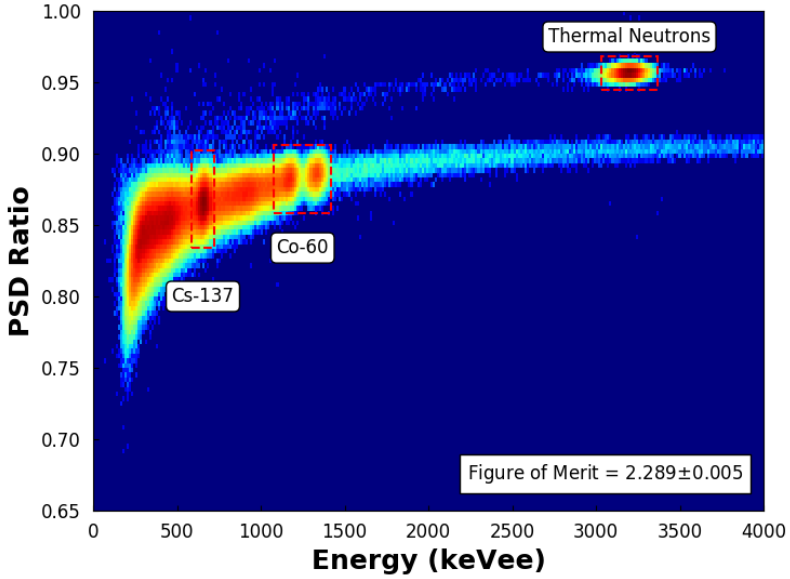

(b)

Figure 20. Two-dimensional histograms of PSD ratio and energy with intensity scaled logarithmically for (a) PMT and (b) SiPM measurements with the RMD-2 crystal. PMT shows better resolution, but SiPM is also able to clearly resolve the photopeaks of known gamma ray sources and the strong thermal neutron peak. A small cluster is visible in the PMT plot due to the ^{35}Cl(n,p)^{35}S interaction that is not defined in the SiPM measurement. All known sources are labeled in the plots and the FOM is reported for all interactions with energy greater than 500 keVee.

This also includes the double-sided crystal which will be discussed in the following section. The only exception was the CS-2 crystal which was enriched in ^{7}Li and therefore not very sensitive to thermal neutrons. While it was possible to identify small clusters of neutrons in the PSD plots for CS-2, the number of neutrons detected was very small and a FOM could not be calculated.

The plots of the PSD ratio were used to set energy and PSD ratio boundaries for examining the waveforms corresponding to thermal neutrons and ^{137}Cs gamma rays in each crystal and for each photomultiplier. The ranges for PSD ratio and energy were chosen to tightly bound each cluster in PSD space and roughly correspond to the red boxes indicated in Fig. 20 for ^{137}Cs and thermal neutrons. These waveform groups were averaged, scaled to their peak amplitudes and plotted in Fig. 21. The first two subplots show (a) the gamma ray and (b) the neutron waveforms for each crystal when measured by a PMT. The risetime for the gamma ray waveforms is on the order of tens of nanoseconds (24±4 ns for RMD-2), while the risetime for thermal neutron waveforms is about an order of magnitude longer (116±4 ns for RMD-2). The gamma ray waveforms fall off rapidly, reaching 20% of their peak value by $1\,\mu s$, while the thermal neutron waveforms have only decayed to $40-60\%$ by $1\,\mu s$. While the probabilities of thermal neutron interactions in CLYC with ^{7}Li enrichment are greatly reduced there were still a few interactions that could be identified and averaged for the CS-2 crystal. The small number of interactions is why the CS-2 average waveform has more noise than the other two crystals.

The last two subplots show the averaged waveforms for (c) gamma ray and (d) neutron interactions as recorded by the SiPM. As with the PMT, the gamma ray waveforms rise much faster than the thermal neutron waveforms and then initially decay much more rapidly as well. However, with the SiPM measurements the gamma ray waveforms have a secondary peak that begins to appear around $100\,ns$ with a

very slow risetime and decay. Besserie et al. previously showed that the gamma ray waveforms consist of a CVL component on top of a more slowly decaying component due to other scintillation processes [23]. We believe the initial peak in our waveforms is due to the fast CVL scintillation process, while the second peak corresponds to the longer scintillation processes (prompt luminescence, trapped hole migration, self-trapped excitons) in CLYC.

The decay times for the waveforms measured from the SiPM are longer for all crystals, and this enables us to resolve the CVL process from the other scintillation processes. The effect is strongest in the crystals with the most defects (RMD-1 and CS-2), because the slow process scintillation photons can re-excite electrons in the crystal and more defects results in more scattering and opportunities for excitation. The defects in RMD-1 and CS-2 are sufficient to create a small shift can also be seen in the PMT waveforms (Fig. 21a).

Between the three crystals, RMD-1 always decays fastest for gamma ray interactions and slowest for neutron interactions, regardless of photomultiplier used, while RMD-2 is the slowest for gamma ray interactions and fastest for neutron interactions. The average waveforms measured from the CS-2 crystal always fall between the waveforms measured with the other two crystals.

Double-sided crystal

When the thermal neutron and gamma ray sources were measured with the double-sided crystal, the energy resolution at 662 keV was quite poor. The PMT had an energy resolution of 14.7% and the SiPM was unable to resolve the ^{137}Cs photopeak. When ^{60}Co was included, none of the photopeaks were resolved regardless of which photomultiplier was used. The result of pulse-shape analysis for the double-sided crystal is shown in Fig. 22. These measurements are uncalibrated because the de-

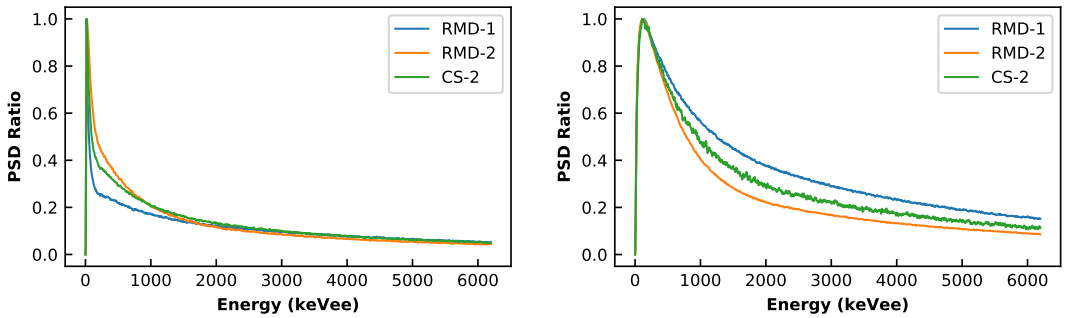

(a) PMT Gamma Ray Waveforms

(b) PMT Neutron Waveforms

(c) SiPM Gamma Ray Waveforms

(d) SiPM Neutron Waveforms

Figure 21. Averaged waveforms, normalized to their peak amplitudes, for ^{137}Cs gamma ray interactions (a and c) and thermal neutron interaction with ^{6}Li (b and d) in each crystal measured using the PMT (a and b) and the SiPM (c and d). When measured using the SiPM, the waveforms were longer-lived and the gamma ray events had a secondary peak. The fast component in these waveforms corresponds to photons generated by the CVL process while the secondary peak corresponds to the slower scintillation processes.

graded resolution made good energy calibration difficult. The lower bound for FOM calculations (channel 300) was chosen because it was above the threshold for each detector and below the full energy photopeak for ^{137}Cs. Both photomultipliers were able to discriminate between gamma rays and neutrons, but the FOM was lower, 1.850±0.004 for the PMT and 1.601±0.005 for the SiPM.

The change in resolution is most likely primarily due to the splitting of scintillation photons between the PMT and SiPM at the ends of the crystal with the photomultiplier closest to the interaction site receiving more photons. In a single-sided crystal the photons reflect within the crystal until they are absorbed by the case or exit

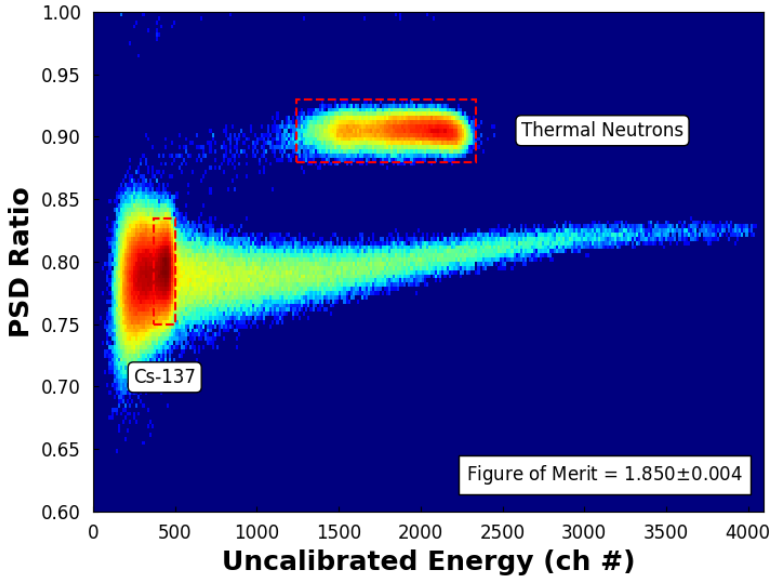

(a)

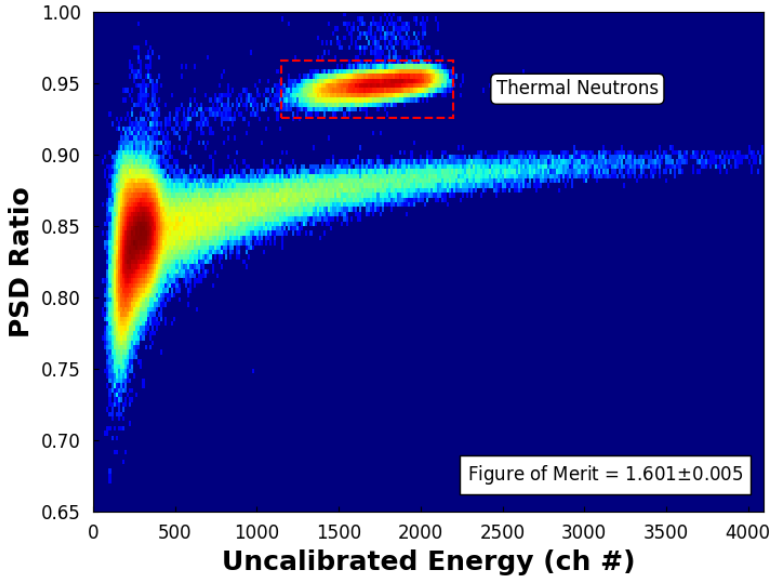

(b)

Figure 22. Two-dimensional histograms of PSD ratio and uncalibrated energy with intensity scaled logarithmically for (a) PMT and (b) SiPM measurements with the double-sided CS-1 crystal. The lower bound for FOM calculations (channel 300) was chosen because it was above the threshold for each detector and below the full energy photopeak for ^{137}Cs. Both photomultipliers provide measurements with acceptable FOMs (1.850±0.004 for PMT and 1.601±0.005 for SiPM), but only the PMT is able to resolve the ^{137}Cs full energy peak. ^{60}Co could not be used with ^{137}Cs in this measurement because the decreased resolution meant none of the photopeaks were resolvable in either photomultiplier. All known sources are labeled in the plots.

through the optical window thereby allowing for a greater fraction of the photons to be collected for a given interaction. Since the fraction of photons lost to absorption will be mostly constant, the number of photons exiting through the optical window will be approximately the same for repeated events at a given energy, which will result in better resolution.

In the case of a double-sided crystal, however, photons have two paths to leave the crystal. If the site of interaction occurs closer to one end of the crystal, then the number of photons exiting the crystal through that side will be larger than those exiting the other side. This is because the solid angle that allows escape without first reflecting is much larger for the nearer optical window. Since the surface of the case is not perfectly smooth, some of the photons initially headed towards the further window may reflect back towards the nearer window, thus increasing the proportion of photons measured on the side nearest the interaction site.

This effect is displayed in Fig. 23, which shows the range of waveforms for the thermal neutron region. In this plot the heavy blue line indicates the average of all thermal neutron waveforms measured by the PMT while the orange line shows the same for the SiPM. Each area is bounded by a minimum and maximum waveform that is calculated by averaging waveforms on the low energy and high energy ends of the thermal neutron regions identified in Fig. 22a and b. The wide range of energy measurements for events with a single energy value results in degradation of the energy resolution. Similar results (not shown) were found when considering the waveforms in the ^{137}Cs gamma ray region.

When using the CAEN digitizer with multiple input channels, a trigger on one channel will record the waveforms on all active channels which synchronizes the waveforms in time. The raw data is then parsed to ensure that both channels registered a peak without pileup. This allows plotting pairs of waveforms generated by each

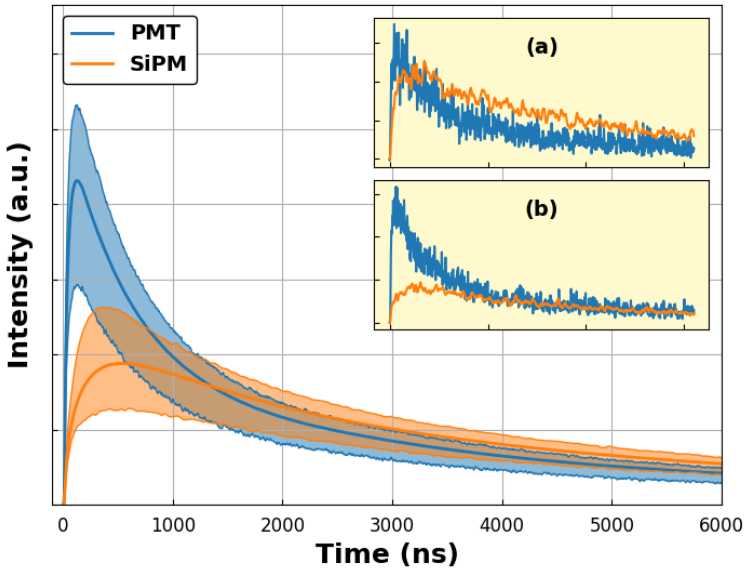

Figure 23. Range of waveforms for simultaneous PMT and SiPM measurements of thermal neutron interactions. The dark line indicates the average waveform and the shaded areas indicate the range of possible measurements. Inset (a) shows a pair of individual waveforms when the PMT integral is lowest and SiPM is highest while inset (b) shows the opposite. This variation in energy measured indicates whether the interaction site was closer to the PMT or SiPM. Gamma ray interactions follow the same trend.

photomultiplier simultaneously from a single interaction within the crystal.

To verify the positional dependence, two waveform pairs are shown as insets to Fig. 23 that demonstrate the inverse relationship between the waveform intensity in the PMT and the SiPM measurement. Inset (a) shows a pair of waveforms where the PMT waveform was selected from the low end of the thermal neutron energy peak and the corresponding SiPM measurement is near its highest value for a thermal neutron interaction. Inset (b) shows the opposite where the PMT waveform is selected from the high end of the thermal neutron region and the corresponding SiPM measurement is near its lowest value for a thermal neutron interaction. The data indicates that high energy PMT measurements correspond to low energy SiPM measurements, and vice versa, therefore a comparison of the energy measurements reveals the relative

position of the interaction site within the crystal by indicating which photomultiplier was closest.

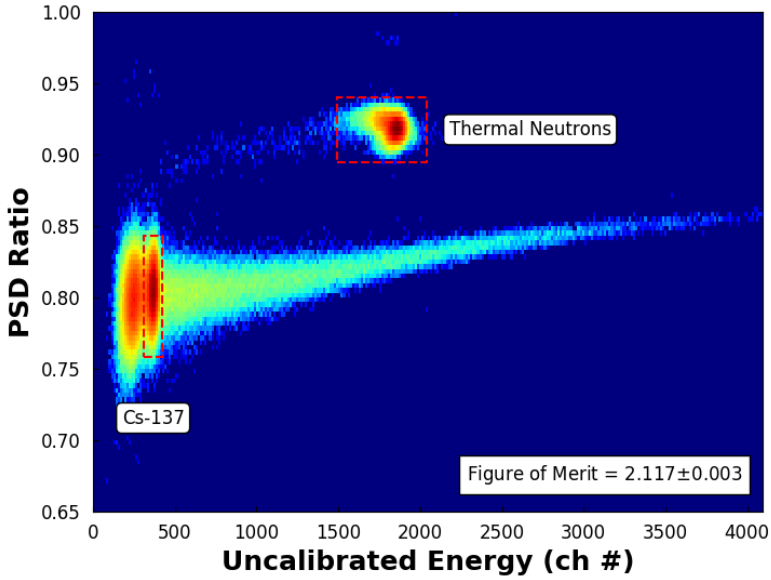

Figure 24. Two-dimensional histograms of PSD ratio and uncalibrated energy with intensity scaled logarithmically for combined data from PMT and SiPM measurements with the double-sided CS-1 crystal. The lower bound for FOM calculations (channel 300) was chosen because it was above the threshold for each detector and below the full energy photopeak for ^{137}Cs. Combining the waveforms also improved the FOM to 2.117±0.003.

To improve the measurements made with the double-sided crystal each of the waveform pairs were combined and averaged without any weighting consideration between PMT and SiPM. The resultant waveforms were then analyzed and the resolution of the ^{137}Cs photopeak improved to 12.7±0.3% compared to 15.9±0.9% when only considering the PMT measurements. The two-dimensional histogram of PSD ratio against uncalibrated energy is shown in Fig. 24. In this view the width of the thermal neutron region has been greatly reduced (5.0% energy resolution) and the ^{137}Cs region is much more defined. The FOM is improved from 1.850±0.004 in the PMT data and 1.601±0.005 in the SiPM data to 2.117±0.003 using the combined data. While the energy resolution is improved it is still not nearly as high as in the

single-sided crystal. However, the FOM for pulse-shape discrimination is comparable to that obtained with single-sided crystals.

4.5 Conclusion

The data presented in this work show that PMTs and SiPMs are both able to adequately discriminate between neutron and gamma ray interactions within CLYC, and have similar FOMs for pulse-shape discrimination. Additionally, the data indicate a degradation in energy resolution with CLYC of approximately 34.0±0.7% (at 662 keV) when moving from PMT to SiPM-based measurement. This may be an acceptable loss considering the inherent high quality energy resolution of measurements with CLYC and the benefits of using a smaller photomultiplier that does not require high voltage biasing. Despite the degradation in energy resolution, all of the single-sided crystals were able to resolve the full-energy photopeaks for ^{137}Cs, ^{60}Co, and thermal neutrons during simultaneous irradiation.

The double-sided crystal initially showed poor energy resolution and acceptable FOM for pulse-shape discrimination, but the combined data was able to modestly improve the energy resolution and greatly improve the FOM. Additionally, the potential ability to determine the interaction position within the crystal may eventually provide a detector benefit that outweighs the loss in energy resolution.

Future work will explore using two identical SiPMs on the double-sided crystal. This should allow more accurate combination of the waveforms and may result in improved energy resolution while preserving the ability to determine the position of the interaction within the crystal.

V. Determining Direction of a Neutron Source Using a $Cs_2LiYCl_6:Ce^{3+}$ (CLYC) Scintillator with Two Optical Windows

This study demonstrates the possibility of using a CLYC crystal with two optical windows to determine the direction of a thermal neutron source (Research Objective III). The results of this study may lead to a new use for CLYC in the areas of nonproliferation and lost source recovery. This work warrants publication and future investigation and further work developing this concept would be well suited for a Master's thesis project. The author intends to submit this chapter as a manuscript for publication, but no journal has been selected.

5.1 Introduction

The results presented in the previous chapter (Ch. IV) suggested that measurements made using the double sided CLYC crystal had information about the location of the interaction sites for neutrons within the crystal. This was seen as a broad neutron peak for measurements taken with each photomultiplier (Fig. 22). It was argued that when the interaction site was closest to a photomultiplier, that photomultiplier received a larger fraction of the total scintillation photons and when it was further from the same photomultiplier, it received fewer scintillation photons. This meant that neutrons of a single energy (thermal in this case) produced waveforms with a wide range of amplitudes in the two channels defined by the two photomultipliers.

When the waveforms from each photomultiplier were combined, the effect mostly vanished and the resolution of the neutron peak was greatly improved. Only a small improvement in gamma ray energy resolution was observed. The different behavior between gamma rays and thermal neutrons was likely due to different penetration depths for each, with gamma rays being much more penetrating.

That study concluded that it might be possible to determine the direction of a neutron source using a similar double sided CLYC crystal and rotating it to find when each photomultiplier signal was maximized. The theory was that, if the thermal neutrons did not penetrate too deeply within the crystal, the photomultiplier nearest the neutron source would have the largest amplitude response and indicate the direction of the source.

This study begins by exploring the feasibility of determining the direction of a neutron source using a CLYC crystal with two optical windows by creating a simple Monte Carlo code to determine the penetration depth of thermal neutrons incident on the crystal surface. In order for the determination of source direction to be possible, the majority of thermal neutron interactions must not penetrate further than halfway through the crystal. Shallower penetration depth will result in better direction discrimination because the difference in maximum and minimum waveform amplitudes will be greater.

The second phase of the study will be to build a detector using a double sided CLYC crystal with a SiPM on each optical interface and then analyze how the signals change as the detector is rotated in the presence of a neutron source. If the penetration depth is shallow enough, then the amplitude of the waveforms and the position of the neutron peak should change as a function of this rotation.

5.2 2D Monte Carlo Model

There are four main interactions for a neutron within CLYC: it can scatter elastically (1) or inelastically (2), it can interact with ^{35}Cl to release a proton (3), or it can be absorbed by ^{6}Li to create an α and triton (4). The two scattering events do not cause scintillation, but they do lower the energy of the neutron. The ^{35}Cl (n,p) reaction releases a proton with an energy that is linearly dependent on the energy of the

incident neutron and might be the most useful interaction for generating a neutron spectrum [4, 38]. The ^{6}Li(n,t)α reaction releases an α and triton that are dependent on the kinetic energy of the incident neutron but produce a continuum instead of a peak for fast neutrons and thus could be used for counting thermal neutrons, but not for determining a neutron spectrum [4].

To explore the behavior of thermal neutrons in CLYC, a simple 2D Monte Carlo code was written. This code assumes that everything outside of the CLYC crystal is a vacuum and thus there is no attenuation of the neutrons from the source to the detector. In fact, all neutrons are created at the center of the left boundary of the crystal. Since elastic scattering is isotropic, one can avoid most of the complicated rotation matrices and allow the neutrons to scatter in random directions [1].

The following interactions were modeled: elastic scattering with ^{35}Cl, ^{35}Cl(n,p)^{35}S, and ^{6}Li(n,t)α. Inelastic scattering was not modeled since it is only possible at higher neutron energies. Each neutron is created at the boundary and allowed to travel in a random direction for some distance according to the total cross-section for the three interactions considered. If the next interaction is due to elastic scattering, then the energy of the neutron is decreased and a new random direction is chosen. If the interaction is due to capture in ^{6}Li or ^{35}Cl, then the neutron is absorbed and no longer tracked. If the neutron leaves the detector at any point, it is assumed that scattering back into the detector is not possible and the particle is no longer tracked.

The 2D Monte Carlo code modeled 100,000 thermal neutrons (0.025 eV) and the paths of the thermal neutrons ultimately absorbed within the crystal are shown in Fig. 25. From this model, it is clear that thermal neutrons incident on the crystal are unlikely to scatter before they are captured. Importantly, this model shows that less than 1% of the thermal neutrons incident on the center of the crystal boundary will scatter without absorption and the remainder will be absorbed near the interface

with fewer than 0.02% penetrating more than 1.5 cm into the crystal before being absorbed.

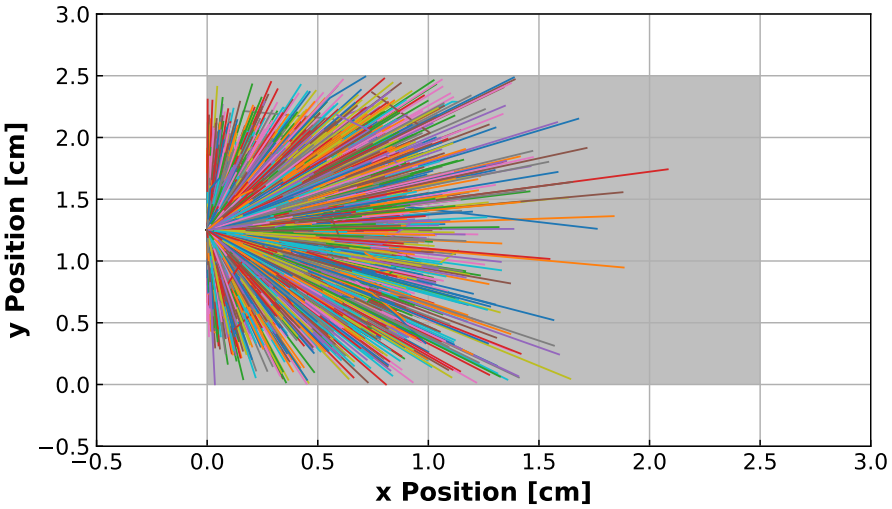

Figure 25. Thermal neutron tracks within CLYC showing the paths taken by thermal neutrons within the crystal. It demonstrates that thermal neutrons are captured very quickly within the material.

This simplistic model demonstrates that even a 2.5 cm crystal is sufficiently large to restrict neutron interaction to the first half of the crystal. If this crystal has two optical windows, each coupled to a SiPM, then whichever optical window is positioned nearest to the thermal neutron source should have the stronger response. This is because the neutron interaction sites in the crystal will be nearest to that photomultiplier and it will collect the majority of the scintillation photons as described in Ch. IV.

5.3 Experiment

For this experiment, a CLYC crystal with two optical windows was grown with 95% enriched ^{6}Li and packaged by CapeSym. This is the same crystal used for the experiment in Ch. IV. A new housing was 3D printed with PLA that allowed two

SiPMs to be coupled to the crystal, one for each optical window. The SiPMs were the same type, one of which was used in the previously referenced experiment. They were an 8×8 array of SensL 3 mm × 3 mm ArrayJ sensors, both biased at 31.5 V and connected to interface boards developed by AiT Instruments. Each SiPM array was summed together on the interface board to create a single channel of data for each optical window.

These channels were recorded directly, without any shaping, by a V1720 CAEN 12 bit digitizer reading at 250 MS/s. The gain and offset of each channel were adjusted such that the baseline and peak amplitude of each waveform were approximately the same for each channel when the detector was placed in a neutral position. In this position, the central axis of the crystal was horizontal and orthogonal to the direction of the neutron source, which resulted in each SiPM being equidistant from the average interaction site within the crystal. Thermal neutrons were generated by a PuBe source placed inside a graphite pile, and the detector was placed approximately 10 meters away.

The experiment began by aligning the central axis of the crystal directly in the direction of the neutron source, with one SiPM (SiPM 0) at its nearest position, and the other (SiPM 1) at its furthest position. Measurements were made for 10 minutes, and the detector was rotated 45° and measured again. This was repeated until the detector had been rotated 180° and the final measurement was made when the other SiPM was nearest the neutron source.

5.4 Results

The initial approach to determine which SiPM was closest to the source was to examine the waveforms and determine when the peak amplitude or waveform integrals were at a maximum. However, in a 10 minute collection there were too few wave-

forms (at the measurement distance) for a smooth average. While the difference in waveforms between nearest and furthest position for each SiPM were distinguishable, the other rotation positions were not.

The best method for determining which SiPM was closest was to find the centroid of the neutron peak. This was accomplished by first considering only the neutron region (waveform integral values 300,000 to 600,000 and PSD ratios 0.93 to 1.00) for each position measurement. Then a Gaussian was fit to a histogram of the integral values for these selected interactions. The centroid of this Gaussian indicated whether each SiPM was at its nearest or furthest position from the source.

This works because, in a double sided crystal, the integral of the waveforms in one photomultiplier increases as the interaction site moves closer to the photomultiplier since it receives a larger fraction of the total scintillation photons [47]. This increase in the waveform integral will change the position of the neutron peak on the uncalibrated energy axis.

The result of the first measurement is shown in Fig. 26 with error bars indicating uncertainty (1σ) in the centroid position from the Gaussian fit. From this plot, very little change can be seen in neutron peak position as a function of rotation with most of the error bars for neutron peak position at each rotation overlapping. This is because the crystal was taken from a cool environment ($\sim$24°C) and moved to a warmer environment ($\sim$33°C) without sufficient time to reach thermal equilibrium. The change in thermal energy affects the neutron waveforms (see Ch. VII), and the change in neutron peak position is minimized. Since increased thermal energy tends to increase the amplitude of the waveforms [19, 29], one might expect the neutron peak position to change more rapidly for SiPM 0 as it moves from its furthest position to its nearest position while the crystal is warming up, but this was not observed.

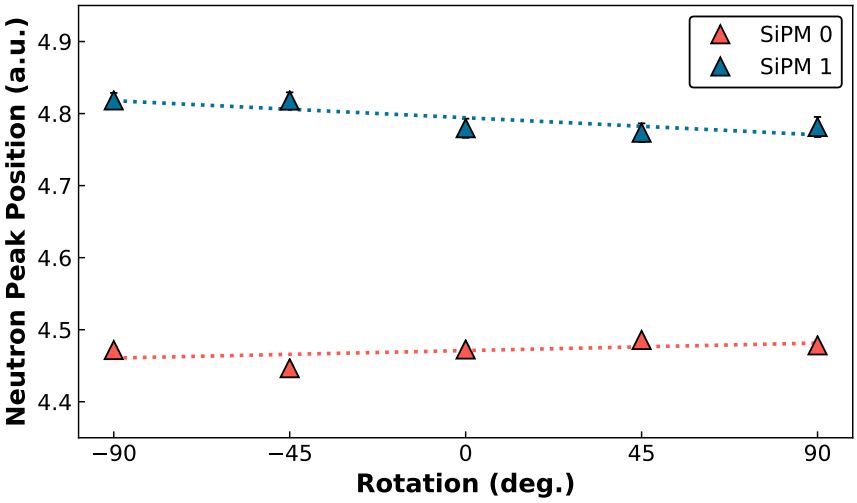

Figure 26. Changes in the neutron peak position as a function of detector rotation. For this measurement, the crystal was moved from a cool environment (∼24°C) to a warmer environment (∼33°C) and not provided time to reach thermal equilibrium. The dotted lines indicate the best linear fit for SiPM 0 ($R^2 = 0.31$) and SiPM 1 ($R^2 = 0.72$).

The crystal was left in the warm environment overnight for the second measurement to allow it to reach thermal equilibrium. The result of the subsequent measurement is shown in Fig. 27. In this plot, the change in neutron peak position is more consistent and significant. The linear fit for each SiPM is also improved with R^2 values of 0.86 and 0.92 for SiPM 0 and SiPM 1, respectively. Many of the individual measurements have overlapping error bars, however, indicating that the precise direction would be difficult to determine. This is because thermal neutrons interacting with the crystal are not exclusively taking direct paths from the graphite pile. Many of these neutrons are scattering before they reach the detector and can enter the crystal from any direction. The majority of the neutrons are coming directly from the source, because the effect of rotating the detector can be seen clearly in the data, but the scattered neutrons interacting at different locations within the crystal diminishes the effect.

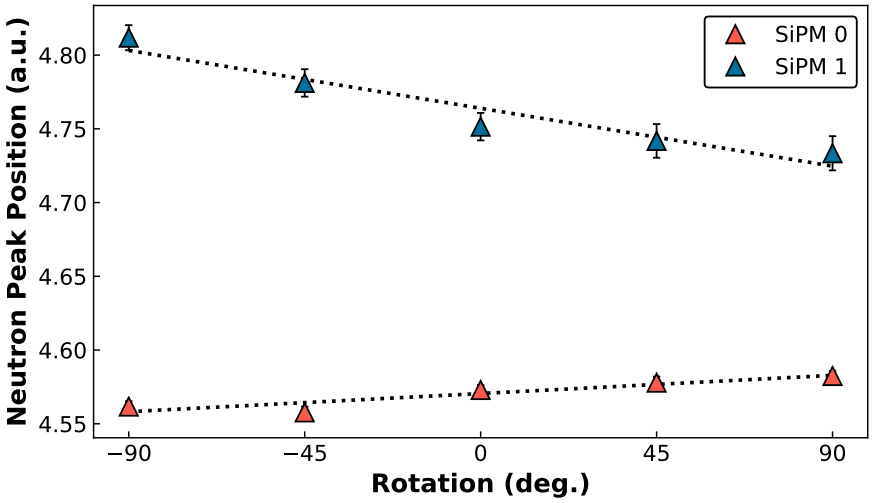

Figure 27. Changes in the neutron peak position as a function of detector rotation. For this measurement, the crystal was kept in the warm environment (∼33°C) overnight and received sufficient time to reach thermal equilibrium. The dotted lines indicate the best linear fit for SiPM 0 ($R^2 = 0.86$) and SiPM 1 ($R^2 = 0.92$).

Additional shielding was added to reduce the number of scattered neutrons reaching the detector for the final measurement. Five sides of the detector were surrounded with blocks of borated polyethylene and thin sheets of cadmium (see Fig. 28). The opening of this box was pointed at the neutron source and the detector was rotated inside the stationary box. The result of this measurement is shown in Fig. 29. This measurement had the most significant changes in neutron peak position, and only two data points had overlapping error bars (SiPM 0 at 45° and 90°).

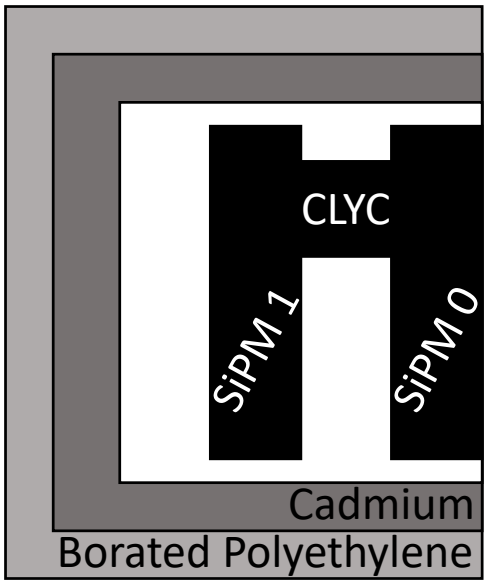

Figure 28. Top down cross section of the additional shielding added for the final measurement (not to scale). Borated polyethylene and cadmium were added to reduce the number of indirect neutrons scattering into the detector.

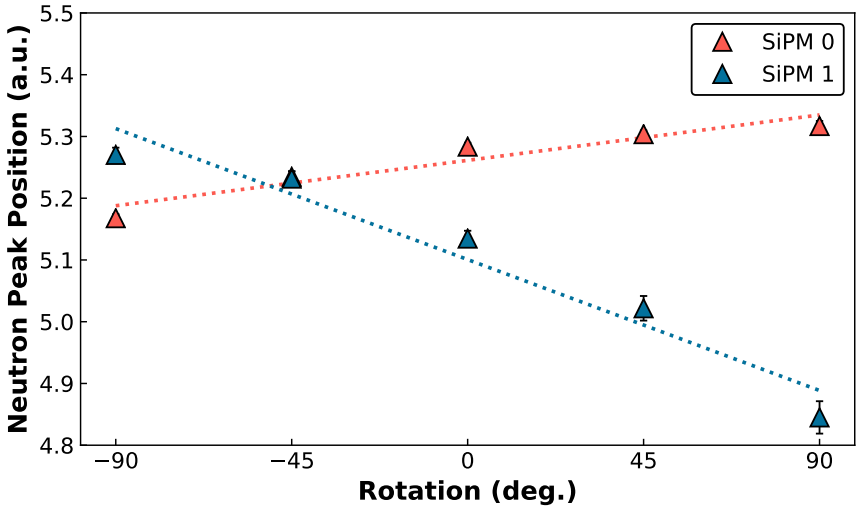

Figure 29. Changes in the neutron peak position as a function of detector rotation. For this measurement, the crystal was again allowed sufficient time to reach thermal equilibrium and additional shielding was introduced so that neutrons could only come from the direction of the source. The dotted lines indicate the best linear fit for SiPM 0 ($R^2 = 0.91$) and SiPM 1 ($R^2 = 0.95$).

The direction of the source can be determined by rotating the crystal and sweeping across the orientations that maximize and minimize the neutron peak position for

both SiPMs. The minimum and maximum peak neutron positions were scaled to the full 180° rotation to find a value for degrees per unit peak position. This value was then used to calculate the directional uncertainty from the uncertainty of the peak position. In this measurement, the thermal neutron source direction uncertainty was ±10°.

5.5 Conclusion

This experiment indicates that determining neutron source direction using a double sided CLYC crystal is feasible. The first and second measurements demonstrate the importance of obtaining thermal equilibrium within the crystal (see Ch. VII for a proposed temperature control method). While the second and third measurements demonstrate the importance of reducing the number of scattered neutrons that enter the crystal.

The addition of moderating material and cadmium shielding in the third measurement significantly increased the change in neutron peak position because there were fewer stray neutrons scattering into the detector from any direction other than directly from the source. There might be some scenarios where scattering is insignificant and can be ignored, but most applications to find the direction of a neutron source using this double sided crystal technique would be greatly improved by removing scattered neutrons.

Rotating the crystal within the five sided moderator/cadmium box worked, but the technique might be improved by permanently attaching cadmium to four sides of the detector so that thermal neutrons can only enter the crystal from one of the SiPM interface sides. Then the whole assembly, including shielding, would be rotated as one unit. The expected output from such a detector would be a large number of neutrons detected when the axis of the detector is collinear with the direction of the

source, decreasing when off-axis and minimized when perpendicular to the direction of the source. Furthermore, the differences in peak position during rotation would indicate which photomultiplier is nearer to the source.

VI. Comparison of Clustering Algorithms for Analysis of Pulse Shape Data from $Cs_2LiYCl_6:Ce^{3+}$ (CLYC)

This study comparing unsupervised computer learning clustering algorithms and developing a methodology for analyzing pulse shape data from CLYC detectors (Research Objective IV) was presented at the *Hardened Electronics And Radiation Technology* (HEART) conference in San Diego, California in April 2019 and generated a manuscript that was submitted to the *Journal of Radiation Effects Research and Engineering* (JRERE) on 15 June 2019. This chapter contains the complete manuscript as submitted to the journal.

M. C. Recker, the primary author, prepared the manuscript and completed the experimentation and data analysis. J. W. McClory provided assistance as the author's research advisor and proofread the manuscript.

6.1 Abstract

Differences in scintillation processes for gamma ray and neutron interactions in $Cs_2LiYCl_6:Ce^{3+}$ (CLYC) enable pulse shape discrimination (PSD) to identify each event. Typically, the determination of an event as gamma ray or neutron interaction is determined by approximating a threshold line between two regions in a plot of PSD ratio vs. energy and declaring one side of the line to be gamma ray events and the other to be neutron events. Three unsupervised computer learning clustering algorithms (K-Means, Gaussian Mixture and DBSCAN) are compared, and a methodology is developed for quickly processing pulse shape data to classify events as either gamma ray or neutron interactions and identify important clusters within the neutron region. The main benefit of this method is that it can isolate the $^{35}Cl(n,p)^{35}S$ interaction with thermal neutrons (0.025 eV), which occurs close to the gamma ray region and is difficult to separate visually.

6.2 Introduction

In recent years, the inorganic scintillator $Cs_2LiYCl_6:Ce^{3+}$ (CLYC) has become a popular research material due to its sensitivity to both gamma rays and neutrons, its excellent energy resolution (∼4% at 662 keV), and its ability to discriminate between both radiation interactions by pulse shape analysis [9, 12, 20]. These two interactions generate photons in several ways; however, only gamma rays can cause core-to-valence luminescence, which occurs when an upper core electron is excited into the conduction band and has an ultrafast decay time (1-4 ns) [19, 21, 23, 26].

This difference in photon generation is apparent when analyzing the waveforms generated by the scintillator when coupled to a photomultiplier. Waveforms generated by gamma interactions will rise and fall quickly whereas the waveforms generated by neutron interactions will tend to rise less quickly and fall much more slowly. A pulse shape discrimination (PSD) ratio is determined by measuring and comparing an area on the rising portion of the waveform to an area on the falling portion of the waveform. The discrimination of neutron events from gamma ray events is done by comparing the PSD ratios and energy measurements of each interaction.

Discrimination of neutron events from gamma events is then accomplished by drawing a threshold line and declaring every interaction on one side to be a neutron event and every event on the other side to be a gamma event. When considering only ^{6}Li(n,t)α interaction with thermal neutrons in CLYC, this is an easy assessment because the neutron events produce approximately 3.2 MeVee of detectable scintillation energy and most of the gamma rays above 2 MeV will pass through a typical 1-inch crystal of CLYC without interacting. However, this discrimination becomes much more difficult when considering the interaction of neutrons with ^{35}Cl which will occur near 500 keV for thermal neutrons. The ability to discriminate neutrons at lower electron equivalent energies is important because the proton released in the ^{35}Cl(n,p)^{35}S

interaction has been shown to have a linear response to neutron energy which may make direct measurements of neutron spectra possible using CLYC, especially if the ^{6}Li content is minimized [4, 31, 44].

A previous study was able to use neural networks and the K-Means clustering algorithm to distinguish between neutron and gamma interactions in CLYC [48]. The goal of this research is to use additional unsupervised machine learning algorithms to identify the gamma ray interactions as well as the two thermal neutron interactions corresponding to ^{6}Li and ^{35}Cl and compare the results from each algorithm. This comparison will be used to develop and then apply a methodology for first filtering gamma events out of the data set, and then searching for clusters of neutron interactions within the remaining data.

6.3 Experiment

The clustering algorithms considered in this study were implemented using the Scikit-learn library for Python [49]. This library is built to facilitate machine learning and has many clustering algorithms that can analyze relatively large amounts of data without requiring extensive code development.

In this study, three clustering algorithms (K-Means, DBSCAN, and Gaussian Mixture) were chosen to identify features within data measured by a CLYC-based detector exposed to both thermal neutron and gamma ray sources. The data chosen for this comparison are from a single measurement using a 1-inch cylinder of CLYC enriched in ^{6}Li produced by RMD [9]. This crystal was coupled to a 51 mm ETEL 9266KEB PMT, biased at -1000 V, and exposed to thermal neutrons generated by a PuBe source in a graphite pile as well as ^{137}Cs and ^{60}Co gamma ray sources. The output signal was read directly from the PMT base without pulse-shaping using a V1720 CAEN digitizer reading at 250 MS/s.

A PSD ratio was determined using

$$PSD\,ratio = \frac{D}{P + D}, \tag{13}$$

where P is the integral of the waveform in the prompt region and D is the integral in the delayed region[45]. When this ratio is plotted against the measured energy for each interaction, clearly defined regions can be identified that correspond to thermal neutron interactions with ^{6}Li (3.2 MeVee) and ^{35}Cl (471 keVee) and gamma ray interactions representing the three full-energy peaks for ^{137}Cs (662 keV) and ^{60}Co (1173 keV and 1332 keV). The energy spectra is shown in Fig. 33a.

For all clustering algorithms, the data were scaled in both PSD ratio and energy using the standardscaler function built into Scikit-learn. This is necessary to ensure both variables are given the same precedence. After scaling, the data set was analyzed by the clustering algorithms which provided a label for each data point corresponding to its group assignment from each algorithm. The algorithms were implemented and timed using a single core of a 2.9 GHz Intel Core i7 processor in an Apple computer with 16 GB of RAM. To prevent overflow for the DBSCAN algorithm, the data had to be analyzed in chunks of 150,000 points. To make a fair comparison between all of the methods, all of the algorithms were limited to 150,000 data points.

From this analysis of clustering algorithms, a methodology is proposed and demonstrated on the original data set and on additional measurements of neutron sources using a CLYC crystal which has been enriched to 99% ^{7}Li (CLYC-7) to limit the ^{6}Li(n,t)α interaction.

6.4 Clustering Algorithm Analysis

K-Means

K-Means is one of the more basic clustering algorithms and is often a first choice when searching for clusters in data sets. The only information required from the user is to specify the number of clusters present, which requires some advanced knowledge. K-means randomly chooses a centroid for each cluster and assigns each data point to the nearest centroid. New centroids are then calculated for each cluster and the data points are reassigned based on their distance from the new centroids. This process is repeated until there are no changes in cluster assignment [50].

This algorithm was set to examine the data set for multiple numbers of clusters (n = 2, 3, 5, and 10). The resultant cluster assignments, when applied to identify two clusters is shown in Fig. 30. This implementation of K-Means was quick ($\sim$8-10 seconds for 10 clusters with 150,000 data points) but unable to distinguish gamma events from neutron events. Increasing the number of clusters from 2 up to 10 did not improve the ability to identify and separate each region. More advanced variations or implementations of K-Means may have more success separating gamma rays and neutrons, but other studies have had trouble discriminating events below 1 MeV [48].

DBSCAN

DBSCAN (Density-Based Spatial Clustering of Applications with Noise) is a clustering algorithm based on the density of points within a certain radius. This method requires no information about the number of true clusters, and instead requires the user to provide a maximum allowable range (ε) for two points to be considered related and a minimum number of related points to constitute a cluster (m). DBSCAN considers each point, in turn, and identifies core samples as those which have m points (including the data point under consideration) within radius ε. A cluster is then

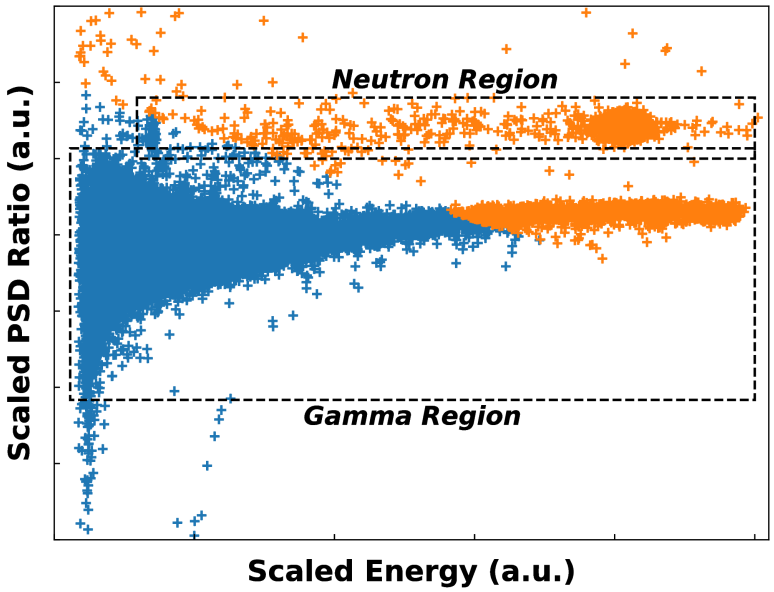

Figure 30. This implementation of the K-Means clustering algorithm is not able to discriminate between neutron and gamma events.

generated by grouping all neighboring core samples with any non-core samples that are within ε of a core point. Increasing m or decreasing ε will increase the density required to generate a cluster [51]. This is the slowest method ($\sim$400 seconds for $\varepsilon = 0.2$ and $m = 20$ with 150,000 data points) of the three considered and can be very resource intensive. However, Fig. 31 shows that DBSCAN was the only algorithm able to identify both of the thermal neutrons interactions (^{6}Li in green and ^{35}Cl in red) and the full gamma region (orange).

Using the full set of data with the Scikit-learn implementation of DBSCAN quickly resulted in memory overflow errors and stopped functioning. Other implementations of DBSCAN (such as the one found in ELKI data mining software) are able to better manage system resources, but take a very long time to run.

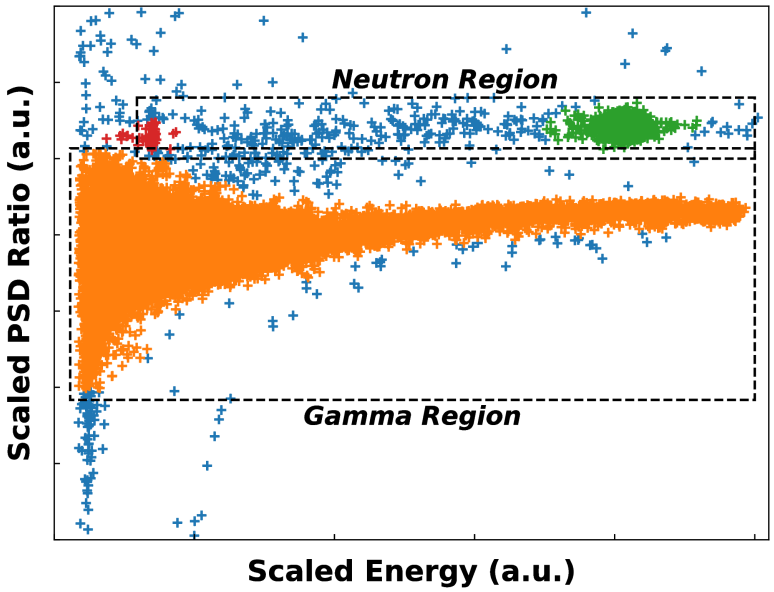

Figure 31. DBSCAN applied to the data is able to identify three clusters corresponding to gamma events (orange), thermal neutrons interacting with ^{6}Li (green), and thermal neutrons interacting with ^{35}Cl (red).

Gaussian Mixture Model

Gaussian Mixture is related to K-Means but assumes that the data set is drawn from a number of gaussian-shaped clusters [52]. The algorithm attempts to assign each data point to one of a number of gaussian distributions (specified by the user) to identify clusters. The result of this method is shown in Fig. 32. This method runs very fast (∼5-6 seconds for 10 clusters in 150,000 data points), but does not work well with fewer than 10 components. Increasing the number of gaussian components for the algorithm to consider gives a measurement of the density as shown in Fig. 32 [53]. In this plot, there are many clusters, however all but two can be assigned to the gamma region. One of these clusters (in green) corresponds to thermal neutrons interacting with ^{6}Li and the remaining cluster captures all of the noise and the rest of the neutron region.

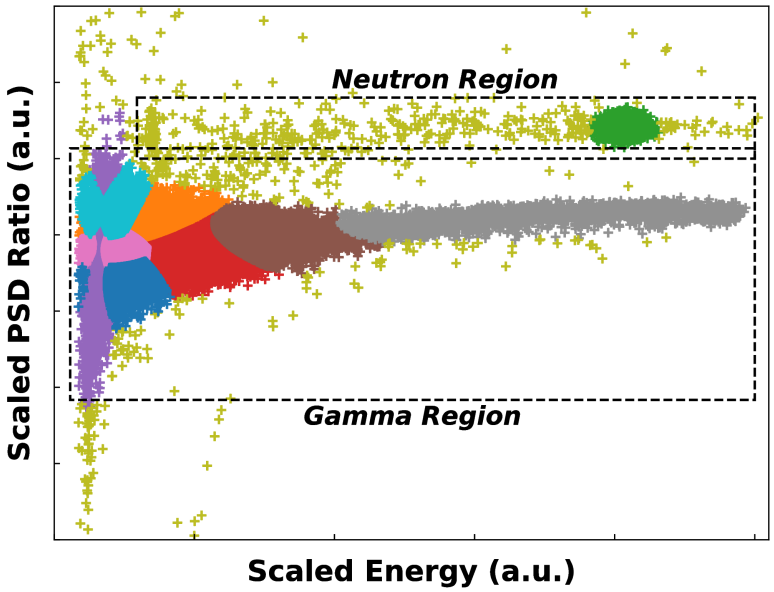

Figure 32. Gaussian Mixture algorithm applied to the data set. When 10 or more gaussian components are used, this algorithm returns a density-based clustering assignment and is able to identify the gamma region as well as the region corresponding to thermal neutrons interaction with ^{6}Li (green cluster in neutron region).

Recommended Cluster Analysis Methodology

From this analysis, K-Means is not a recommended method for separating neutron and gamma interaction data. DBSCAN and Gaussian Mixture were both able to clearly identify the gamma region as well as the ^{6}Li thermal neutron interaction region. DBSCAN was the only algorithm able to pick out the cluster corresponding to thermal neutron interactions with ^{35}Cl, but the cost was a slow compute time that does not scale well with increased data points, which can quickly overwhelm system resources.

The proposed methodology is to use Gaussian Mixture to quickly identify all of the gamma events from the full data set. It is recommended that at least 10 clusters be used to ensure the results are representative of the densities in the PSD ratio plot space. Once tagged as gamma events, these data points can be filtered out along

with any points below a minimum PSD ratio. The remaining data points can then be analyzed as one set with DBSCAN to search for clusters within the neutron region.

6.5 Cluster Analysis Applied

Expanded Data Set

This method is first applied to the original data set in its entirety (∼700,000 interactions) by using Gaussian Mixture to identify 16 clusters, most of which correspond to events in the gamma region. These clusters are tagged as either gamma events, neutron events, or noise if the extent of the cluster is large or its location in PSD-space is ambiguous.

The total energy spectrum measured is shown in Fig. 33a. In this plot, all of the full energy peaks corresponding to the ^{137}Cs (662 keV) and ^{60}Co (1173 keV and 1332 keV) are visible as is the full energy peak corresponding to the ^{6}Li(n,t)α (3.2 MeVee). If the clusters identified as gamma interactions are removed what remains is a mixture of neutron events and noise. These events are plotted on a semilog scale in Fig. 33b and show a strong neutron peak from the ^{6}Li interaction as well as a small peak, just above the baseline, corresponding to the ^{35}Cl(n,p)^{35}S interaction with thermal neutrons. The signal to noise ratio can be improved slightly by setting a minimum threshold of PSD ratios to remove some of the low energy noise (not shown here).

The next step is to take this tagged data set, filter the gamma events, establish a minimum PSD ratio (0.8 in this case), and run the DBSCAN algorithm to find clusters within the neutron region. Some user variation of the algorithm parameters (ε and m) is required to determine the proper values for this step as the best values will vary for each data set analyzed depending on the number of points to be analyzed and the spacing between each point. In this case the best values were $\varepsilon = 0.2$ and $m = 25$. With these values, DBSCAN identified three clusters in the data, shown in Fig. 34a.

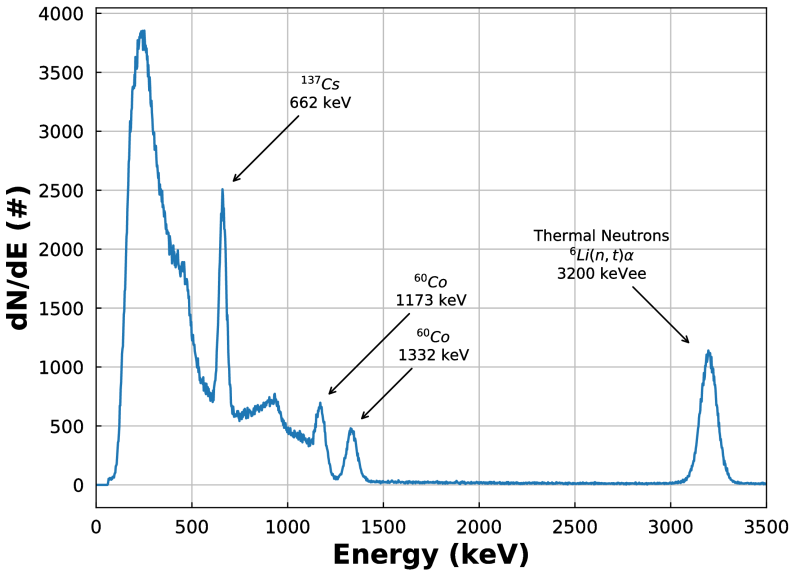

(a) Total Energy Spectrum

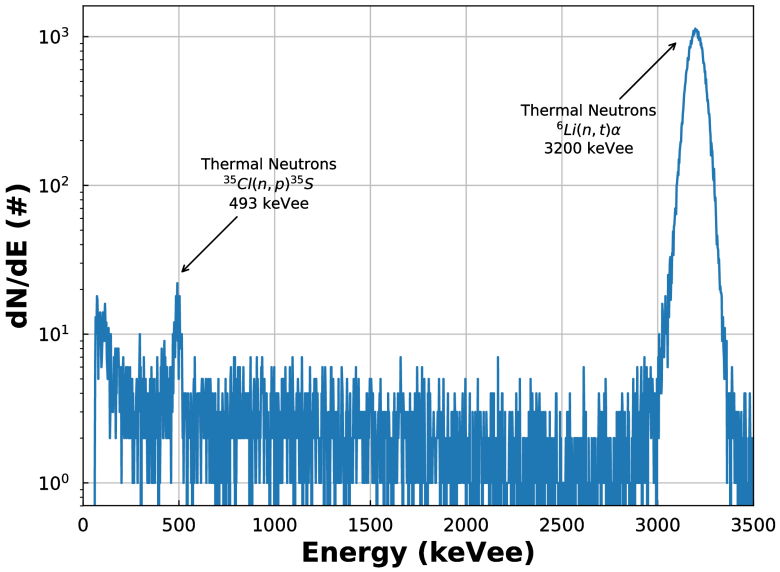

(b) Energy Spectrum without Gamma Interactions

Figure 33. Results of Gaussian Mixture applied to the entire data set. Subplot (a) shows the total response from the scintillator with all full energy gamma peaks identified, as well as the thermal neutron peak corresponding to the ^{6}Li interaction. Subplot (b) shows the same energy range with all of the events tagged as gamma ray interactions removed. On this semilog plot the interactions of thermal neutrons with ^{35}Cl can be seen slightly above the noise at ∼493 keVee.

Two of these clusters corresponded to thermal neutron interactions:^{6}Li(n,t)α, in red (51,013 data points), and ^{35}Cl(n,p)^{35}S, in blue (102 data points). Visually, it appears that DBSCAN did not pick out the full height of the ^{35}Cl cluster which appears to extend up to ∼0.90 PSD ratio. The remaining cluster, in green (47 data points), is located on the edge of the gamma region and likely corresponds to some gamma events that were not identified by the Gaussian Mixture algorithm. The remaining 2,591 data points, shown in gray, correspond to unclustered gamma ray and neutron interactions. The data points between the red and blue clusters correspond to other neutron interactions within the crystal. These could be neutrons that did not fully thermalize within the graphite pile and are interacting with ^{35}Cl to deposit additional energy, or possibly neutrons that interacted with ^{6}Li and were more significantly quenched.

The gamma cluster is excluded and the remaining neutron clusters are plotted as energy histograms in Fig. 34b, and laid over the energy spectrum from Fig. 33b. In the case of a monoenergetic source of thermal neutrons, DBSCAN was able to completely isolate both neutron interactions (^{6}Li and ^{35}Cl in red and blue, respectively) from the background events. This background is composed of gamma interactions remaining after Gaussian Mixture analysis and unclustered neutron interactions. The peaks identified in this plot correspond to the minimum energy deposited into the crystal for each interaction. Therefore, any events with an appropriate PSD ratio (∼0.87-0.90) and energies ranging from 500 keVee to 3.0 MeVee are due to higher energy neutrons interacting with ^{35}Cl. Events with the same PSD ratios and energies above 3.5 MeVee are likely due to interaction with ^{6}Li, since the neutron interaction cross section for ^{6}Li is greater than it is for ^{35}Cl, although ^{35}Cl interactions continue to be possible at all neutron energies.

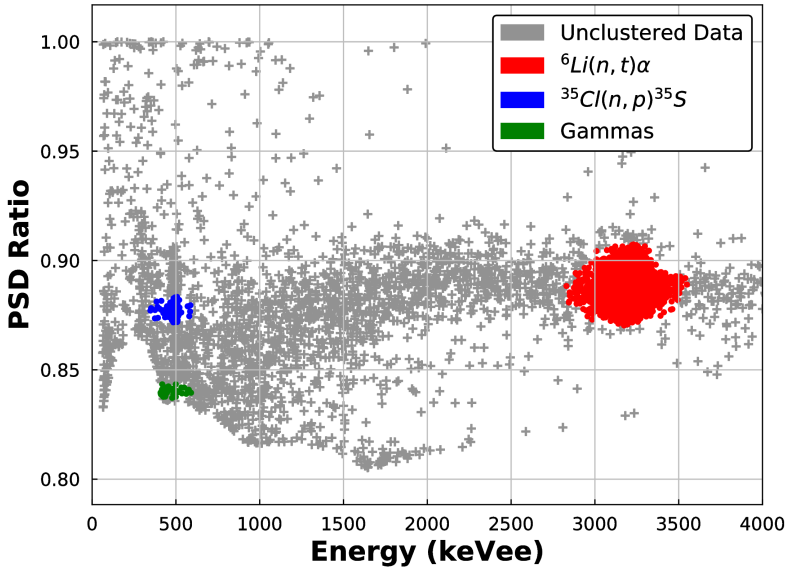

(a) Clusters Identified by DBSCAN

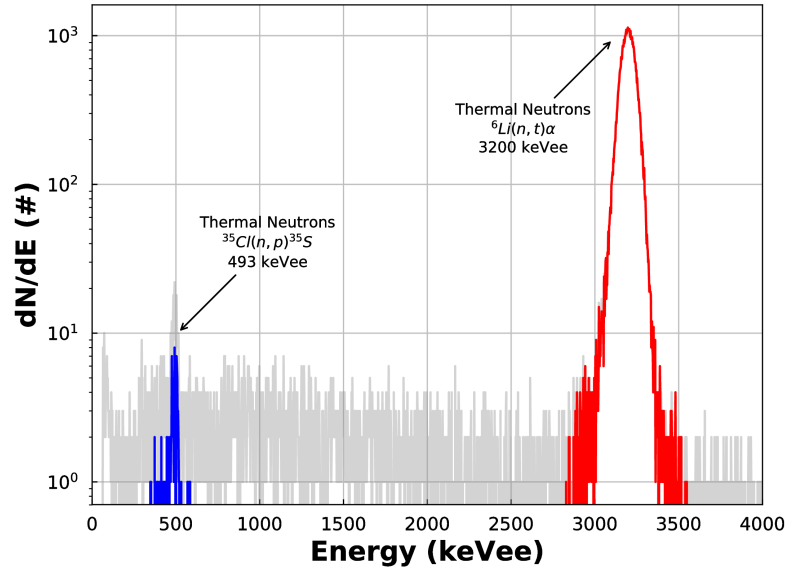

(b) Energy Histogram of Neutron Interactions

Figure 34. Result of DBSCAN algorithm applied to the dataset with gamma interaction events removed. Subplot (a) shows three clusters identified by DBSCAN. The red and blue clusters correspond to thermal neutrons interacting with ^{6}Li and ^{35}Cl, respectively. The green cluster is right on the edge of the gamma region and likely corresponds to gamma ray interactions that were not identified during the Gaussian Mixture analysis. Subplot (b) shows energy histograms of the two neutron clusters (in blue and red) laid over the results of the Gaussian Mixture analysis (in gray) with gamma events removed for comparison. After DBSCAN only the neutron clusters remain and in this histogram the neutron events are clearly identified and noise is greatly reduced.

CLYC-7 with a Thermal Neutron Source

This method can be verified by examining another measurement of the same graphite pile, using a CLYC crystal that is grown with lithium enriched to 99% ^{7}Li, referred to as CLYC-7. This greatly reduces the probability for neutrons to interact with ^{6}Li. The result of applying this methodology is shown in Fig. 35. The first subplot, Fig. 35a, shows the result after both Gaussian Mixture and DBSCAN ($\varepsilon = 0.15$ and $m = 40$) have been applied. Visible, in this plot, are one large cluster of neutron events (^{35}Cl interactions) and one smaller cluster of neutron events (^{6}Li interactions). In this measurement, the space between the ^{35}Cl and ^{6}Li interaction clusters has very few data points, which implies that this region in Fig. 34a is due to additional quenching of the scintillation photons from ^{6}Li interactions.

The second subplot, Fig. 35b, shows the energy histogram for these two clusters plotted over the energy spectrum after Gaussian Mixture, with the gamma events removed. This measurement has reversed the relative size of each cluster, which is what we expect since the ^{6}Li content has been minimized. It should be noted that there is more noise in the energy histogram for the ^{35}Cl interaction (484 keVee) because the identified cluster extended to the edge of the gamma region and likely includes some data points that correspond to interactions with gamma rays and not neutrons. The energy of thermal neutron interaction (3.0 MeVee) is slightly lower than expected (3.2 MeVee) because there were no full energy peaks at high energy for calibration.

CLYC-7 with Continuous Energy Neutron Sources

Cluster analysis of CLYC-7 interactions with continuous energy neutron sources like AmBe or PuBe is more difficult. When measuring monoenergetic sources (such as the thermal neutron source in the previous section), there are two distinct neu-

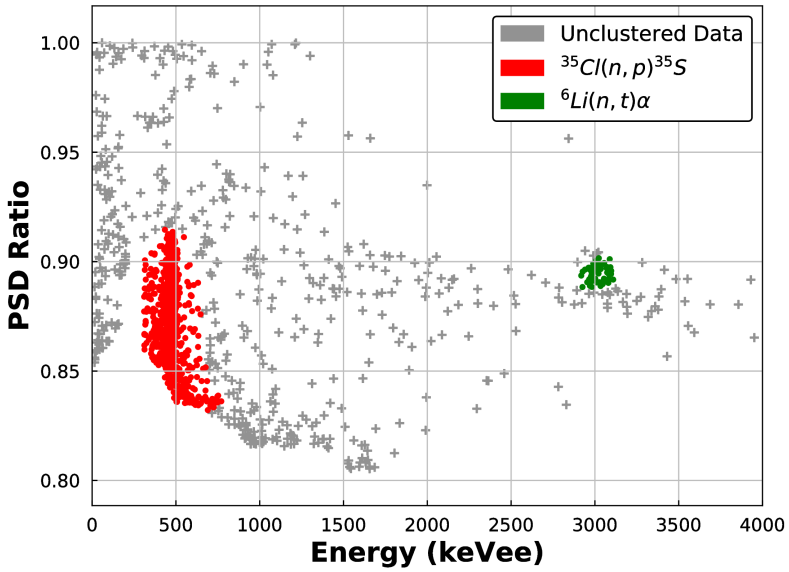

(a) Clusters Identified by DBSCAN

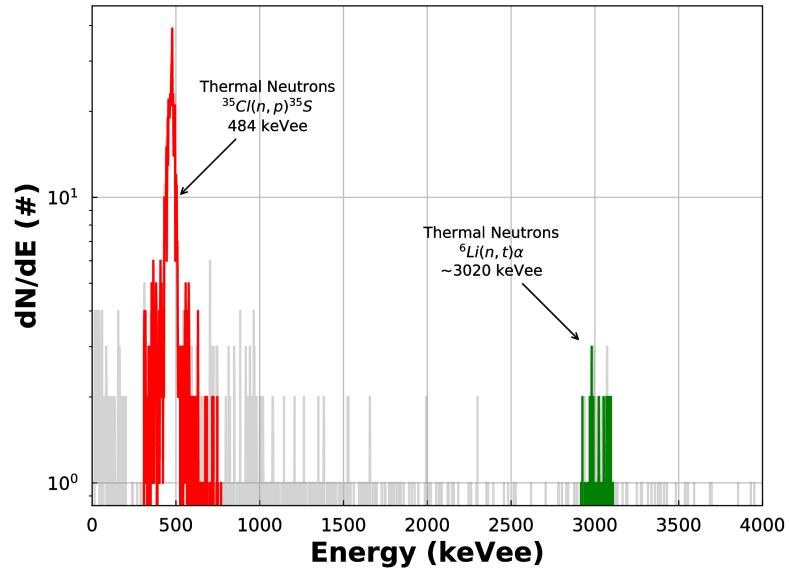

(b) Energy Histogram of Neutron Interactions

Figure 35. Gaussian Mixture and DBSCAN are applied to another data set recorded using a CLYC-7 crystal (grown with 99% enriched ^{7}Li). Due to the lower content of ^{6}Li, the cluster and peak corresponding to thermal neutrons interacting with ^{35}Cl are strengthened while those corresponding to ^{6}Li are diminished.

tron clusters to identify corresponding to the neutron interactions with ^{6}Li and ^{35}Cl, with the ^{35}Cl(n,p)^{35}S interaction being more probable in CLYC-7. This results in a tight grouping in each of the clusters with sparse interactions between the two. In this case, determining the appropriate input parameters for DBSCAN is relatively simple because the output of the algorithm is not very sensitive to the value of the parameters.

For neutron sources with continuous energy, however, this is not true. When using CLYC-7, the lowest energy neutron interactions will result in the creation of $\sim$490 keVee of scintillation photons and increasing the energy of the neutron will increase the amount of photon energy measured. Since the source is continuous there will be no sparse regions in the PSD ratio plot space and any peaked regions within the continuous neutron spectrum will be harder to identify.

This is made more difficult because the response function in CLYC-7 changes depending on the energy of the neutrons interacting. Lower energy neutron interactions will produce a response function that is singly peaked, while higher energy neutrons (>3.5 MeV) will develop a second peak and at higher energy still (>7 MeV) the response function broadens and eventually becomes a continuum [44]. This broadening is due to the increased probability of the ^{35}Cl(n,α)^{32}P interaction at higher energies [44]. As a result, the high energy neutrons from a continuous source can introduce additional data points to the lower region of the energy spectrum that do not correspond to low energy interactions.

When using the DBSCAN algorithm on measurements from a continuous source, the output is very sensitive to the input parameters. User interpretation is required to decide whether the clusters make sense and to identify each as either neutron interactions or noise. Typically, the clusters rejected as noise will be those that are on the edges of the gamma region or those with improper PSD ratios.

The result of applying Gaussian Mixture and DBSCAN ($\varepsilon = 0.35$ and $m = 70$) to an AmBe neutron source (continuous energy up to ∼10 MeV [54]) is shown in Fig. 36. Additional clusters corresponding to noise or gamma interactions have been removed. The energy threshold for these interactions was set higher than in previous measurements because there were a large number of low energy interactions that made the data files too large. As a result, the lowest energy measured is ∼550 keVee and the region corresponding to thermal neutron interaction with ^{35}Cl is not visible in either subplot.

The Fig. 36a subplot shows the clusters identified by DBSCAN in PSD ratio plot space, while the Fig. 36b subplot shows the energy histogram of those neutron interaction clusters (in red) laid over the energy histogram of all interactions (in gray) after Gaussian Mixture was used to remove the gamma ray interactions. Varying the parameters for DBSCAN will change the number and size of clusters identified, but there does not appear to be any direct connection between these clusters and relative peaks in the AmBe neutron spectrum [54].

6.6 Conclusion

The Gaussian Mixture algorithm provides a fast method to identify the majority of gamma ray interactions from CLYC measurements, while the DBSCAN algorithm performs well at locating dense clusters within the remaining interactions. These two algorithms can be combined to process measurements from CLYC. This methodology still requires user interpretation, but could be used to quickly label interactions and identify some neutron features that might be otherwise difficult to separate from the background (such as the small peak from thermal neutrons interacting with ^{35}Cl). Since it works well with thermal neutrons, this method could be used to identify neutrons in data from multiple measurements with various amounts of neutron mod-

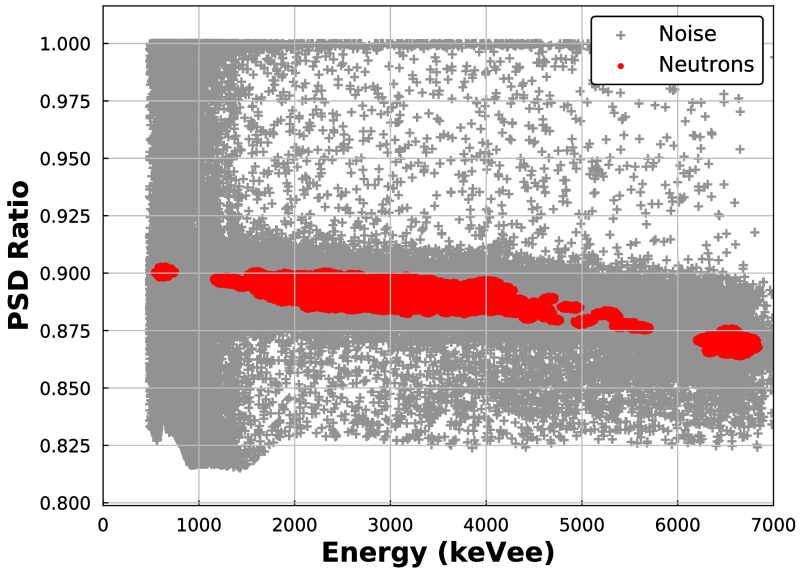

(a) Clusters Identified by DBSCAN

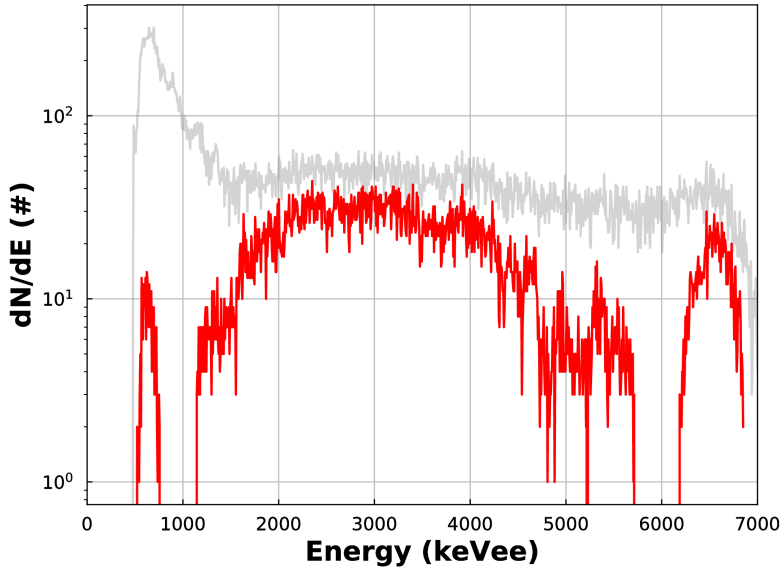

(b) Energy Histogram of Neutron Interactions

Figure 36. Gaussian Mixture and DBSCAN are applied to a data set recorded using a CLYC-7 crystal (grown with 99% enriched ^{7}Li) exposed to a continuous energy neutron source (AmBe).

eration which could be used to unfold a neutron spectrum.

While this method works well with monoenergetic neutrons, it is more complicated for neutron sources with continuous energy distributions. This is especially true for continuous sources with neutron energies above 7 MeV because the response function broadens into a continuum. In these continuous energy measurements, the cluster identification with DBSCAN is highly sensitive to the input parameters. This requires a user to have knowledge about a source in order to interpret the data and identify which clusters are important. One solution to this might be the OPTICS algorithm which is not yet implemented in a stable release version of Scikit-learn. OPTICS does not require input on the appropriate radius for DBSCAN, but only the minimum number of points required to constitute a cluster and then chooses an appropriate radius. Once fully implemented, OPTICS will be used to analyze the data from continuous energy neutron sources.

VII. Controlling CLYC Crystal Temperature and Analysis of CLYC-7 Performance from -20°C to 40°C

This study demonstrated a simple and effective method for controlling the temperature of a CLYC crystal using inexpensive and widely available components and verified that many of the temperature dependent properties of CLYC with 95% ^{6}Li enrichment are the same when using CLYC with 99% ^{7}Li enrichment (Research Objective V). The results of this study are important for the future use of CLYC with ^{7}Li enrichment, but not significant enough on their own to warrant publication.

7.1 Introduction

Previous studies examining the effect of temperature on $Cs_2LiYCl_6:Ce^{3+}$ (CLYC) have focused on crystals made with 95% enriched ^{6}Li, and have not considered those made with 99% enriched ^{7}Li [19, 28, 29, 55]. However, the linear response of the ^{35}Cl(n,p)^{35}S interaction in CLYC might enable neutron spectroscopy and enrichment of the ^{7}Li isotope will be important to reduce the response from ^{6}Li interactions, which would otherwise mask some of the fast neutron interactions with ^{35}Cl.

With a Q value of 616 keV (see Sec. 2.2), thermal neutrons are expected to generate a 616 keV proton. After quenching, this results in a measured electron equivalent energy value of ∼500 keVee (see Ch. IV and Ch. VI). With faster neutrons, beginning around 2.5 MeV, the electron equivalent value will be close to 3.0 MeVee and will start to overlap with the strong peak generated by thermal neutrons interacting with ^{6}Li (3.2 MeVee). Using 99% enriched ^{7}Li greatly reduces the strength of the ^{6}Li(n,t)α peak and enables the response from the ^{35}Cl(n,p)^{35}S interaction to be observed at all incident neutron energy levels.

As discussed in Ch. V and demonstrated in other studies, temperature can have a significant effect on the detector response [19, 28, 29, 55]. Temperature variations in

CLYC have been shown to effect both the amplitude and shape of waveforms, which then effects resolution and FOM [19, 28, 29, 55]. As a result, the desire of this study is to demonstrate a simple and effective method for controlling the temperature of the crystal and verify that the observed behavior of CLYC with 99% ^{7}Li enrichment is the same as reported for CLYC with 95% ^{6}Li enrichment.

7.2 Experimental Method

This experiment used a 1 inch right circular cylinder CLYC crystal, grown by CapeSym, using 99% enriched ^{7}Li (CLYC-7) and packaged into a sealed canister with an optical window for coupling to a photomultiplier. A detector with a custom temperature control system was designed and built for this crystal (see Sec. 7.3) to maintain steady temperatures of -20°C, 0°C, 20°C and 40°C within the crystal.

The temperature was measured at the surface of the crystal package and maintained for 20-30 mins before taking detector measurements to allow the crystal to obtain thermal equilibrium. Once the crystal reached a steady state temperature, the detector was irradiated with thermal neutrons (generated by a PuBe source within a graphite pile) and 662 keV gamma rays from a ^{137}Cs source. Measurements of 30 minutes were taken directly from the base of the PMT without pulse-shaping using a V1720 CAEN 12 bit digitizer reading at 250 MS/s.

7.3 Temperature Controller

A custom temperature controller was built for this experiment, because the range of temperatures required was small (-20°C to 40°C) and easily achievable with commercial-off-the-shelf components. The controller was built using the components listed in Table 4 and primarily consisted of a Raspberry Pi Zero W connected to a temperature probe and a heating element.

Table 4. Temperature controller components

Component	Role	Cost
Raspberry Pi Zero W	Computer System	\$5-\$10
16GB MicroSD Card Class 10	Computer Storage	\$3-\$10
0.96 in. I2C OLED LCD	Display Interface	\$8-\$10
BMP 180 Breakout Board	Temperature Probe	\$7
Electric Relay Switch	Relay Power to Heating Element	\$6-\$25
Electric Heating Pad	Heating Element	\$10

The temperature probe was a BMP180 chip that provided measurements of temperature, barometric pressure and altitude to the Raspberry Pi Zero W through an I2C interface. This chip has a reported accuracy of ±1°C [56] and is mounted to the side of the crystal canister with a thin square of thermally conductive silicone to prevent the exposed circuit board from short-circuiting on the metallic canister and to ensure good thermal transfer from the crystal to the sensor.

The heating element was obtained by removing the heat wire from a therapeutic heating pad. This heat wire was wrapped helically around the packaged CLYC crystal and temperature probe in a single layer from the optical window to the end of the canister. It was held in place with double-sided foam tape between the wire and the crystal and wrapped in electrical tape. The heating element was plugged into an electric relay switch (Adafruit Controllable Outlet Power Relay Module v2) which could be controlled by the Raspberry Pi Zero W to provide power to the heating element when required.

The assembly was placed inside a 3D printed plastic housing and coupled to a 51 mm ETEL 9266KEB PMT. The entire detector was then placed inside a Styrofoam box with dry ice (-78.5°C) to provide indirect, ambient cooling, but alternative methods could be used depending on the application. For example, if the detector were used on an airborne platform, the external air at altitude could provide sufficient cooling.

A Python script was written to read the temperature from the probe and activate the heating element when appropriate. The code reads the temperature and stores the most recent 108 measurements to display as a graph on the LCD screen. This allows visual verification that constant temperature is achieved. The main loop of the program is shown in Fig. 37. The loop begins with a temperature measurement and then subtracts the current temperature value from the target temperature. If the difference is more than 5, the heater is turned on. If the difference is less than 0.2, then the heater is turned off. If the value is in between 0.2 and 5 degrees, then the temperature from third most recent stored temperature is subtracted from the current temperature to determine how fast the temperature is changing and then the heater is either turned on or off, accordingly. Finally, the current value is updated to the displayed plot and the loop begins again. Once the target temperature is reached, the temperature reading tends to oscillate around the target temperature by $\pm$ 0.1°C.

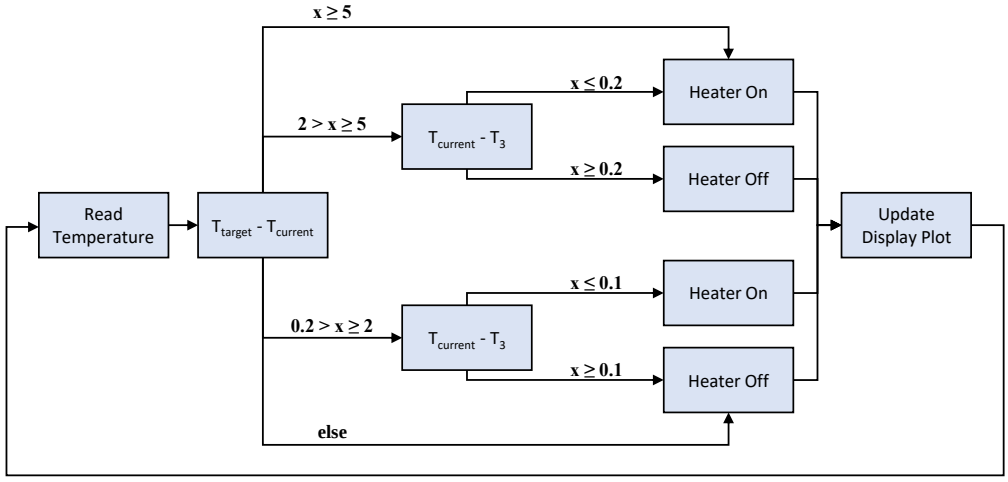

Figure 37. Main programming loop of the temperature controller built for this experiment.

7.4 Results and Analysis

The uncalibrated energy spectra for measurements from -20°C to 40°C are shown in Fig. 38 and the resolutions of the primary photopeak for ^{137}Cs for each temperature are shown in Fig. 39. When moving from low to high temperature, the uncalibrated channel position of each feature in the spectra increases, as does the resolution of the primary photopeak. Additionally, as the temperature increases, the primary photopeak has more defined separation from the Compton edge.

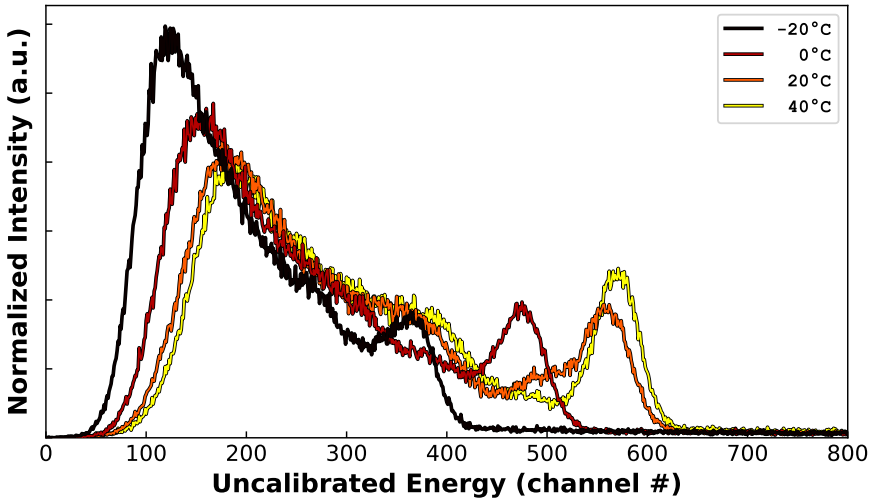

Figure 38. Uncalibrated energy spectra for measurements of a combined gamma ray and neutron environment using a CLYC-7 crystal at temperatures ranging from -20°C to 40°C. The full energy photopeaks and Compton edge are visible at all temperatures. At lower temperatures the full energy photopeak is less resolved, and appears at lower energy channels.

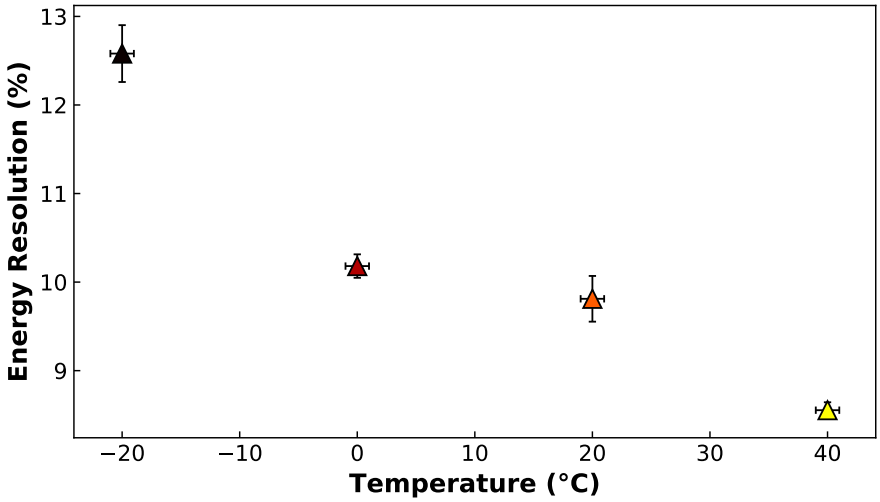

Figure 39. Uncalibrated energy resolution of the ^{137}Cs photopeak for each temperature examined. Increasing temperature, improved the energy resolution with the best value (8.55±0.09%) obtained at 40°C.

This is the expected result, and has been reported on previously [29]. The reason the channel position of the features change can be seen by looking at the waveforms shown in Figs. 40 and 41. For gamma rays, the peak amplitude is decreased slightly with increasing temperature, but the integral of each waveform is greatly increased. These waveforms change with temperature because CVL scintillation is reduced with increasing temperature (eventually unresolvable at ∼125°C) and a larger portion of the gamma ray energy is used for other scintillation processes [55]. As the temperature increases, the reduced contribution of the fast component causes the decrease in peak amplitude, while the increased contribution of the slow components causes the waveform peak to broaden. As discussed in Sec. 2.2, the V_k centers and STEs are able to move more freely with increased thermal energy, which decreases their decay time [19] and further broadens the waveform peak. The integral of the waveform increases with higher temperatures because a larger fraction of the total scintillation photons were observed before the time cutoff (4 μs), additional thermal energy generated more photons in the crystal or noise within the PMT, additional thermal energy reduced

the quenching effect, or a combination of some or all of these.

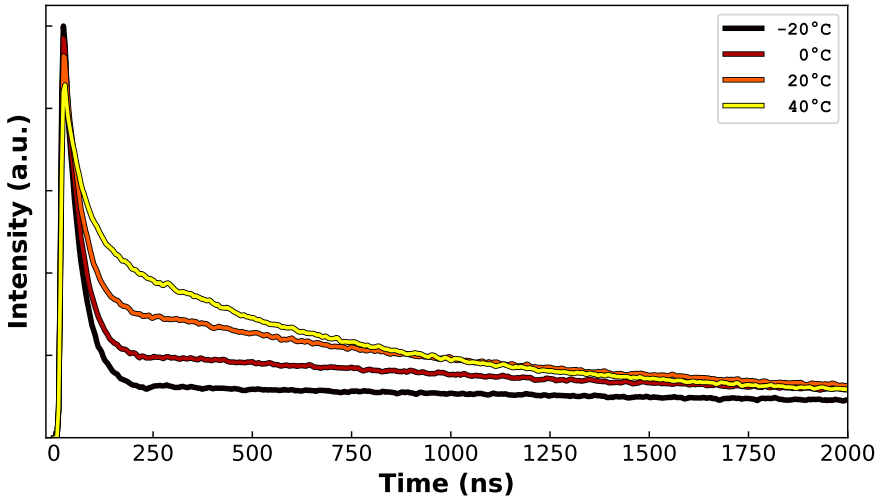

Figure 40. Averaged gamma ray waveforms normalized to the -20°C waveform. Peak amplitude decreases slightly with increasing temperature, but the integral of each waveform is greatly increased with increasing temperature.

For neutrons, both the peak amplitude and the integral are increased with temperature. The difference in behavior is because neutrons cannot cause CVL scintillation. As a result, only the slow component scintillation processes are effected. These change in the same way as with the gamma ray waveforms. Increasing temperature decreases the decay time for V_k centers and STEs, this causes more of the photons to arrive earlier which increases the amplitude and integral of the waveforms. Since this study uses CLYC with low ^{6}Li content, only a few neutrons from the ^{35}Cl(n,p)^{35}S interaction were detected. The averaged neutron waveforms are much noisier, due to the small number detected and they could not be detected at all for measurements below 20°C.

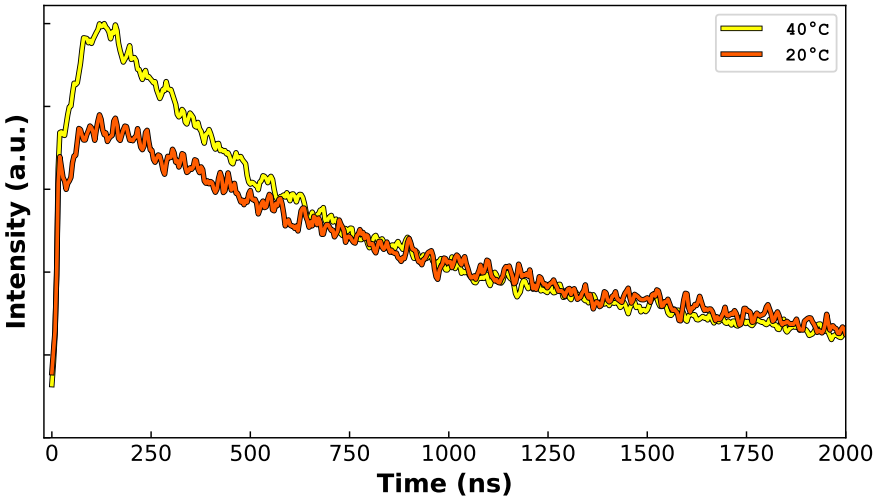

Figure 41. Averaged neutron waveforms normalized to the 40°C waveform. Peak amplitude and integral of each waveform is increased with increasing temperature.

The small number of neutrons also made figure of merit (FOM) calculations for separation of gamma rays and neutrons impossible. However, analysis of the waveforms indicates that the FOM would improve with decreasing temperature. This is because the overall shape of the neutron waveform does not change much, while the gamma ray waveforms change very drastically as the temperature is decreased. At low temperatures, more of the scintillation events occur within the prompt region and therefore the PSD ratio will decrease. This will increase the spacing between the centroids of the gamma ray and neutron regions and improve the FOM. This is consistent with other studies [19, 29, 55].

One new trend observed in this study is that the ability to detect the ^{35}Cl(n,p)^{35}S interaction changes with temperature. Figs. 42-45 show plots of the PSD ratio as a function of uncalibrated energy for all four temperatures (-20°C, 0°C, 20°C, and 40°C). At 40°C, a cluster is discernible that corresponds to this (n,p) interaction. As the temperature is decreased to 20°C, the position of the cluster remains mostly unchanged, but the intensity decreases. At 0°C and below, this cluster is not visible at

all. This is why Fig. 41 only shows the averaged waveforms for 20°C and 40°C. Since decreased temperature reduces the mobility of the V_k centers and STEs, it's possible that the waveform shape or integral are distorted enough that these waveforms mix into the gamma region.

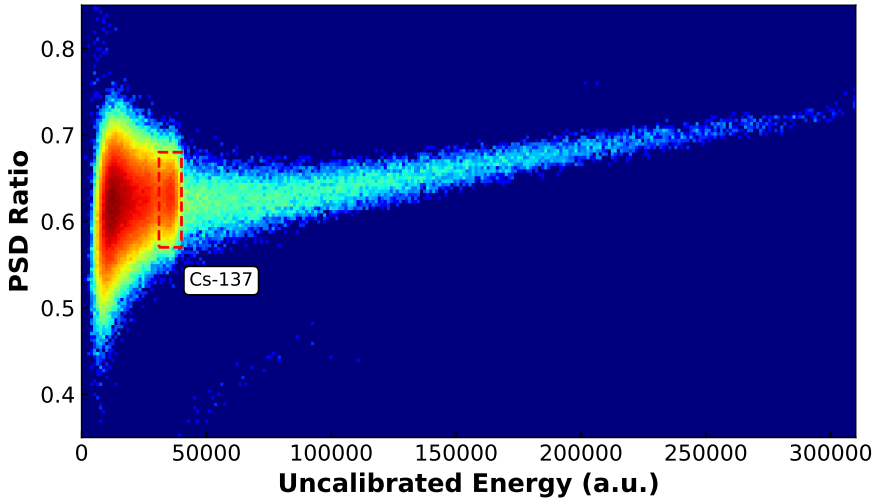

Figure 42. CLYC-7 PSD ratio plotted against uncalibrated energy at -20°C. At this temperature the only feature visible is the photopeak due to ^{137}Cs.

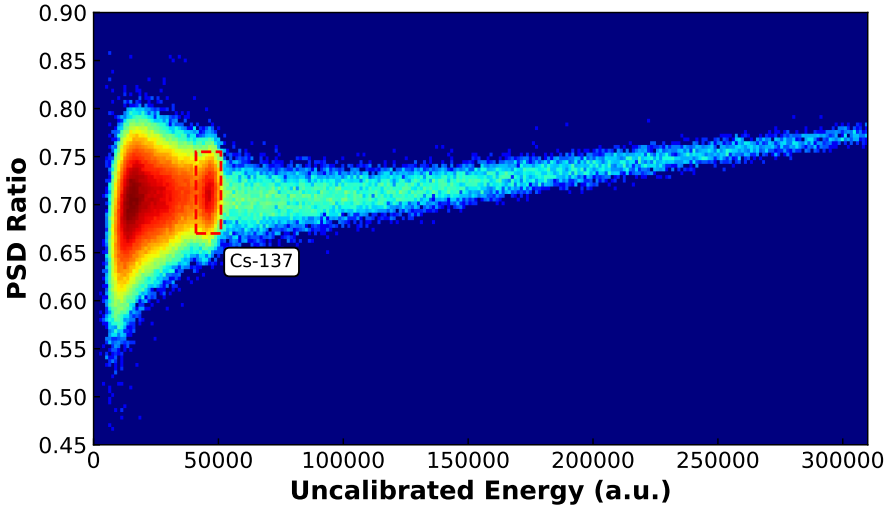

Figure 43. CLYC-7 PSD ratio plotted against uncalibrated energy at 0°C. At this temperature the ^{137}Cs photopeak is the only identifiable feature, but it is more defined than it was in the -20°C measurement.

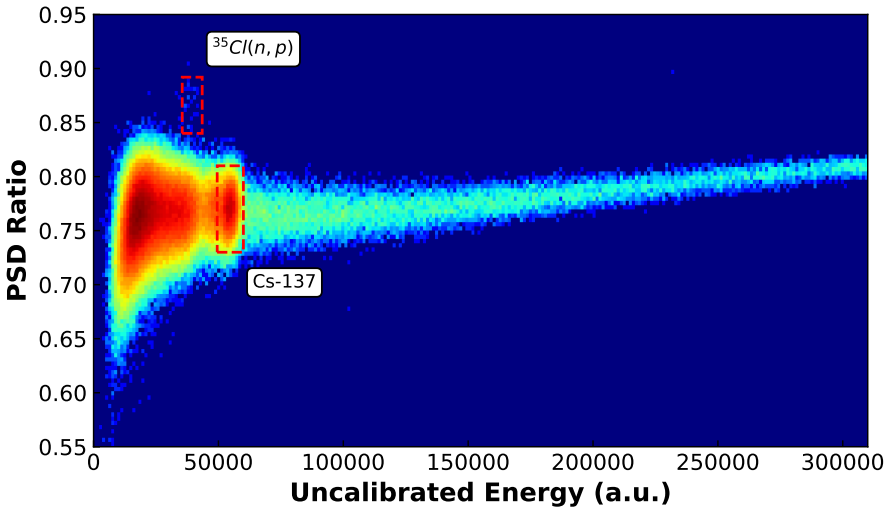

Figure 44. CLYC-7 PSD ratio plotted against uncalibrated energy at 20°C. At this temperature, the ^{137}Cs photopeak is more clearly separated from the gamma rays in the Compton continuum and now neutrons from the ^{35}Cl(n,p)^{35}S interaction are visible.

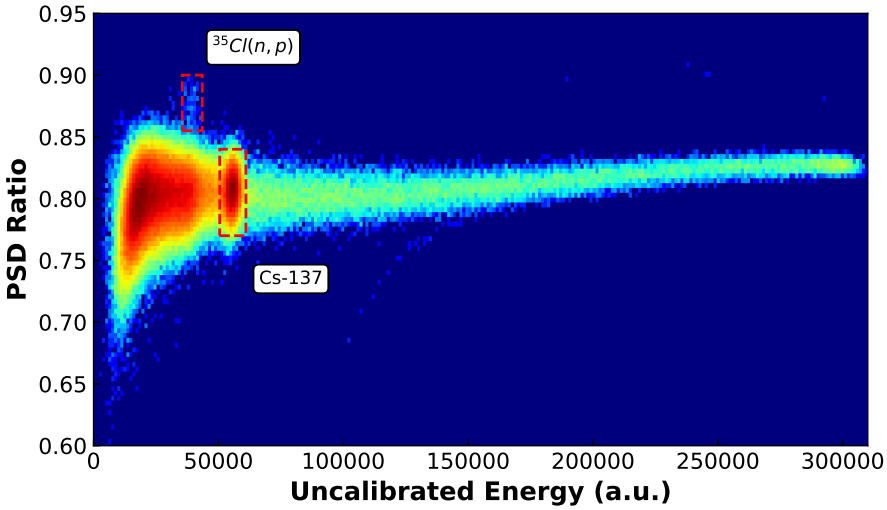

Figure 45. CLYC-7 PSD ratio plotted against uncalibrated energy at 40°C. At this temperature, the ^{137}Cs photopeak is very clearly defined, as is the cluster corresponding to the ^{35}Cl(n.p)^{35}S interaction.

The temperature probe was checked against known temperature values after the experiment and found to have a small nonlinear deviation. For the 40°C measurement,

the corrected temperature was 42.4±0.1°C which is not far from the reported accuracy from the manufacturer (±1°C). All of the other temperature measurements, when corrected, were within 1°C of their intended values.

7.5 Conclusion

This study demonstrated a simple and effective method for controlling temperature of a CLYC crystal using inexpensive and widely available components, any of which could be used in a small portable or mobile system. It also verified that CLYC made with ^{7}Li enrichment (99%) exhibited many of the same temperature-dependent properties as previously observed with CLYC made using ^{6}Li enrichment (95%). Using a range of temperatures from -20°C to 40°C, this study showed that the gamma ray features in the uncalibrated energy spectra moved to higher or lower channels with increased or decreased temperature, respectively, and the uncalibrated energy resolution improved with increased temperature.

Analysis of the waveforms for gamma ray interactions showed that CVL scintillation is more likely for gamma rays at lower temperatures. This has a large effect on the rise time and decay time of the waveforms, ultimately leading to better pulse-shape discrimination at lower temperatures. At higher temperatures, CVL is decreased for gamma ray interactions and the V_k centers and STEs are able to move more freely which reduces their decay time and broadens the peak of the gamma ray waveforms. Since neutrons are not able to cause CVL scintillation, temperature only affected their waveforms by altering the decay time of the V_k centers and STEs. This resulted in changing the amplitude and integral of the neutron waveforms, but not their PSD ratios.

When considering plots of the PSD ratio as a function of uncalibrated energy, the presence and strength of the cluster corresponding to the ^{35}Cl(n,p)^{35}S interaction

appears to depend on the temperature. At low temperatures (-20°C and 0°C), the cluster was not visible. At 20°C the cluster was visible and at 40°C the intensity of the cluster was increased. Understanding the nature of the relationship of temperature to this interaction is important for future CLYC-based neutron detectors which may rely on this interaction for neutron spectroscopy or fast neutron detection.

VIII. Conclusion

The purpose of this research was to further the development of mobile and portable neutron detection systems utilizing scintillating CLYC crystals. This was accomplished through three areas of study that were divided into five research objectives (Table 1). The first area of study was to compare equipment that could be used with CLYC crystals to determine how well the smaller, lighter, and/or less expensive options performed. The second area was to look for new ways to use CLYC and the data measured from CLYC-based detectors that might have an impact on mobile or portable applications. The final area recognized that temperature would be an important variable in mobile and portable operations and studied how temperature would affect the data from systems using CLYC with ^{7}Li enrichment (99%). All research objectives were successfully completed.

The first objective was to consider how well a low cost digitizer would work and whether it would be able to perform PSD analysis. The digitizer chosen was the FemtoDAQ with a 100 MS/s sample rate and an onboard Linux computer. It was able to calculate PSD ratios in real time with very good separation (FOM = 1.42) between neutron and gamma ray events. This study showed that small, inexpensive electronics packages are suitable for use with CLYC and the results were presented at SORMA in 2018 and published in NIM-A.

The second objective was to consider how well a SiPM performed when compared to a PMT for photomultiplication. This is an obvious followup to the first objective because SiPMs are much smaller, lighter, and require less biasing voltage than PMTs, which would be very useful in a mobile or portable system. Furthermore, the FemtoDAQ was built with SiPMs in mind and is able to provide power and biasing for these photomultipliers. Previous studies had differed on how well SiPMs were able to perform when paired with CLYC and no one had made a direct comparison of one

to the other. This study found that moving from a PMT to a SiPM would degrade the energy resolution by 34.0±0.7% (at 662 keV).

Without context, this seems like an untenable degradation. However, CLYC has excellent energy resolution. The best resolution measured in this study was 6.5±0.1% (at 662 keV) with a PMT which coincided with a resolution of 8.6±0.2% (at 662 keV) with a SiPM. For many applications, this change in energy resolution will not present a major concern. In fact, the ability to discriminate neutrons from gamma rays, which might be the most important application for a mobile or portable CLYC-based neutron detector, was similar for both photomultipliers. In one case, the PMT performed better and in the other the SiPM performed better. However, both had figures of merit greater than 2, which indicates very good separation. The results of this study were presented at the IEEE NSS conference in Sydney, Australia in 2018 and accepted for publication in the *IEEE Transactions on Nuclear Science* in 2019.

While conducting the experiment for the second research objective, it was found that the double-sided CLYC crystal appeared to provide information about where the neutron interactions were occurring within the crystal. This information was captured in the broadening of the neutron peak and resulted in the addition of a new research objective. This third objective was to study whether source direction information could be determined using a double sided CLYC crystal with two SiPMs. This experiment found that if temperature was controlled and neutrons scattering from random directions into the detector was eliminated or reduced, then the direction of the source could be determined with an uncertainty of ±10°. This represents a new application for CLYC and would be very useful for mobile and/or portable systems trying to find missing radioactive material or clandestine nuclear operations. It is likely this could be expanded to any scintillating detector where the mean free path of neutrons in the crystal is less than the full length of the detecting medium.

The fourth objective was to take data from a CLYC detector and consider new analysis methods using unsupervised computer learning clustering algorithms. Typically, the determination of gamma ray or neutron interaction is done by applying a cut between the two regions. The goal of this research was to make this process a bit more rigorous and use clustering algorithms to group similar data. This is especially important for the ^{35}Cl(n,p)^{35}S interaction with thermal neutrons, because this cluster of data in PSD plots is very close to the gamma ray region. This study compared multiple clustering algorithms and found that Gaussian Mixture was best suited for the initial classification to determine whether an interaction was due to gamma rays or neutrons. After identifying the gamma rays, they could be removed and then DBSCAN was used to identify clusters in the remaining data. This worked very well for monoenergetic thermal neutrons and made the ^{35}Cl(n,p)^{35}S cluster clearly identifiable. However, when this methodology was applied to neutron sources with continuous energy distributions the results of DBSCAN were harder to interpret. These algorithms still required user knowledge of the data to establish parameters, but it aided the correct determination of the interactions and represents the beginning of a new way to analyze PSD data from CLYC detector measurements.

The final objective was to determine how temperature affected the behavior of CLYC grown with enriched ^{7}Li (99%). This variety of CLYC would be useful in any detector that wanted to maximize the ^{35}Cl(n,p)^{35}S interaction, which could be useful in determining a neutron spectrum. This study was able to show the same behavior with CLYC-7 as with CLYC-6 in response to temperature changes. One new result was that the cluster corresponding to the interaction with ^{35}Cl appeared to have a dependence on temperature. This cluster was not visible for measurements at -20°C and 0°C, but was observed at 20°C and most pronounced at 40°C. This experiment also demonstrated a simple way to control the temperature of the crystal using a

heating wire, an inexpensive temperature probe, and a Raspberry Pi. This experiment showed that temperature has a significant influence on resolution and the previous experiments showed that it also affected the ability to determine neutron source direction. For these reasons, it will be important for mobile and portable detection systems to control and maintain a constant temperature to maximize performance and this technique might provide a cost effective solution.

The results of these experiments can be combined to create a new mobile and/or portable detection system that utilizes the CLYC scintillator for neutron and gamma ray detection. Going forward, there are three major areas of future work that should be considered. Each of these proposed studies would be suitable as research projects for master's students in nuclear engineering and would further advance the field of neutron detection with CLYC:

- The ability to determine neutron source direction with a double sided CLYC crystal and two SiPMs is quite promising. Future work in this area should use a larger, two-inch crystal and make measurements with smaller increments of rotation. One alternative to the box of cadmium and borated polyethylene bricks would be to wrap the side of the crystal in cadmium so that thermal neutrons can only enter through the optical windows. This would provide directional information from not only the thermal neutron peak position, but also from the number of neutrons in the region. This would be maximized when the optical windows are pointed at the source and minimized when the crystal is orthogonal to the direction of the source since the cadmium would prevent neutrons from entering at the side of the crystal.

- Future work should use the results of this research to design and build a mobile or portable neutron detection system that uses CLYC with a SiPM for photomultiplication. Temperature control will be important, and such a sys-

tem should have fans and/or heating elements to keep the temperature steady. That system should have an onboard DAQ with a single chip computer to collect and analyze the data, report results to the user, and control all of the various components. Such a system could be hand-carried or mounted on a vehicle and used for port security, counter-proliferation inspections, or locating lost material.

- Clustering algorithms were shown to work well with a monoenergetic source of thermal neutrons, but most sources will produce neutrons with a range of energies. More work should be done to explore clustering algorithms for these types of neutron sources like AmBe and PuBe. Future studies should explore the OPTICS algorithm, when it is fully implemented in Scikit-learn, or consider other more advanced algorithms that are not currently implemented in easily accessible Python libraries. It might also be possible to recreate these continuous spectra with more data processing and careful selection of parameters for DBSCAN, but this research was not able to achieve that desired state.

Bibliography

1. K. Krane, *Introductory Nuclear Physics*. Hoboken: John Wiley and Sons, Inc., 1988.

2. T. W. Crane and M. P. Baker, "Neutron Detectors," in *Passive Nondestructive Assay of Nuclear Material*, T. D. Reilly, N. Ensslin, and H. A. Smith, Eds., 1991, pp. 379–406.

3. G. F. Knoll, *Radiation Detection and Measurement*, 4th ed. John Wiley and Sons, Inc., 2010.

4. J. Glodo, U. Shirwadkar, R. Hawrami, T. Achtzehn, H. R. Andrews, E. T. H. Clifford, H. Ing, V. D. Kovaltchouk, M. B. Smith, and K. S. Shah, "Fast Neutron Detection With Cs_2LiYCl_6," *IEEE Transactions on Nuclear Science*, vol. 60, no. 2, pp. 864–870, 2013.

5. M. B. Smith, T. Achtzehn, H. R. Andrews, E. T. H. Clifford, H. Ing, and V. D. Kovaltchouk, "Fast Neutron Spectroscopy Using Cs_2LiYCl_6:Ce (CLYC) Scintillator," *IEEE Transactions on Nuclear Science*, vol. 60, no. 2, pp. 855–859, 2013.

6. R. T. Kouzes, E. R. Siciliano, J. H. Ely, P. E. Keller, and R. J. McConn, "Passive neutron detection for interdiction of nuclear material at borders," *Nuclear Instruments and Methods in Physics Research, Section A: Accelerators, Spectrometers, Detectors and Associated Equipment*, vol. 584, no. 2-3, pp. 383–400, 2008.

7. B. Geelhood, J. Ely, R. Hansen, R. Kouzes, J. Schweppe, and R. Warner, "Overview of portal monitoring at border crossings," *2003 IEEE Nuclear Science Symposium. Conference Record (IEEE Cat. No.03CH37515)*, vol. 1, pp. 513–517, 2003.

8. R. T. Kouzes, E. R. Siciliano, J. H. Ely, P. E. Keller, and R. J. McConn, "Passive neutron detection at borders," *IEEE Nuclear Science Symposium Conference Record*, vol. 2, pp. 1115–1119, 2007.

9. J. Glodo, R. Hawrami, and K. Shah, "Development of Cs_2LiYCl_6 scintillator," *Journal of Crystal Growth*, vol. 379, pp. 73–78, 2013.

10. R. C. Byrd, J. M. Moss, W. C. Priedhorsky, C. A. Pura, G. W. Richter, K. J. Saeger, W. R. Scarlett, S. C. Scott, and R. L. Wagner, "Nuclear detection to prevent or defeat clandestine nuclear attack," *IEEE Sensors Journal*, vol. 5, no. 4, pp. 593–608, 2005.

11. R. T. Kouzes and J. H. Ely, "PNNL-19360: Status Summary of 3 He and Neutron Detection Alternatives for Homeland Security," Tech. Rep. April, 2010.

12. C. M. Combes, P. Dorenbos, C. W. E. Van Eijk, K. W. Krak, and H. U. Guk, "Optical and scintillation properties of pure and Ce^{3+}-doped Cs_2LiYCl_6 and Li_3YCl_6:Ce^{3+} crystals," *Journal of Luminescence*, vol. 82, pp. 299–305, 1999.

13. F. P. Doty, X. Zhou, P. Yang, and M. A. Rodriguez, "Elpasolite Scintillators," Tech. Rep. December, 2012.

14. E. M. Baum, M. C. Ernesti, H. D. Knox, T. R. Miller, and A. M. Watson, *Nuclides and Isotopes: Chart of the Nuclides*, 17th ed. Bechtel Marine Propulsion Corporation, 2010.

15. A. A. Sonzogni, "Nuclear data sheets for A = 134," *Nuclear Data Sheets*, vol. 103, no. 1, pp. 1–182, 2004.

16. E. Browne, "Nuclear Data Sheets for A = 90," *Nuclear Data Sheets*, vol. 82, no. 2, pp. 379–546, 1997.

17. J. Glodo, W. M. Higgins, E. V. D. Van Loef, and K. S. Shah, "Scintillation properties of 1 inch Cs_2LiYCl_6:Ce crystals," *IEEE Transactions on Nuclear Science*, vol. 55, no. 3, pp. 1206–1209, 2008.

18. D. W. Lee, L. C. Stonehill, A. Klimenko, J. R. Terry, and S. R. Tornga, "Pulse-shape analysis of Cs_2LiYCl_6:Ce scintillator for neutron and gamma-ray discrimination," *Nuclear Instruments and Methods in Physics Research, Section A: Accelerators, Spectrometers, Detectors and Associated Equipment*, vol. 664, no. 1, pp. 1–5, 2012.

19. B. S. Budden, L. C. Stonehill, J. R. Terry, A. V. Klimenko, and J. O. Perry, "Characterization and Investigation of the Thermal Dependence of Cs2LiYCl6:Ce3+ (CLYC) Waveforms," *IEEE Transactions on Nuclear Science*, vol. 60, no. 2, pp. 946 – 951, 2012.

20. M. B. Smith, M. McClish, T. Achtzehn, H. R. Andrews, M. J. Baginski, D. J. Best, B. S. Budden, E. T. H. Clifford, N. A. Dallmann, C. Dathy, J. M. Frank, S. A. Graham, H. Ing, and L. C. Stonehill, "Assessment of photon detectors for a handheld gamma-ray and neutron spectrometer using Cs_2LiYCl_6:Ce (CLYC) scintillator," *Nuclear Instruments and Methods in Physics Research, Section A: Accelerators, Spectrometers, Detectors and Associated Equipment*, vol. 715, pp. 92–97, 2013.

21. E. van Loef, P. Dorenbos, C. van Eijk, K. Kramer, and H. Gudel, "Scintillation and spectroscopy of the pure and Ce^{3+}-doped elpasolites : Cs_2LiYX_6 (X = Cl , Br)," *Journal of Physics: Condensed Matter*, vol. 14, no. 36, pp. 8481–8496, 2002.

22. E. van Loef, J. Glodo, W. Higgins, and K. Shah, "Optical and scintillation prop-

erties of $Cs_2LiYCl_6:Ce^{3+}$ and $Cs_2LiYCl_6:Pr^{3+}$ crystals," *IEEE Transactions on Nuclear Science*, vol. 52, no. 5, pp. 1819–1822, 2005.

23. A. Bessiere, P. Dorenbos, C. van Eijk, K. Kramer, and H. Gudel, "New thermal neutron scintillators: $Cs_2LiYCl_6:Ce^{3+}$ and $Cs_2LiYBr_6:Ce^{3+}$," *IEEE Transactions on Nuclear Science*, vol. 51, no. 5, pp. 2970–2972, 2004.

24. P. Dorenbos, "Scintillation mechanisms in Ce 3+ doped halide scintillators," *Physica Status Solidi (A) Applications and Materials Science*, vol. 202, no. 2, pp. 195–200, 2005.

25. R. T. Williams and K. S. Song, "The self-trapped exciton," *Journal of Physics and Chemistry of Solids*, vol. 51, no. 7, pp. 679–716, 1990.

26. P. A. Rodnyi, "Core-valence luminescence in scintillators," *Radiation Measurements*, vol. 38, no. 4-6, pp. 343–352, 2004.

27. N. Dolympia, P. Chowdhury, C. J. Guess, T. Harrington, E. G. Jackson, S. Lakshmi, C. J. Lister, J. Glodo, R. Hawrami, K. Shah, and U. Shirwadkar, "Optimizing Cs 2LiYCl 6 for fast neutron spectroscopy," *Nuclear Instruments and Methods in Physics Research, Section A: Accelerators, Spectrometers, Detectors and Associated Equipment*, vol. 694, pp. 140–146, 2012.

28. F. Liang, H. Brands, L. Hoy, J. Preston, and J. Smith, "Scintillation detectors constructed with an optimized 2x2 silicon photomultiplier array," *2016 IEEE Nuclear Science Symposium, Medical Imaging Conference and Room-Temperature Semiconductor Detector Workshop (NSS/MIC/RTSD)*, pp. 1–6, 2016.

29. K. E. Mesick, L. C. Stonehill, J. T. Morrell, and D. D. S. Coupland, "Performance of several solid state photomultipliers with CLYC scintillator," in *2015 IEEE*

Nuclear Science Symposium and Medical Imaging Conference, NSS/MIC 2015, 2015, pp. 1–4.

30. B. S. Budden, A. J. Couture, L. C. Stonehill, A. V. Klimenko, J. R. Terry, and J. O. Perry, "Analysis of Cs_2LiYCl_6:Ce^{3+} (CLYC) waveforms as read out by solid state photomultipliers," *IEEE Nuclear Science Symposium Conference Record*, pp. 347–350, 2012.

31. N. D'Olympia, P. Chowdhury, C. J. Lister, J. Glodo, R. Hawrami, K. Shah, and U. Shirwadkar, "Pulse-shape analysis of CLYC for thermal neutrons, fast neutrons, and gamma-rays," *Nuclear Instruments and Methods in Physics Research, Section A: Accelerators, Spectrometers, Detectors and Associated Equipment*, vol. 714, pp. 121–127, 2013.

32. Raspberry Pi Foundation, "Raspberry Pi 3 Model B+," 2018. [Online]. Available: https://www.raspberrypi.org/products/raspberry-pi-3-model-b-plus/

33. BeagleBoard.org Foundation, "BeagleBone Black," 2018. [Online]. Available: https://beagleboard.org/black

34. B. Travaglione, A. Munyard, and D. Matthews, "Using low cost single-board microcontrollers to record underwater acoustical data," *Internoise 2014*, pp. 1–8, 2014.

35. V. M. Cvjetkovic and M. Matijevic, "Overview of architectures with arduino boards as building blocks for data acquisition and control systems," *International Journal of Online Engineering*, vol. 12, no. 7, pp. 10–17, 2016.

36. R. Mukaro, "A microcontroller-based data acquisition system for solar radiation and environmental monitoring," *IEEE Transactions on Instrumentation and Measurement*, vol. 48, no. 6, pp. 1232–1238, 1999.

37. W. Skulski, A. Ruben, and S. Benzvi, "FemtoDAQ: A Low-Cost Digitizer for SiPM-Based Detector Studies and Its Application to the HAWC Detector Upgrade," *IEEE Transactions on Nuclear Science*, vol. 64, no. 7, pp. 1677–1682, 2017.

38. M. B. Smith, T. Achtzehn, H. R. Andrews, E. T. Clifford, P. Forget, J. Glodo, R. Hawrami, H. Ing, P. O'Dougherty, K. S. Shah, U. Shirwadkar, L. Soundara-Pandian, and J. Tower, "Fast neutron measurements using Cs_2LiYCl_6:Ce (CLYC) scintillator," *Nuclear Instruments and Methods in Physics Research, Section A: Accelerators, Spectrometers, Detectors and Associated Equipment*, vol. 784, pp. 162–167, 2015.

39. H. Singh and S. Singh, "Novel discrimination parameters for neutron-gamma discrimination with liquid scintillation detectors using wavelet transform," *Journal of Instrumentation*, vol. 10, no. 6, 2015.

40. S. Yousefi and L. Lucchese, "A wavelet-based pulse shape discrimination method for simultaneous beta and gamma spectroscopy," *Nuclear Instruments and Methods in Physics Research, Section A: Accelerators, Spectrometers, Detectors and Associated Equipment*, vol. 599, no. 1, pp. 66–73, 2009.

41. B. S. Budden, L. C. Stonehill, N. A. Dallmann, J. M. Michel, M. J. Baginski, D. J. Best, C. Dathy, J. M. Frank, M. McClish, and M. B. Smith, "Gain stabilization and pulse-shape discrimination in a thermally-variant environment for a hand-held radiation monitoring device utilizing $Cs_2LiYCl_6:Ce^{3+}$ (CLYC) scintillator," *IEEE Nuclear Science Symposium Conference Record*, pp. 351–356, 2012.

42. W. G. J. Langeveld, M. J. King, J. Kwong, and D. T. Wakeford, "Pulse Shape Discrimination Algorithms, Figures of Merit and Gamma Rejection for Liquid

and Solid Scintillators," *IEEE Transactions on Nuclear Science*, vol. 9499, no. c, pp. 1–1, 2017.

43. W. M. Higgins, J. Glodo, U. Shirwadkar, A. Churilov, E. Van Loef, R. Hawrami, G. Ciampi, C. Hines, and K. S. Shah, "Bridgman growth of Cs_2LiYCl_6:Ce and ^{6}Li-enriched $Cs_2{}^6LiYCl_6$:Ce crystals for high resolution gamma ray and neutron spectrometers," *Journal of Crystal Growth*, vol. 312, no. 8, pp. 1216–1220, 2010.

44. N. Dolympia, P. Chowdhury, E. G. Jackson, and C. J. Lister, "Fast neutron response of ^{6}Li-depleted CLYC detectors up to 20 MeV," *Nuclear Instruments and Methods in Physics Research, Section A: Accelerators, Spectrometers, Detectors and Associated Equipment*, vol. 763, pp. 433–441, 2014.

45. M. C. Recker, E. J. Cazalas, and J. W. McClory, "Pulse shape discrimination with a low-cost digitizer using commercial off-the-shelf components," *Nuclear Instruments and Methods in Physics Research, Section A: Accelerators, Spectrometers, Detectors and Associated Equipment*, no. July, 2018. [Online]. Available: https://doi.org/10.1016/j.nima.2018.10.157

46. A. Giaz, N. Blasi, C. Boiano, S. Brambilla, F. Camera, C. Cattadori, S. Ceruti, F. Gramegna, T. Marchi, I. Mattei, A. Mentana, B. Million, L. Pellegri, M. Rebai, S. Riboldi, F. Salamida, and M. Tardocchi, "Fast neutron measurements with7Li and6Li enriched CLYC scintillators," *Nuclear Instruments and Methods in Physics Research, Section A: Accelerators, Spectrometers, Detectors and Associated Equipment*, vol. 825, pp. 51–61, 2016. [Online]. Available: http://dx.doi.org/10.1016/j.nima.2016.03.090

47. M. C. Recker, E. J. Cazalas, J. W. Mcclory, and J. E. Bevins, "Comparison of SiPM and PMT Performance Using a CLYC Scintillator with Two Optical Windows," *Transactions on Nuclear Science*, vol. PP, no. APRIL, p. 1, 2019.

48. E. Doucet, T. Brown, P. Chowdhury, C. J. Lister, C. Morse, P. C. Bender, and A. M. Rogers, "Machine learning n/γ discrimination in CLYC scintillators," *Nuclear Instruments and Methods in Physics Research, Section A: Accelerators, Spectrometers, Detectors and Associated Equipment*, no. July, 2018. [Online]. Available: https://doi.org/10.1016/j.nima.2018.09.036

49. F. Pedregosa, G. Varoquaux, A. Gramfort, V. Michel, B. Thirion, O. Grisel, M. Blondel, P. Prettenhofer, R. Weiss, V. Dubourg, J. Vanderplas, A. Passos, D. Cournapeau, M. Brucher, M. Perrot, and É. Duchesnay, "Scikit-learn: Machine Learning in Python," *Journal of Machine Learning Research*, vol. 12, pp. 2825–2830, 2012.

50. W. L. Martinez, A. R. Martinez, and J. L. Solka, *Exploratory Data Analysis with MATLAB*, 2nd ed. Boca Raton: CRC Press, 2011.

51. S. learn developers, "Scikit-Learn User Guide," 2018. [Online]. Available: https://scikit-learn.org/stable/user_guide.html

52. A. K. Jain and R. C. Dubes, *Algorithms for Clustering Data*. Englewiid Cliffs: Prentice Hall, 1988.

53. S. Theodoridis and K. Koutroumbas, *Pattern Recognition*, 4th ed. Academic Press (Elsevier), 2009.

54. J. W. Marsh, D. J. Thomas, and M. Burke, "Am-Be and Am-B neutron sources," vol. 366, 1995.

55. K. Yang and P. R. Menge, "Pulse shape discrimination of Cs_2LiYCl_6:Ce^{3+} scintillator from -30Â°C to 180Â°C," *Nuclear Instruments and Methods in Physics Research, Section A: Accelerators, Spectrometers, Detectors*

and Associated Equipment, vol. 784, pp. 74–79, 2015. [Online]. Available: http://dx.doi.org/10.1016/j.nima.2014.08.031

56. "BMP180 Barometric Pressor Sensors." [Online]. Available: https://www.bosch-sensortec.com/bst/products/all_products/bmp180

REPORT DOCUMENTATION PAGE

Form Approved
OMB No. 074-0188

1. REPORT DATE *(DD-MM-YYYY)*	2. REPORT TYPE	3. DATES COVERED *(From – To)*
12-09-2019	Ph.D. Dissertation	Oct 2016 – Sep 2019

4. TITLE AND SUBTITLE
Enabling Mobile Neutron Detection Systems with CLYC

5a. CONTRACT NUMBER

5b. GRANT NUMBER

5c. PROGRAM ELEMENT NUMBER

6. AUTHOR(S)
Recker, Matthew C., Major, USAF

5d. PROJECT NUMBER

5e. TASK NUMBER

5f. WORK UNIT NUMBER

7. PERFORMING ORGANIZATION NAMES(S) AND ADDRESS(S)
Air Force Institute of Technology
Graduate School of Engineering and Management (AFIT/EN)
2950 Hobson Way, Building 640
Wright-Patterson AFB, OH 45433-7765

8. PERFORMING ORGANIZATION REPORT NUMBER
AFIT-ENP-DS-19-S-028

9. SPONSORING/MONITORING AGENCY NAME(S) AND ADDRESS(ES)
POC: COL Chad Schools (chad.c.schools.mil@mail.mil)
Defense Threat Reduction Agency
8725 John J. Kingman Rd
Ft. Belvoir, VA 22060

10. SPONSOR/MONITOR'S ACRONYM(S)
DTRA

11. SPONSOR/MONITOR'S REPORT NUMBER(S)

12. DISTRIBUTION/AVAILABILITY STATEMENT
Distribution Statement A. Approved for Public Release; Distribution Unlimited

13. SUPPLEMENTARY NOTES
This material is declared a work of the U.S. Government and is not subject to copyright protection in the United States.

$Cs_2LiYCl_6:Ce^{3+}$ (CLYC) has the desirable property of being sensitive to both gamma rays and neutrons while producing waveforms suitable for pulse shape discrimination (PSD) to determine which radiation was detected. This dissertation examines the behavior of CLYC to support its further development for mobile and portable applications. First, the feasibility of performing PSD with CLYC and an inexpensive data acquisition system was examined. This system was able to clearly distinguish both events with a figure of merit of 1.42. Next, the performance of a SiPM was compared to a traditional PMT. Analysis showed that the SiPM degraded the energy resolution by an average of 34.0±0.7% (at 662 keV). Measurements were also taken using a CLYC crystal with two optical windows which was rotated to determine the direction of a neutron source with an accuracy of ±10°. An analysis of the ability of clustering algorithms to discriminate between gamma ray and neutron interactions was also performed. A methodology was developed and applied to separate these two interactions and provide the ability to isolate the $^{35}Cl(n,p)^{35}S$ interaction with thermal neutrons, which occurs close to the gamma ray region and is difficult to separate visually. Finally, the effect of temperature on a ^{7}Li (99%) enriched CLYC crystal (important when the $^{35}Cl(n,p)^{35}S$ interaction is more desirable than $^{6}Li(n,t)\alpha$ interaction) was examined. Measurements agreed with previous results from ^{6}Li (95%) enriched CLYC, but also indicated that identifying the cluster corresponding to thermal neutrons interacting with ^{35}Cl was temperature dependent.

15. SUBJECT TERMS
neutron detection, n-γ discrimination, CLYC, silicon photomultiplier, cluster analysis, source direction

16. SECURITY CLASSIFICATION OF:			17. LIMITATION OF ABSTRACT	18. NUMBER OF PAGES	19a. NAME OF RESPONSIBLE PERSON
a. REPORT	b. ABSTRACT	c. THIS PAGE			Dr. John W. McClory
U	U	U	UU	138	19b. TELEPHONE NUMBER *(Include area code)* (937)255-6565 x7308